



Contract Number: 622177

## Deliverable n°3.4

# New sensors for repository monitoring

### Work Package 3

Project Acronym	Modern2020
Project Title	Development and Demonstration of Monitoring Strategies and Technologies for Geological Disposal
Start date of project	01/06/2015
Duration	48 Months
Lead Beneficiary	<i>Andra</i>
Contributor(s)	Johan BERTRAND and Sylvie LESOILLE (Andra, France) Héctor Luis ABOS GRACIA (Arquimea, Spain) , Jiří SVOBODA (CTU, czech republic) Mauro CAPPELLI (ENEA, Italy) Firat Berrak BERRAK, Toshihiro SAKAKI and Tobias Vogt (NAGRA, Switzerland) Christian BROADWAY - Damien KINET - Patrice MÉGRET (UMONS, Belgium) Maryna Kudinova, Jean Louis Auguste & George Humbert (XLIM, France) Joonas JARVINEN (VTT, Finland)
Contractual Delivery Date	31/05/2019
Actual Delivery Date	31/05/2019
Reporting period 3:	01/06/2018 - 31/05/2019
Version	final

<i>Project co-funded by the European Commission under the Euratom Research and Training Programme on Nuclear Energy within the Horizon 2020 Framework Programme</i>		
<b>Dissemination Level</b>		
<b>PU</b>	Public	X
<b>PP</b>	Restricted to other programme participants (including the Commission Services)	
<b>RE</b>	Restricted to a group specified by the partners of the Modern2020 project	
<b>CO</b>	Confidential, only for partners of the Modern2020 project and EC	

History chart			
Type of revision	Document name	Partner	Date
General review	Modern_D3.4_version1	<i>Jose-Luis Garcia Sineriz (Amberg)</i>	28/05/2019

**Reviewed by**

*Jose-Luis Garcia Sineriz (Amberg)*

**Approved by:**

This report has been approved by:

- José-luis Garcia-Sineriz, Work Package 3 Leader, *31/05/2019*
- Johan Bertrand, the Modern2020 Project Co-ordinator (on behalf of the Modern2020 Project Executive Board), *31/05/2019*



## Abstract

---

Research and development (R&D) has demonstrated that technologies exist for monitoring the near field. However, existing technologies have limitations, which has to be addressed before the beginning of the operational geological monitoring program. These include the adaptation of the technologies to specific monitoring objectives, host rocks and repository concepts, for the monitoring of specific parameters, and improvement of the long-term performance.

The underground installations of the geological disposal will be built progressively and operated over a period about a century. In the framework of this project, monitoring of the environment and repository structures should provide requested information for its operation and its reversible management. This monitoring system also needs to answer to legal and societal expectations expressed.

Depending of the national context and the waste management strategy, the monitoring devices and installed equipment must further resist to the severe environmental conditions existing in a repository, which may include high temperatures, high pressures, humidity and/or submersion, chemically aggressive environments, and levels of radiation that may degrade electrical and optical cables performances. Typical requirements also include the longevity (several decades) of expected monitoring (without real possibility of accessibility to maintain equipment, except by robotized devices), the high level of needed confidence in signal reliability, and the absence of interference with barrier performances, in particular as pertaining to long-term safety. This is a key requirement of the monitoring system not to degrade the favorable conditions and expected performances for long-term safety of the repository.

To match these requirements, Modern2020 has launched an ambitious 4 years R&D program to ensure that reliable, durable, metrologically qualified and tested monitoring systems will be available at the time of repository construction to respond to specific monitoring objectives of member states.

This document aims to develop the results obtained in the development of new sensors dedicated to geological disposal purposes.



## Table of content

Abstract.....	3
Executive Summary.....	6
List of figures.....	14
List of Tables.....	19
Glossary.....	20
1. General Introduction .....	21
1.1 Background .....	21
1.2 Objective of the task 3.4 .....	21
1.3 Approaches.....	22
1.4 Scope of the document.....	23
2. Optical fiber technologies development .....	24
2.1 Optical fibers and related sensors: back to basics.....	24
2.1.1 Related specificities of optical fiber sensors.....	25
2.2 Radiation, H2 and pH sensors based on FBG technology (University of Mons) .....	26
2.2.1 Introduction .....	26
2.2.2 State of Art ((SOA) on Hydrogen and pH sensor based on based on FBG technology .....	27
2.2.3 pH sensor developed by UMONS .....	35
2.2.4 Concept description and methodology .....	39
2.2.5 Conclusion .....	40
2.3 Design and performances of a sensing system to provide distributed radiation, H2 strain and temperature measurements in geological repository environments (Andra, Xlim) .....	42
2.3.1 Introduction .....	42
2.3.2 Distributed optical fiber technology.....	43
2.3.3 Distributed Temperature sensing .....	45
2.3.4 Distributed hydrogen sensing.....	48
2.3.5 Distributed gamma sensing .....	57
2.3.6 Compatibility of temperature and strain OFS with harsh environment .....	60
2.4 Active DTS for investigations of thermal conductivity, density and water content in the EBS (Nagra)73	
2.4.2 General experimental setup.....	76
2.4.3 Calibration test .....	77
2.4.4 On-site verification of effects of shotcrete at Mont Terri .....	79
2.4.5 Summary .....	80



2.4.6	FE Experiment: Estimation of GBM state in June 2017 .....	81
2.4.7	Summary and conclusion .....	86
3.	Non-invasive techniques: .....	87
3.1	Introduction.....	87
3.2	Objectives.....	87
3.2.1	Reference scenario.....	88
3.2.2	Electromagnetic waves sensor .....	90
3.2.3	Gradiometric Sensor .....	94
3.2.4	Ultrasonic waves sensor .....	96
4.	Chemical sensors .....	101
4.1	Improvements and new developments on chemical measurements .....	101
4.1.1	Introduction .....	101
4.1.2	Description of the technology.....	102
4.1.3	Preparation of the samples .....	103
4.1.4	Compacting of the samples .....	104
4.1.5	Electrodes.....	104
4.1.6	Test benches .....	106
4.1.7	Results.....	107
4.2	Thermocouple psychrometers for water content measurement .....	111
4.2.1	Concept description and methodology .....	111
4.2.2	Experimental set-up.....	112
4.2.3	Final design.....	113
4.2.4	Electronics.....	113
4.2.5	Mechanical .....	114
4.2.6	Conclusion/Discussion/Summary.....	114
5.	Combined smart sensors .....	115
5.1	Objectives.....	115
5.2	Objectives.....	115
5.3	Mechanical setup .....	115
5.4	First version.....	117
5.5	Second version .....	118
5.6	Electronics .....	120
	References.....	124

## Executive Summary

---

### Introduction and Objectives

The Development and Demonstration of Monitoring Strategies and Technologies for Geological Disposal (Modern2020) Project aims to provide the means for developing and implementing an effective and efficient repository operational monitoring programme, taking into account requirements of specific national programmes. The main focus of the project is monitoring of the repository and repository near-field during the operational period to support decision making and to build further confidence in the post-closure safety case (including verification of the as-built repository through monitoring of processes in the short period following emplacement).

Deliverable D3.4 is the summary report for Task 3.4 of Work Package 3, which is focused on the improvement of the durability of monitoring sensors components (design, materials, armour, etc.) with the goal to extend their lifetime under aggressive conditions expected in the repository. In particular, the presence of ionising radiation and aggressive corrosion conditions has been considered. The development of integrated systems, especially using multi-parameters cables incorporating optical fibre sensors or combined sensors is shown. Non-invasive techniques is considered as an essential aspect of monitoring due to their advantages over common intrusive methods. The ambition includes an increase in the range of physical properties that are monitored in order to allow the means for cross correlating monitoring results. This task aimed to address several remaining generic issues not previously addressed in international collaborative projects.

### Waste management organisation expected technologies

In the First workshop of the Modern2020 project in Stockholm (Sweden), a summary of questionnaire responses relevant to monitoring technologies, including the specific WP3 technologies of interest to each WMOs, and justifications for this interest (e.g. examples of where and how such technologies could be used in planned monitoring strategies) has been presented and discussed. The main conclusion of the analysis was that there is interest from at least one WMO in each of the technologies being developed in WP3, as shown in Table 1.



Table 1: WMO interest in monitoring technologies proposed for investigation under WP3.

Technologies of interest/under consideration according to questionnaire responses: Green=yes, Red=no, Amber=maybe/more information needed, blank=not specifically mentioned or discussed	Andra	DBE-TEC	ENRESA	NRG	RWM	RWMIC/NUMO	Posiva	SKB	SURAO
<b>Transmission systems</b>									
High/medium frequency wireless data transmission systems									
Low frequency wireless data transmission systems									
<b>Energy storage</b>									
Energy harvesting based on low thermal gradients									
Energy storage devices									
Wireless energy transmission									
Miniaturised nuclear generators									
<b>New sensors</b>									
New generation optical fibre sensors based on quasi-distributed measurements based on cascaded fibre Bragg gratings									
Optical fibre cable for distributed measurements of four parameters (temperature, strain, hydrogen and radiation)									
New method to determine thermal conductivity, density and water content of the EBS based on distributed temperature sensing									
New method to determine water pressure in boreholes based on distributed temperature sensing and distributed strain sensing									
Thermocouple psychrometers for water content measurement									
Techniques for non-contact displacement measurement									
Chemical measurements (ion-selective electrodes for measuring ion activities)									
Combined thermal-hydrological-mechanical-chemical smart sensors (small combined cells to measure total pressure, temperature, pore pressure and humidity)									
<b>Geophysical methods</b>									
Seismic full waveform inversion									
Combined method based on electrical resistivity tomography and induced polarisation tomography									

**Detailed Approach**

R&D program can be detailed as follow:

Topic 1: Fiber optic technologies:

- Research on custom-made fibre Bragg gratings (FBGs) is made in order to adapt: (i) irradiation sensor based on FBGs photo-inscribed in specialty optical fibres by means of a femtosecond pulses laser, (ii) improve the hydrogen sensor based on FBGs surrounded by a catalytic sensitive layer made of tungsten oxide doped with platinum and (iii) develop pH sensors based on tilted FBGs covered with a micro-porous coating consisting of a pH indicator (bromophenol blue) encapsulated in a silica sol-gel matrix.
- Development (design, realization and tests) of an optoelectronic sensing chain to supply distributed measurements of four parameters: temperature, strain, hydrogen and radiation, separately or at the same time. We will take advantage of the huge influence of optical fibre dopants and primary coatings to enhance the influence of one only parameter while annealing the influence of the three other. To reach this ambitious goal, the system will rely on two or three scattering measurements, namely Brillouin, Rayleigh and Raman scatterings.
- Method development for fiber-optic distributed sensing of thermal conductivity, density and water content in the EBS by means of heatable fiber-optic cables as well as development of fiber-optic pressure cells for borehole applications.

Topic 2: non-contact techniques

- Research on non-contact techniques for new short-range displacement sensors to be buried into the engineered barriers system. This kind of sensors will solve the problem of having preferential paths in the EBS due to the use of standard extensometers.

Topic 3: chemical parameters



- Development/adaptation of ion-selective electrodes for measuring e.g. Ca<sup>2+</sup>, Mg<sup>2+</sup>, Na<sup>+</sup>, K<sup>+</sup>, S<sup>2-</sup>, and H<sup>+</sup> ion activities to monitor chemical processes in the long term. The research results will be compared with modelling, chemical analyses from dismantled samples and previous studies of the microstructure of compacted bentonites. After testing the electrodes used to work in compacted bentonite can be utilized to observe chemical parameters in laboratory or *in-situ* experiments.
- Development of new sensors based on thermocouple psychrometers operating under the more accurate dew point method to measure water content in the bentonite barriers when close to saturation state.

#### Topic 4: combined measurement

- Development of combined Thermal Humidity Mechanical Chemistry (THMC) sensors in order to reduce the volume and energy need of the sensors that does will be installed in the repository. Thus a small combined cell to measure total pressure, temperature, pore pressure and optionally humidity will be developed. Besides, it will be designed to eliminate the weak points of existing total pressure cells (the tube connecting the cell with transducer and its big size) while maintaining the same precision and accuracy. The proposed integration of transducers and electronics will improve the reliability by providing digital data.

#### Optical fiber sensors results

##### Optical Bragg sensors technologies under radaition

Optical fiber technology is a promising technique for sensing nuclear waste disposal sites. Indeed, silica-based fibers can be engineered to be either radiation resistant or radiation sensitive depending on the application. . Although hydrogen FBG sensors were successfully developed, radiation tests were not satisfactory on this technology and all samples died. The lack of adherence of the sensitive layer is the major problem that can explain the failure of the sensor but no conclusion can be drawn on their radiation robustness. pH sensors still require a lot of effort to be tested in radiation field. They should first be tailored for the pH range of 11-13, which is very challenging. Finally, polymer optical fibers and gratings were tested as an alternative to silica-based fibers. First results show that these fibers are radiation sensitive and survive 100 kGy.

Based on the presented design and results, we can imagine the future system to obtain distributed measurements of strain, temperature, hydrogen and radiation.

##### Distributed OFS technologies for temperature measurement

Within MODERN2020 projet, Andra focused on “distributed optical fiber sensor”. It designates the case in which the silica-based material becomes a sensor. Monitoring with a single fiber can provide information all along the structure behaviour, and thus overcome limitations of traditional sensors, whose information is restricted to local effects.

Temperature measurement using Raman effect is a mature technologies for different industries, in order to qualify the techniques to geological disposal condition different evaluation has been performed which conduct to the following conclusion:

- Carbon-primary coating is mandatory to prevent hydrogen diffusion. Its efficiency was experimentally demonstrated. Its durability under harsh environment remains to be evaluated.
- F-doped fiber is mandatory to reduce the Radiation induced attenuation (RIA) but is not sufficient to suppress dramatic radiation impact on temperature sensing. Double-ended configuration proved to be efficient, at the expense of temperature uncertainty, which reach 5 °C at 1 MGy.



- Maximal distance range remains to be quantified. We expect more than 100 m even at 1 MGy received dose.

Perspectives of the work are

- Evaluation of coupled temperature and radiation. Literature proves that temperature limits the negative influence of radiation. Hence, our results are pessimistic and we can be confident that temperature uncertainty will be smaller than 5° C.
- Evaluation of the influence of hydrogen on the irradiated carbon-coated samples.

As a back-up solution for temperature sensing, we evaluated the possibility to pair Brillouin or Rayleigh scattering with a loose tube (enclosing a singlemode fiber), to get rid of strain influence and be able to provide temperature measurement only. We proved that loose tube is efficient to isolate the sensing fiber from mechanical stress if implementation is carefully realized which could be challenging in some application. It is an interesting back-up solution for temperature sensing, since temperature uncertainty actually remains similar for the three scatterings after radiation impact.

#### Distributed OFS technologies for Strain measurement

Continuously distributed sensors based on Brillouin scattering is used to measuring Strain. Evaluation of the performance of this technology to harsh condition has been evaluated in the project. The following results has been found

- Carbon-primary coating is mandatory to prevent hydrogen diffusion. Its efficiency was experimentally demonstrated. Preliminary test have revealed a degradation of carbon-coating hydrogen-hermiticity after 10 MGy total dose. The results should be repeated and confirm for different doses rate and carbon-coating types.
- F-doped fiber is required to reduce the RIA and Brillouin frequency shift induced by gamma radiation. The Brillouin frequency shift is in the order of 4 MHz at 1 MGy for the Ge-doped fiber and only 2 MHz with the developed F-doped fiber, which approximately corresponds to 40  $\mu\text{m}/\text{m}$  maximal error in strain measurement. Coupled effects of temperature and radiation was evaluated. Temperature reduces the negative impact of radiation on distributed sensors exploiting the Stimulated Brillouin Scattering. At 80 °C, 100 °C and 120 °C, compared to room temperature, the radiation-induced attenuation is significantly reduced and maximal distance range is improved. It remains to be quantified.

Rayleigh scattering has proved to be a very promising solution for strain sensing. It is even less affected by radiation than Brillouin scattering. With the custom fiber based on F-dopants instead of Ge-dopants, the influence of radiation on Rayleigh frequency shifts is as small as -4 GHz, or 2.5  $\mu\text{m}/\text{m}$  error, whatever the working temperature is (80, 100 or 120 °C).

#### OFS Cable qualification

The qualified optical fiber has been inserted into a strain sensing cable. It has been placed under irradiation. We plan to evaluate if sensing cable performances are similar with naked fiber ones in Autumn 2018.

Regarding distributed radiation sensing, we tested three singlemode optical fibers selected for their various sensitivities towards radiation. Al-doped sample is clearly the most radiation-sensitive: it could provide distributed measurement until a dose of 470 Gy. Then the GeP-doped fiber should be favored. It worked until 4 kGy. The Ge-doped could be measured till the end of the irradiation, despite lower sensitivity. The optical fiber lengths and the working wavelength are two other parameters to adjust to the application. However, while obtaining these calibration curves, the strong dependence of curing effect and coupled temperature and radiation influences was demonstrated. As a consequence, this work must be reproduced taking into consideration many more parameters. We cannot conclude yet on the

best solution for underground repository monitoring. Many research teams have recently published on this topic and we can now expect rapid progresses.

Hydrogen OFS sensors

Hydrogen sensing was initially envisioned with palladed silica optical fibers paired with Brillouin scattering in microstructured optical fiber (PCF). XLIM, in charge of this topic, established a model and provided calibration curves. Many special fibers were realized. A strong collaboration with University of MONS has been implemented to perform on-line measurements, during hydrogen exposure, for several temperature and pressure conditions. Optical fiber losses compromise the technical solution: presently, samples length cannot exceed 10 m and measurements remain very noisy. Xlim explored a back-up solution, based on birefringence measurement in palladed polarization maintaining fiber. Modeling and experiments were performed. Feasibility of hydrogen measurement has been demonstrated. A patent application has been submitted in November 2017 by Xlim and Andra on this new sensing scheme. Now publications are on progress. There remains to make hydrogenation cycles, with smaller amounts of hydrogen. Based on these developments, we published [59][60][61][71] and patented [83] the results.

Suggested Geological disposal configuration for distributed measurement

Figure 1 summarizes the proposed distributed measuring system. It is only a schematic and we are still far from an industrial system:

- The first three boxes are commercial equipment’s, yet separated. Distributed birefringence measuring device is not off-the shelf but focuses many research developments and should become an industrial product in the coming years.
- The fibers are almost qualified but naked fibers would not endure repository cell construction. The strain sensing cable developed in the project will surely prove its durability in the coming months! For temperature and radiation sensing, blowing fibers into capillaries enables (i) placing sensors after the construction stage, and (ii) maintenance. Huge developments are not required to implement this solution; it would be an efficient and promising scheme. The main research topic is hydrogen sensing. Even if rapid and important results are obtain in laboratory, how to implement the sensitive optical fiber next to the wastes without deteriorating at emplacement should focus attention.

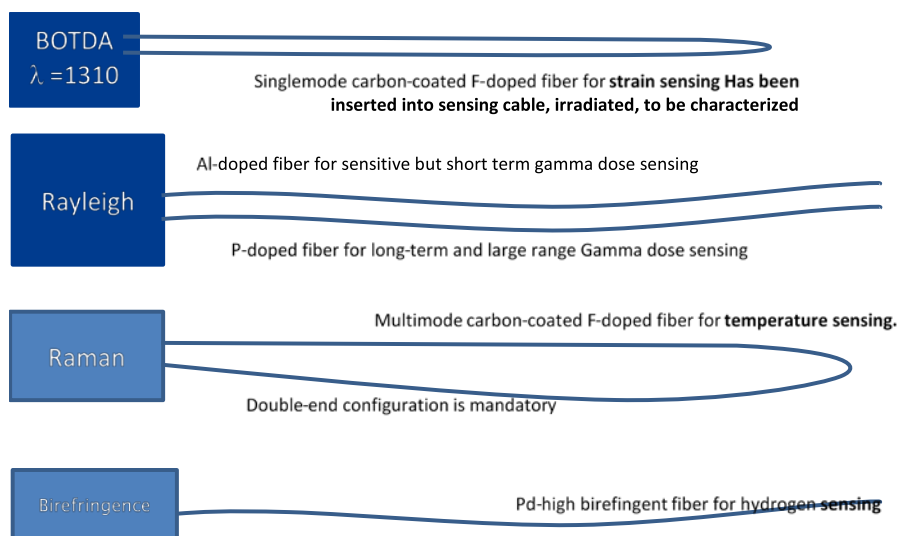


Figure 1: Schematic of the completely sensing system to provide strain, temperature, hydrogen and radiation distributed sensing

Application of the heated fiber-optic and DTS

Application of the heated fiber-optic and DTS (active DTS) to monitor the state of GBM was examined through a series of laboratory tests at the Grimsel Test Site (GTS) and Mont Terri rock laboratory (FMT) in Switzerland. The experimental setting parameters to obtain thermal responses that best reflect the GBM conditions were first identified. It was then followed by calibration of the active DTS tool to the dry density and degree of saturation of the GBM, and evaluation of effects of shotcrete.

The FO cable installed in the FE tunnel at the Mont Terri rock laboratory was then heated with the recommended setting parameters and the temperature responses were closely analyzed to estimate the state of the GBM along the FO cable in the FE tunnel. Finally, the results from the early heating tests in the FE tunnel was interpreted to extract information about the initial dry density at the time of the emplacement.

As summarized below, the active DTS results showed positive insights for estimating the dry density and saturation of the GBM materials.

### **Non invasive techniques**

Preliminary results indicate that all approaches could be suitable to solve the studied problem, yet several technical issues are to be faced before defining the best solution, which will be the result of a trade off among accuracy, depth of penetration and complexity of the detection system.

In this report we have analysed three different approaches to the problem based on three different physical principles: ultrasound waves, EM waves, gravity.

It is not possible here to give a direct comparison among them in terms of pros and cons, because the maturity level of the correspondent technology has not here considered, being well beyond the scope and the objectives of this work.

The objective of this activity has been to understand potential approaches to the individuation of alternatives to cable or contact existing technologies.

We have here individuated three different physical choices. Not all have been investigated until the final definition of a sensor, because even arriving to a real study of feasibility imposes the realization of experiments and tests that require the availability of significant resources.

The aim of this work has been an overview based both on the literature and on some original studies conducted by the authors, in order to explore potential applications that could deserve more attention in the future also thanks to the results contained in this report.

The ultrasound waves technique can be considered a mature technique already used in several applications for similar purposes. But in order to arrive to a real study of feasibility on the realization of a contactless sensor to be used for displacements measurement, more effort is required in order to design and test a prototype in a realistic application. The scheme here presented can be considered as a hint to start with.

On the other hand, the gradiometric technique here proposed should be considered at this stage as a pure conceptual proposal, yet a very promising one. It requires a strong effort to be transformed in a realistic prototype. The technique seems to show several advantages:

- Measures are also possible through a material discontinuity or vacuum
- Measures are also possible through metallic shielding
- Possible Hard Rad-Hard version (with remote electronics) up to 100Krad

- Easy to calibrate

Nevertheless, several issues should be fixed, first of all the interference effects with other (natural or artificial) massive systems.

More attention has been paid here to the third approach, i.e. *EM waves*. This possibility has been widely considered both on the theoretical and the simulation point of view. Some considerations could then be given as a conclusion of the work.

The GPR and NMR methods have been considered. Each method must be evaluated in terms of *depth of penetration* and *accuracy* of the detected signal. This requires to perfectly knowing the dielectric medium the signal passes through. In order to do that, a specific characterization of the dielectric parameters should be performed. This is a crucial point. Several works proposed validated models that could be used in the simulations.

It should be underlined that the diagnostic systems based on the propagation of RF waves are limited from the maximum depth of penetration. This in turn is inversely proportional to the AC conductivity of the medium penetrated by the RF wave and therefore inversely proportional to the water concentration of the medium. In the presence of non-negligible water concentrations, it is therefore necessary to reduce the frequency of the RF wave so that it penetrates in the medium and can be detected with sufficient signal-to-noise ratio. In this way, however, the spatial resolution (limited by diffractive phenomena), tends to compressively decrease, despite the length of the RF wave being compressed in the presence of media with a higher water content, as shown in figure 12.

On the other hand, the use of well-defined topological configurations that allow the propagation of stationary electromagnetic waves and the knowledge of the electromagnetic properties of the materials involved, enhances the spatial resolutions below the diffractive limits. In this case, although the medium in which the electromagnetic field propagates is dissipative, by choosing wavelengths of at least one order of magnitude less than the geometric dimensions of the considered scenario, a series of resonant modes can be established (geometrically overmodal structure).

However, the presence of water concentrations will not allow to obtain resonant modes with high factors of merit. Therefore, the frequency spectrum of the reflected signal will have a finite band. Yet, the frequency band is not very narrow with an approximately linear phase drift around the central frequency (if the modes have central frequencies sufficiently distant from each other). A modal analysis of the reflected signal, when the position of one of the objects changes, will allow to detect variations in amplitude and phase that in principle are linked to the object deviation. The resolution depends here on the factor of merit of the analyzed resonant mode, which in turn is inversely proportional to the water concentration of the medium. The linearity of the phase shift with the displacement of the analyzed object and the corresponding sensitivity require a preliminary analytical and numerical study of the scenario.

Preliminary simulation results presented in this work confirm that as the frequency increases, the depth of penetration tends to dramatically reduce. But decreasing the frequency means that a higher antenna should be used. As a consequence, the design of the sensor should be done by a trade off between accuracy and geometrical dimension of the sensor (that should be designed so as to be easily included in the proposed environment). All possible combinations in terms of frequency range have been reported on Table 3. A detailed design could be done only after a thorough experimental campaign. The presented table could be used as a basic reference guide to start with.

## **Chemical sensors**

### **Ions activities**

Direct measurement of ion activities in pore water of compacted bentonite are exceedingly difficult to perform because of the huge swelling pressure, which most of the sensors cannot withstand, also the low amount of the free water available for the sensors and long measuring times. VTT has developed a methodology for measuring pH and Eh in compacted bentonite. The aim of this study is to broaden the method of in-situ measuring relevant ion activities in the pore water of compacted bentonite. In this study commercial and house-made Ag/AgCl Cl-sensitive electrodes and Na sensitive “Nasicon” electrode with solution filling are tested in batch experiments, as well, H<sup>+</sup> sensitive IrO<sub>x</sub> electrode in diffusion experiment.

### **Water content**

A new system to measure relative humidity through dew point method using psychrometer sensors have been developed and tested. It has demonstrated to be sensitive to changes in relative humidity using calibrated samples.

The resulting system is low price and size, and it presents versatile features to be adapted to different cases of use, providing different working modes and control interfaces.

The developing process has not been easy but very profitable, and results are encouraging. The physics involved are very interesting, but it is not trivial to obtain good results from the very beginning. Noise and other parasitic effects have caused the biggest challenges during the development, and big effort has been done to mitigate them to the minimum.

There is stillroom for improvements in psychrometer sensors. Methods like the one proposed in this case open new possibilities for measurement systems. Thus, it is important to dedicate efforts to investigate and develop new sensors because of the new opportunities hidden behind them

### **Smart sensors in combined measurement**

There is a quite big range of total pressure cells on the market for the measurement of total. They usually come in 230mm diameter cylinder form with transducer attached via steel tube. Typical transducers used are vibrating wire (GeoKon), pneumatic (GLOTZL) or lately fibre optics. The CTU developed and used such pressure cells for civil engineering applications over 20 years now. Although these sensors are reliable, there are some disadvantages of their usage for EBS. In particular, their size and the necessity to use them in combination with other sensors to get full state of EBS, which is even more space demanding and measurements, are done in different places. Together with cabling and necessary data loggers, system gets complicated.

The new cell is targeted especially (but not exclusively) for measurements in the EBS system and to mitigate these problems. Although it is named as pressure cell, it is designed as all in one package. Along total pressure sensor, it integrates temperature, pore pressure sensor, RH sensors and electronics in the same package. This way the complete picture of EBS state can obtained at once with much lower demands on space, cabling and power.

## List of figures

---

Figure 1: Schematic of the completely sensing system to provide strain, temperature, hydrogen and radiation distributed sensing .....	10
Figure 2: The electromagnetic spectrum: optical fibers convey visible and closed infrared light .....	24
Figure 3: Structure of a silica optical fiber .....	24
Figure 4 : Description of MM fiber and SM fiber .....	25
Figure 5: Diagram of a fibre-optic measurement system: An acquisition device is connected to an optical fibre containing sensors used to convey information. The sensors are local (red arrows), long-based (where the sensor corresponds to the distance between arrows), or distributed (where the fibre itself becomes a sensor).....	26
Figure 6: Geometrical structure of a singlemode optical fiber.....	26
Figure 7: Basic principle of uniform fiber Bragg grating. ....	27
Figure 8: Experimental setup used to test FBGs response under H2.....	30
Figure 9: Picture of the h2 test bench. ....	30
Figure 10: Transmitted spectrum of a 4 cm long FBG in response to different H2 concentrations in dry air at ambient temperature .....	31
Figure 11: Shift of the Bragg wavelength as function of the H2 concentration in dry air at ambient temperature for different physical lengths of the gratings.....	31
Figure 12: Uniform FBG superimposed in a LPBG for H2 detection. ....	32
Figure 13: Bragg wavelength shift as a function of the H2 concentration in wet air for a hybrid sensor. ....	33
Figure 14: Bragg wavelength shift as a function of the H2 concentration at different temperatures.....	33
Figure 15: Scheme of a tilted fiber Bragg grating and its mode couplings. ....	35
Figure 16: Bromophenol: left acidic form, right alkaline form.....	36
Figure 17: Experimental setup used to measure the transmitted amplitude spectra of the TFBG. ....	37
Figure 18: Transmission spectrum of the TFBG at different pH values.....	38
Figure 19: Peak-to-peak amplitude of the transmission spectrum at 1562 nm at different pH values. Experimental points and sigmoidal fitting .....	38
Figure 20: Response to pH change: Peak to peak amplitude around 1562 nm versus time for a change from pH = 3 to pH = 10.2 and pH = 10.2 to pH = 3.1 .....	38
Figure 21: Sketch of a truly-distributed measuring system .....	43
Figure 22: Spectrum of backscattered light inside an optical fibre: higher frequencies are called anti-stokes, shorter are called Stokes components .....	43
Figure 23: Schematic experimental arrangement for evaluating performances of DTS Raman interrogator .....	46
Figure 24: Temperature trace measured with the SILIXA device after calibration at 23°C. ....	46

Figure 25: MTE measured with the sensing optical fiber stabilized at Four different temperatures - (23 °C, 3 °C, 40 °C and 60 °C) .....	47
Figure 26: Brillouin spectra for a G652 fiber before and after hydrogen exposure (13 days 150 bars, 25 °C) .....	49
Figure 27: Brillouin Frequency shift as a function of hydrogen concentration in the optical fiber core..	49
Figure 28: SEM pictures of cross-sections of three optical fibers with Pd particles embedded into the silica cladding realized by the powder in tube process: (a) a SiO <sub>2</sub> -GeO <sub>2</sub> core step index fiber. (b) a pure silica core microstructured fiber; (c) a SiO <sub>2</sub> -GeO <sub>2</sub> step index core with a microstructured cladding fiber; (d): zoom-in the cladding region of the fiber. ....	50
Figure 29: (a) Scheme of H <sub>2</sub> diffusion process into a silica fiber, (b) Evolution of H <sub>2</sub> concentration (normalized to saturation concentration) in the fiber center for different fiber diameters (80 μm and 125 μm) exposed to H <sub>2</sub> gas under a pressure 175 bars and at different temperatures (50 °C and 80 °C). (c) Evolutions of H <sub>2</sub> concentration at saturation and of the variation of the refractive index of the fiber core, versus H <sub>2</sub> gas pressure applied on the exposed fiber, at different temperatures. (d) Variation of the refractive index of the fiber core induced by H <sub>2</sub> at saturation for different pressures versus the temperature .....	51
Figure 30: Time-evolution of (i) the Rayleigh frequency shift (grey squares with left axis), (ii) the Brillouin frequency shift (dark squares with left axis), (iii) the Bragg grating wavelength (opened grey triangles with right axis), (iv) calculated normalized concentration of H <sub>2</sub> (dark line with right axis), during H <sub>2</sub> out-gassing of the SMF (exposed up to 200 bars of H <sub>2</sub> at 80 °C during 60 hours).....	52
Figure 31: sketch of the special fiber with Pd in the cladding and SEM pictures of the three drawn fibers .....	52
Figure 32: Comparison of Brillouin peak shift for G652, HS31 et HSPCF Fibers in desorption. ....	53
Figure 33: measured Brillouin frequency of the palladed fiber HS26 during hydrogen loading.....	54
Figure 34: Comparison of Birefringence and hydrogen concentration in SAPs versus time. ....	55
Figure 35: Measured Interferometric peak variation for FPO (black) and FP7 (red), versus hydrogenation time. ....	55
Figure 36: Wavelength peak shift position versus H <sub>2</sub> concentration in SAP. ....	55
Figure 37 OTDR trace at 1550 nm measured before irradiation, at the starting and at the end of the irradiation. The three fibers have been spliced in series.....	58
Figure 38: extracted RIA time evolutions at 1550 nm.....	58
Figure 39: RIA spectral dependences measured in the GeP sample at different times during irradiation .....	59
Figure 40: Comparison between the RIA growth kinetics at 1550 nm for the GeP fiber deduced from either OTDR or spectral measurements. ....	59
Figure 41: Measured temperature obtained from Raman scattering in a 100 m long sample of F-doped fiber, pristine (blue) and exposed to radiation doses.....	60
Figure 42: Measured Brillouin frequency shift for standard fiber with Ge dopants (left) and F-doped fiber (right) [47].....	61
Figure 43: Influence of hydrogen exposure on Raman scattering.....	61

Figure 44: Picture of the Neubrescope instrument and its multiplexor bought with modern2020 funds, to enable measuring Brillouin and rayleigh scatterings in 8 optical lines sequentially and automatically ..... 63

Figure 45: strain sensing cable developed within MODERN2020 project: Schematic of the cross section (left) and picture of the cable prior splicing, longitudinal view ..... 63

Figure 46 Pictures of the silicone with the optical sample and thermocouple (left) and the irradiation test (right) prior to the radioactive rod emplacement with optical fibers heated at three controlled temperatures..... 66

Figure 47 : Example of raw measurements: Brillouin frequency shift along one optical line (2 samples at 80 °C) while irradiated ..... 66

Figure 48 Brillouin frequency shifts measured in the two samples (Ge- and F doped fibers) placed at ambient temperature and the measured ambient temperature as a function of the received dose ..... 67

Figure 49 Brillouin frequency shift in Ge-doped fibers at different temperatures: total dose trend (left) and zoom at irradiation start (right)..... 68

Figure 50 Radiation influence on the Brillouin central peak amplitude on the four samples at 1 MGy. A linear fit is plotted along the traces. .... 68

Figure 51 Radiation induced attenuation for the Brillouin gain spectrum central peak amplitude ..... 69

Figure 52 Brillouin frequency shift in F-doped fibers at different temperatures as a function of the received gamma dose, up to 1 MGy ..... 69

Figure 53: Schematic of the whole sensing system to provide strain, temperature, hydrogen and radiation distributed sensing ..... 72

Figure 54: Schematic cross-section of the heatable FO cable (taken from Brugg Cables, 2015 [85]) ..... 74

Figure 55 : The main DTS unit. Silixa Ultima-S (Silixa Ltd. 2015[103])..... 74

Figure 56: Temperature resolution over a distance of 5 km with 0.127 m sampling resolution..... 75

Figure 57: Electrical current generator ..... 75

Figure 58: Grain size distribution of mixture 2 (Garitte et al. 2015)..... 76

Figure 59: Schematic image of the experimental setup ..... 76

Figure 60: The FO cable fixed along the centerline of the test box ..... 77

Figure 61 : Heatable FO cables (red) installed in the FE tunnel. .... 79

Figure 62: (left) Heating test site in Gallery 08 at FMT Switzerland (right) Schematic illustration of the heating test setup ..... 80

Figure 63: FO cable installed configuration. .... 82

Figure 64: Side view of FO cable configurations ..... 82

Figure 65: Behind the concrete plug ..... 82

Figure 66: Temperature profiles at different times along the FO cable with 1.9 W/m (two ways, going in and coming out)..... 83

Figure 67: Temperature profiles along the FO cable (one way) at different times..... 84

Figure 68 : Temperature changes at different times along the FO cable with 1.9 W/m..... 84

Figure 69: Temperature changes along the FO cable in ISS at different times with 1.9 W/m..... 85



Figure 70. Extensometers (EA1/1 & EA1/2) installed in EB experiment .....	88
Figure 71: Extensometers (white pipes) installed in FE experiment .....	88
Figure 72 : Schematic of potential implementation of the sensor. (a) Overall view from the tunnel. (b) View inside the hole .....	89
Figure 73: Dielectric, conductivity and wave length spectra of the clay-rock from series 4 (S4) as a function of frequency at different states (results obtained with the IFTTAR cell measured with Anritsu VNA as well as R&S and Agilent PNA).....	91
Figure 74 : Simulation scenario in a reduced scale for a canister where a propagating EM field is generated by one dipole antenna.....	93
Figure 75: Reflecting coefficient (S11 [dB]) for the scenario presented in Figure 69 .....	94
Figure 76: Schematic of potential implementation of the sensor .....	95
Figure 77. Ultrasound Sensor Scheme.....	96
Figure 78. Shaft schematics and cross section .....	97
Figure 79. Wave speed contours at a cross-section depth of 1.34 m.....	98
Figure 80. Generalized microstructure of (MX-80) bentonite[146] Extra layer water as non-IL water. ..	101
Figure 81. Schematic presentation of the test bench for ion-selective electrode batch testing. [140]..	103
Figure 82. Bentonite initial Cl content effect on Cl activity in compacted samples when Cl accessible porosity is taken into account (Muurinen & Carlsson, 2013). The chloride activities were calculated based on the species in the Thermoddem database when using the <i>PHREEQC</i> code. ....	103
Figure 83. Purified Ca-montmorillonite on the left, MX-80 and grinded Na- and Ca-montmorillonites purified from MX-80 on the right.....	104
Figure 84. Diffusion cells for wetting compacted bentonite samples. On the right diffusion cell where external water sources are below and above of stainless steel sample holder. Liquid is separated from bentonite sample by sinters.....	104
Figure 85. On the right side house-made liquid filled Na-sensitive Nasicon and pH sensitive IrOx electrodes. On the left electrodes ready for experiments. ....	105
Figure 86. Schematic presentation of the liquid filled ion selective electrode.....	106
Figure 87. Test bench for batch experiments.....	106
Figure 88. Photo of the diffusion cell. The diameter of the bentonite sample is 40 mm and the height 50 mm. The electrodes are 5, 10 mm from the solution-bentonite interface. The volume of the solution in the external vessel is 230 ml. ....	107
Figure 89. Measured chloride activities with Ag/AgCl electrodes versus calculated Cl activity by PhreeqC based on measured chloride content and Cl accessible porosities at studied dry densities in samples. ....	108
Figure 90. Measured Cl concentration with Ag/AgCl electrode in the porewater of MX-80 sample compacted to a dry density of 1.5 g/cm <sup>3</sup> . The Cl accessible porosity of 7 % match with measured values when per total water volume gives a clearly lower values.....	109
Figure 91. Liquid filled Na electrode calibration curves before and after experiments. Potential versus SHE were measured in solutions with different Na activities. ....	109

Figure 92 : Measured activity of Na <sup>+</sup> in compacted bentonite saturated with 0.1 M Na <sub>2</sub> SO <sub>4</sub> solutions. According to PhreeqC calculations the activity of Na <sup>+</sup> in this kind of solution should be about 0.12. Na1 as calibration 1 before experiments and Na2 as calibration 2 before experiments. ....	110
Figure 93: pH at different depths in bentonite and in the external solution of the diffusion cell sample. The solution chemistry was changed at 271 days from low-pH to high-pH.....	111
Figure 94 Isolated sample chamber to perform measurements .....	112
Figure 95 Complete system set up for prototype .....	113
Figure 96 Software interface .....	113
Figure 97: Proposed electronics.....	113
Figure 98: Mechanical envelope of the sensor.....	114
Figure 99: Conceptual design as presented during WP3 workshop (2015) (images not to scale) .....	117
Figure 100: Cross section of the first version of the body design (images not to scale) .....	117
Figure 101: (On the left) First body version of smart cell (stainless steel body; (on the right) 3D printed prototype.....	118
Figure 102: First prototype test in press (heat toleration test in progress.....	118
Figure 103: Cross section of the second version of the body design (images not to scale).....	119
Figure 104: 3D model.....	119
Figure 105: 2nd revision smart cells (cell on the left designed for LTRBM).....	120
Figure 106: Block diagram of the core part of the smart sensor cell .....	121
Figure 107: Block diagram of supply, interfaces and outer connection of the smart sensor cell .....	122
Figure 108: Bottom view of the PCB .....	122
Figure 109: First version of the cell electronics compartment (SHT-25 is pulled out from its measuring place).....	122

## List of Tables

---

Table 1: WMO interest in monitoring technologies proposed for investigation under WP3.....	7
Table 2 : Comparison of hydrogen sensors .....	27
Table 3 : Comparison of pH sensors .....	35
Table 4. Main parameters to be monitor in the underground repository.....	42
Table 5. Typical performances of distributed temperature and sensing systems based on Rayleigh, Brillouin and Raman scatterings in optical fibers. ....	44
Table 6. Optical fiber characteristics and measured scatterings under hydrogenation. ....	52
Table 7. realised birefingent fibers.....	55
Table 8 : Setting parameters examined.....	77
table 9 : Selected conditions in three test boxes.....	80
table 10: Cable meters for Silixa DTS unit at selected points .....	83
table 11 : Comparison among different diagnostic methods in terms of all relevant parameters .....	91
Table 12 : Measured chloride activities by Cl <sup>-</sup> selective electrodes for different densities and salt solutions. ....	108
Table 13 : Results on basic test measurement on cell electronics .....	123



## Glossary

---

CW continuous wave.

CYTOP amorphous fluoropolymer.

EBS engineered barrier system.

FBG fiber Bragg grating.

HLW high level waste.

ILW intermediary level waste.

LPBG long period Bragg grating.

LPG long period grating.

PMMA poly(methyl methacrylate).

POFBG polymer fiber Bragg grating.

RIA radiation induced absorption.

SMF standard singlemode fiber.

SMF-28 standard singlemode fiber from Corning.

UV ultra-violet.

WDT wireless data transmission systems.

Cigéo future French underground repository for high level and intermediate level long-lived radioactive wastes

BGS Brillouin gain shift

DTS Distributed Temperature Sensing device

H<sub>2</sub> hydrogen

HiBi

MM-Fibers (MultiMode)

MTE Mean trueness error

OFS Optical fiber sensor

Pd Palladium

RIA Radiation induced attenuation

RT Room temperature

SAP Stress Applying Parts

SBS stimulated Brillouin scattering profiles

SEM Scanning Electron Microscopes

SMF singlemode fiber

URL Underground Research laboratory

VWS Vibrating Wire sensors

# 1. General Introduction

---

## 1.1 Background

The Development and Demonstration of Monitoring Strategies and Technologies for Geological Disposal (Modern2020) Project is a European Commission (EC) project jointly funded by the Euratom research and training programme 2014-2018 and European nuclear waste management organisations (WMOs). The Project is running over the period June 2015 to May 2019, and 28 WMOs and research and consultancy organisations from 12 countries are participating.

The overall aim of the Modern2020 Project is to provide the means for developing and implementing an effective and efficient repository operational monitoring programme, taking into account requirements of specific national programmes. The Project is divided into six Work Packages (WPs):

- WP1: Coordination and project management.
- WP2: Monitoring programme design basis, monitoring strategies and decision making. This WP aims to define the requirements on monitoring systems in terms of the parameters to be monitored in repository monitoring programmes with explicit links to the safety case and the wider scientific programme (see below).
- WP3: Research and development of relevant monitoring technologies, including wireless data transmission systems, new sensors, and geophysical methods. This WP will also assess the readiness levels of relevant technologies, and establish a common methodology for qualifying the elements of the monitoring system intended for repository use.
- WP4: Demonstration of monitoring implementation in repository-like conditions. The intended demonstrators, each addressing a range of monitoring-related objectives, are the Full-scale in situ System Test in Finland, the Highly-active (HA) Industrial Pilot Experiment in France, the Long-term Rock Buffer Monitoring (LTRBM) Experiment in France, and the Full-scale Emplacement (FE) Experiment in Switzerland. An assessment and synthesis of a number of other tests and demonstrators will also be undertaken, and this will include consideration of the reliability of monitoring results.
- WP5: Effectively engaging local citizen stakeholders in research and development (R&D) and research, development and demonstration (RD&D) on monitoring for geological disposal.
- WP6: Communication and dissemination, to include an international conference, a training school, and the Modern2020 Synthesis Report.

This report is Deliverable D3.4 of the Modern2020 Project and is the summary report for Task 3.4 (WP3), the fourth of six tasks in WP3. WP3.4 aimed to develop research on new sensors to measure relevant parameters when suitable probes do not exist or develop new techniques and probes when the existing ones do not comply with the required performance.

## 1.2 Objective of the task 3.4

Based on the previous work [3.], one major goal of Modern2020 EU project was the adaptation of the existing technologies or the development of new ones for specific monitoring objectives, host rocks and repository concepts, for the monitoring of specific parameters, and for improving their long-term performance.



About the development of news sensors, only high priority research activities has developed in the project by the partners. The research activities divided in two groups:

- Topic 1: Technologies based on optical fiber. Optical fibre sensors (OFS) are found to be exceptional tools, as they enable distributed measurements, thus providing data over the entire structure. Monitoring with a single fibre can provide information all along the structure behaviour, and thus overcome limitations of traditional sensors, whose information is restricted to local effects. Moreover, optical fibre's small size enables one to reduce invasiveness. Remote sensing would enable the maintenance of the optoelectronic devices during the facility lifetime; only the optical fibre, that is known to be more resistant than electronics, can be exposed to the harsh conditions during the operating period.
- Topic 2 : Non-invasive techniques : Harsh conditions suggest the possibility to study alternative method for measurements, for example methods not using cables or buses for detecting relevant. More in general, it is better to enlarge the investigation range to include not only wireless technologies (i.e. EM waves) but also other physical techniques coming from non-EM physical principles, provided that the connection between the detected parameters and the detection system is a non-contact one.
- Topic 3: Chemical measurement techniques: At lot of new challenges has been attached to the development of chemical sensors dedicated to the monitoring of geological facility in addition to the classical ones (sensitivity , selectivity , stability)
- Topic 4 : Smart Sensing Technology: The design, fabrication, and construction of smart structures is one of the ultimate challenges in the structure health monitoring. Smart sensors offer integrated approaches with innovative sensing principle, communication system and pre-analyse treatment is the future of the structure health monitoring. The development of smart sensors for GDF is considered has an interesting perspective about intrusiveness.

## 1.3 Approaches

For each specific R&D topic, the d program can be detailed as follow:

### Topic 1: Fiber optic technologies:

- Research on custom-made fibre Bragg gratings (FBGs) in order to adapt an irradiation sensor based on FBGs photo-inscribed in specialty optical fibres by means of a femtosecond pulses laser, improve the hydrogen sensor based on FBGs surrounded by a catalytic sensitive layer made of tungsten oxide doped with platinum and develop pH sensors based on tilted FBGs covered with a micro-porous coating consisting of a pH indicator (bromophenol blue) encapsulated in a silica sol-gel matrix.
- Development (design, realization and tests) of an optoelectronic sensing chain to supply distributed measurements of four parameters: temperature, strain, hydrogen and radiation, separately or at the same time. We will take advantage of the huge influence of optical fibre dopants and primary coatings to enhance the influence of one only parameter while annealing the influence of the three other. To reach this ambitious goal, the system will rely on two or three scattering measurements, namely Brillouin, Rayleigh and Raman scatterings.
- Method development for fiber-optic distributed sensing of thermal conductivity, density and water content in the EBS by means of heatable fiber-optic cables as well as development of fiber-optic pressure cells for borehole applications.

### Topic 2: non-contact techniques

- Research on non-contact techniques for new short-range displacement sensors to be buried into the engineered barriers system. This kind of sensors will solve the problem of having preferential paths in the EBS due to the use of standard extensometers.

### **Topic 3: chemical parameters**

- Development/adaptation of ion-selective electrodes for measuring e.g. Ca<sup>2+</sup>, Mg<sup>2+</sup>, Na<sup>+</sup>, K<sup>+</sup>, S<sup>2-</sup>, and H<sup>+</sup> ion activities to monitor chemical processes in the long term. The research results will be compared with modelling, chemical analyses from dismantled samples and previous studies of the microstructure of compacted bentonites. After testing the electrodes used to work in compacted bentonite can be utilized to observe chemical parameters in laboratory or *in-situ* experiments.
- Development of new sensors based on thermocouple psychrometers operating under the more accurate dew point method to measure water content in the bentonite barriers when close to saturation state.

### **Topic 4: combined measurement**

- Development of combined Thermal Humidity Mechanical Chemistry (THMC) sensors in order to reduce the volume and energy need of the sensors that does will be installed in the repository. Thus a small combined cell to measure total pressure, temperature, pore pressure and optionally humidity will be developed. Besides, it will be designed to eliminate the weak points of existing total pressure cells (the tube connecting the cell with transducer and its big size) while maintaining the same precision and accuracy. The proposed integration of transducers and electronics will improve the reliability by providing digital data.

## **1.4 Scope of the document**

This Modern2020 report, identified as D3.4, is the final technical report of the Task 3.4 of project Modern2020. The aim of this report is to synthesize the progress achieved in the Task 3.4 by Andra, Arquimea, CTU, EDF-DTG, EGIS, ENEA, ENRESA, EURIDICE, NAGRA, TUL, UMONS, XLIM, & VTT.

Section 2 summarizes the four studies dedicated to fiber optics technologies

Section 3 present the investigation of possible non-contact techniques for displacement measurement.

Section 4 summarizes the two studies dedicated to the development of a new psychrometer for water content measurement and the development of selective electrodes for the identification of ion

Section 5 summarizes the combined approaches for the development of a smart sensor.

## 2. Optical fiber technologies development

### 2.1 Optical fibers and related sensors: back to basics

An optical fiber **Erreur ! Source du renvoi introuvable.** is a waveguide the size of a single hair (0.1 mm) that enables conveying light, i.e. an electromagnetic wave with frequencies on the order of 100 THz. The breakthrough of this technology occurred in the 1970's when lasers were associated with optical fibers. A wide array of optical fibers have been developed in either glass or plastic, with solid or hollow cores, packaged in very diverse shapes to convey signals that may be visible or invisible, usually with wavelength around 1µm. These various parameters are chosen depending on the specificities of the given application.

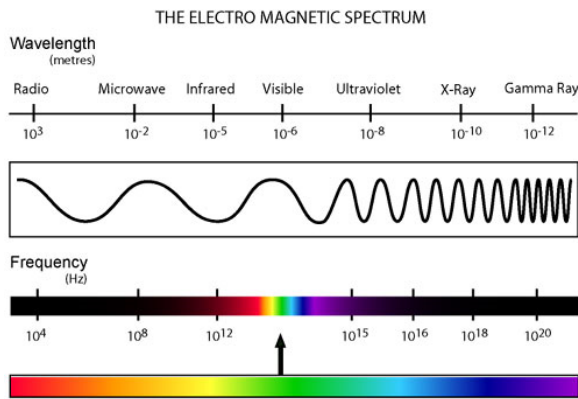


Figure 2: The electromagnetic spectrum: optical fibers convey visible and closed infrared light

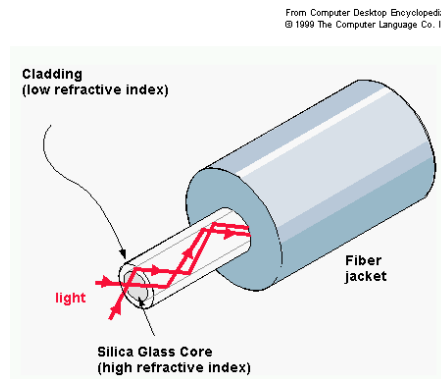
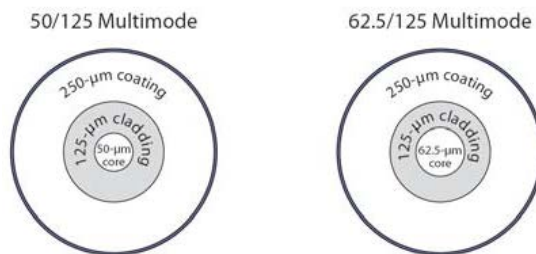


Figure 3: Structure of a silica optical fiber

To ensure guiding, the optical fiber is made of a cladding and a core, generally composed of the same material. Included impurities called dopants (such as Ge, F...) modify the refractive indexes. When the cladding has a lower refractive index, light is kept in the core by total internal reflection *Figure 3*.

Depending on the refractive index difference, on the size of the core and the working wavelength, many or only one propagation modes (paths in a first approximation) are supported inside the fiber, either called multi-mode fibers (MMF) or single-mode fibers (SMF). The basic rule of thumb is that the smaller the core diameter, the higher the fiber's bandwidth and the lower the attenuation (loss in dB per kilometer).

- Multi-mode fibers generally have a larger core diameter, in the order of 50µm or 62.5 µm, can handle high power but propagation losses are higher. Propagation losses may be 2.5dB/km (50/125) and 3.5 dB/km (62.5/125) if used at 850nm. Propagation losses may be 0.8dB/km (50/125) and 1.4 dB/km (62.5/125) if used at 1300-1310nm





- The most common type of single-mode fiber is called G.652, a code from the ITU-T (International Telecommunication Union). It is designed for use in the near infrared. It has a core diameter in the order of  $10\mu\text{m}$ , a refractive index difference in the order of a few  $10^{-3}$ ; propagation losses may be as low as  $0.2\text{dB/km}$  if used at  $1550\text{nm}$ .

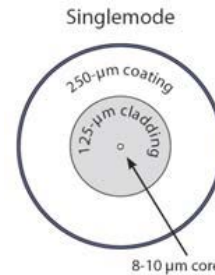


Figure 4 : Description of MM fiber and SM fiber

### 2.1.1 Related specificities of optical fiber sensors

From these characteristics, a number of specificities regarding fiber optic sensors (or OFS) can be stated:

- Since glass exhibits a very high melting point, OFS may be applied with very high temperature settings. These sensors also resist very high pressures, even in the presence of ionizing radiation. However, the protective envelope (fiber jacket) depicted in Figure 3, which proves critical to the effective mechanical resistance of silica, must be chosen on the basis of actual use conditions: standard acrylate does not withstand high temperature..
- Dimensions are very small (millimeter scale), OFS are attractive for integration into other structures ("smart structures"). A disadvantage of this specificity is optical fibers are quite fragile and need additional protection to perform reliably in field set-up's.
- The signal can propagate over several kilometers without practically any distortion. This characteristic becomes essential when remotely interrogating sensors placed inside inaccessible zones, such as radioactive wastes storage cells, which enables the upgrade of the optoelectronics during long exploitation periods and reduce the specification for very-long lasting monitoring system.
- Sensor signal acquisition speeds are solely limited by the electronic sensor interrogation system.

However, given that the useful signal is propagating over the  $50\text{-}\mu\text{m}$  ( $0.05\text{-mm}$ ) central axes of the typical multimode optical fiber, the connections between fiber segments offer sensitive points that simple dust is able to degrade; this aspect necessitates extreme care during any handling. With this consideration in mind, the majority of connections are routed far from construction site conditions.

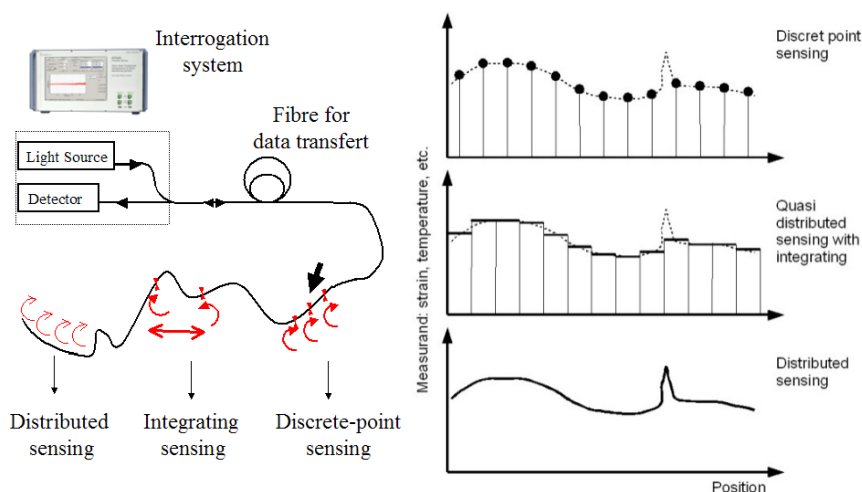


Figure 5: Diagram of a fibre-optic measurement system: An acquisition device is connected to an optical fibre containing sensors used to convey information. The sensors are local (red arrows), long-based (where the sensor corresponds to the distance between arrows), or distributed (where the fibre itself becomes a sensor)

A large variety of OFS have been successfully commercialized in the past three decades essentially based on Bragg-gratings and Fabry-Perot cavities (FP), providing one or several, localized measurements. These technologies require a specific, localized treatment of the fibre, for example localized surface grating, to create a localized, sensitive element susceptible to produce a measurable signal. These OFS technologies remain limited in their applications by the pre-defined and “point-like” nature of data they can provide. For civil engineering, a large number of such “point-like” OFS need to be multiplexed to instrument real decametric structures. A wide variety of multiplexing schemes have been developed to enable simultaneous measurement of several tens of sensors. However, even if a thousand of sensors are available, the choice of their locations may be highly sensitive, and is an intensive research topic.

In comparison, distributed sensing provides a more versatile and powerful monitoring tool as it requires much less *a priori* knowledge of the structure behaviour. The term *distributed sensor* designates the case in which the optical fibre itself becomes a sensor. It is thus no longer necessary to implement anticipated sensor positions since measurements are being performed all along the optical fibre connected to the reading device

## 2.2 Radiation, H2 and pH sensors based on FBG technology (University of Mons)

### 2.2.1 Introduction

In its simplest form, an optical fiber consists of two coaxial cylinders of different materials (core of refractive index  $n_{co}$  and cladding of refractive index  $n_{cl}$ ) and a protection (jacket generally made in polymer material) as depicted in Figure 6. Figure 6 shows a Geometrical structure of a singlemode optical fiber whose typical For silica-based fibers, the core and the cladding are made of doped silica whereas for polymer optical fibers the core and cladding are made of polymer materials. Typical dimensions for silica-based fibers are core diameters in the range 4  $\mu\text{m}$  to 62.5  $\mu\text{m}$ , cladding diameter of 125  $\mu\text{m}$  and a jacket diameter of 250  $\mu\text{m}$ . On the other hand, polymer optical fibers are bigger with typical dimensions of 980  $\mu\text{m}$  for the core diameter and 1 000  $\mu\text{m}$  for the cladding diameter.

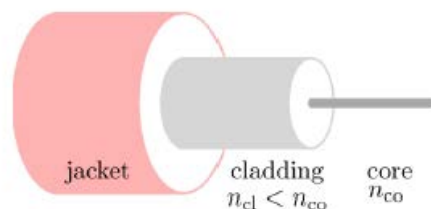


Figure 6: Geometrical structure of a singlemode optical fiber

Because of the abrupt index change at the core-cladding interface, this fiber is referred to as step-index fiber and the light is trapped inside the core by the total internal reflection mechanism.

A FBG is achieved by creating a z-periodic modulation of the refractive index of the fiber core, which generates a distributed reflector characterized by its period \_\_\_\_\_ and modulation depth

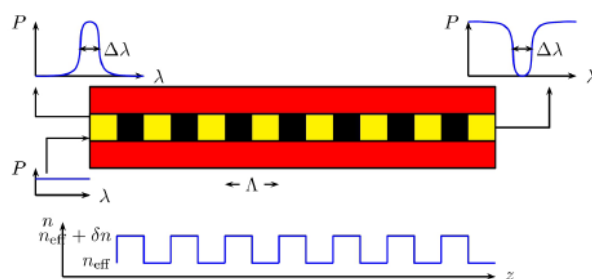


Figure 7: Basic principle of uniform fiber Bragg grating.

## 2.2.2 State of Art ((SOA) on Hydrogen and pH sensor based on based on FBG technology

### 2.2.2.1 State of art dedicated to optical Hydrogen sensor

Optical hydrogen sensors are based on two fundamental parameters: refractive index changes and axial strain. As hydrogen has no direct reaction with optical fibers, it is necessary to introduce a coating that will cause one of the desired changes and to consider changes to the fiber or FBG in order to enable it to accurately change the spectral response based on changes in the coating.

The vast majority of coatings used are based on palladium [7][8][9] or an alloy of palladium such as silver [10][11][12][13][14][15][16][17] nickel [9][18][19] and chromium [7]. However, platinum alloys are also in use which pair it with tungsten oxide [20][21][22] and silicon oxide [23] Finally, there are examples of using sol gels based on tungsten oxide [24] and palladium with titanium nanotubes [25].

Within the domain of optical sensing, the majority of hydrogen sensors are based on Bragg gratings. These sensors can be augmented by modifying the structure, microstructuring the fiber in post-production for instance has been shown to benefit the sensitivity of the fiber to strain by increasing the surface area of the applied coating [9][11][15]. Another option is side polishing the optical fiber prior to coating application [12] While the fiber itself can be physically modified, fibers can also be doped with different gases. A common dopant for hydrogen detection is hydrogen itself, yielding a significant improvement in sensitivity. However, there is a question as to whether hydrogen loading is the most advantageous [18]. Table 2 compares the six hydrogen sensors presented in this literature survey

Table 2 : Comparison of hydrogen sensors

	A	B	C	D	E
Sensor	4 mm chirped FBG	10 mm FBG	FBG	LPBG/FB	10 mm SMF
Coating	Pd-Ag	Pd-Ag	Pd/Ni	Pt-WO <sub>3</sub>	Pd/Au
Fiber	SMF-28	Double Spiral Machined	Etched to core	Hydrogen loaded	SMF-MMF coupled
Sensitivity	65 pm per % H <sub>2</sub>	52.5 pm per % H <sub>2</sub>	38 pm per % H <sub>2</sub>	1.98 pm per % H <sub>2</sub>	0.01 % per % H <sub>2</sub>
Threshold	0.014 %	0.2 %	0.5 %	0.9 % to 1.5 %	?
Resp. Time	5 s	Above typical	5 min to 6 min	Circa 1 s	24 s
Lifespan	Sub-Typical	?	Sub-Typical	Typical	?

Having described current state of the art techniques for FBG hydrogen sensors and compared the technical specifications of 4 principal methods, we now conclude by drawing conclusions on the best sensors for use in our given application and the potential for future research.

In terms of sensitivity, D has the highest overall sensitivity per percent H<sub>2</sub> concentration by far, especially given the fact that this figure is for negatively impacting air humidity levels. Indeed, overall this paper presents relatively stable wavelength changes regardless of humidity – between 1:5 and 2nm per percent H<sub>2</sub> for both dry and wet air. Temperature changes are similarly of small significance in the 50 °C to 25 °C range. The lifespan of the sensor is also good, which is extremely important for medium term isolated measurements (10s of years) and the fast response time is extremely important for such a critical indicator in a heavily sealed environment.

However, while all sensors are capable of measuring up to the 4% concentration point (the danger level for spontaneous combustion), each sensor has a different lower detection threshold. The lower detection threshold is important given the low levels expected and the importance of providing advance warning of a hydrogen build up. For this, sensor A has the lowest threshold and a very rapid response time, at the cost of lifespan and sensitivity.

As this has several unsuitable qualities, the best option may well be sensor B, which demonstrates a detection threshold of 1/4th sensor D. This is interesting given that the fiber preparation could be applied to other sensors without affecting the fundamental operation of the existing sensor. Indeed, many of the failings of sensor B could be attributed to the coating type and the sensing element with the exception of the detection threshold; where a standard FBG is expected to have a much higher threshold [16]. This is in line with expectation per the increase in coating surface area. It is however worth noting that no mention of lifespan is made in this paper and that tests should be conducted on lifespan changes when using this technique if it were to be considered for implementation.

To conclude, sensor D demonstrates many of the qualities required for our specific application; a high sensitivity, fast response and a higher lifespan than sensors with other coatings. The lower detection threshold could however be better, perhaps by incorporating micromachining per the design of sensor B. In the future it may be of value to consider testing this design and incorporating the normal sensor and coating of sensor D.

#### 2.2.2.2 Hydrogen sensor developed by UMONS

##### Hydrogen sensor composition

Uniform FBGs were inscribed into standard singlemode fiber by means of a frequency-doubled Argon-ion laser emitting at 244 nm. Prior to the UV exposure, to increase its photosensitivity, the optical fiber was hydrogen-loaded at 70 °C and 200 atm during 48 h. After the inscription, the gratings were annealed at 100°C during 24 h in order to stabilize their properties. Long period Bragg gratings were used for their radiative properties since they are transmissive gratings that couple light from the fiber core to the cladding.

To obtain the sensitive layer, nano-sized tungsten oxide powder was prepared using the sol-gel method. Aqueous sol-gel of tungstic acid (H<sub>2</sub>WO<sub>4</sub>) was obtained from Na<sub>2</sub>WO<sub>4</sub> with protonated cation-exchange resin. In a first stage, a gel consisting of WO<sub>3</sub> ·H<sub>2</sub>O was formed. The gel was washed, centrifuged several times with demineralized water and dried in air at 60 °C for 6 h. Appropriate amounts of hexachloroplatinic acid (H<sub>2</sub>PtCl<sub>6</sub>) solution were added to the obtained powder. The mixture was finally

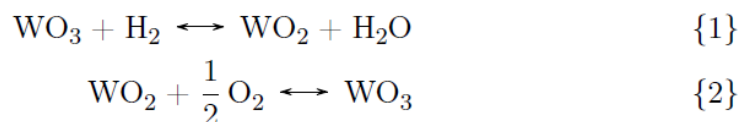


annealed at 500 C for 1 h in order to obtain WO<sub>3</sub> doped with Pt on its surface. At the end of the process, the active layer consists of WO<sub>3</sub> nano-lamellae (cubes of about 1 μm by 1 μm by 50 nm) with Pt dispersed on their surface.

Every grating was written in the middle of a 5 cm long stripped region of the optical fiber. The sensitive layer was finally dispersed in a solvent in order to deposit a uniform layer of the sensitive material (several microns) on the stripped optical fiber using the dip-coating technique, ensuring in any case the same experimental conditions. The molar ratio Pt/W was about 1/14.

Let us also add that the used layer does not react with other pollutants such as methane or carbon monoxide.

In the presence of hydrogen in air, the following chemical reactions occur in the sensitive layer:



The oxidation of H<sub>2</sub> molecules by O<sub>2</sub> molecules is an exothermic reaction that elevates the temperature around the FBG. H<sub>2</sub> sensing is therefore based on the monitoring of the Bragg wavelength shift induced by a temperature change. The activation energy of this reaction is equal to 0.15 eV.

#### Experimental set-up

The set-up used to test the H<sub>2</sub> sensors in different air environments of various relative humidity levels is depicted in figure 17. It is composed of two gas bottles, one of pure H<sub>2</sub> and the other one of dry air. A bubbler filled with distilled water is used to modify the relative humidity level of air between 0 and 90 %. Three mass flow controllers provide a mixture of air and hydrogen with variable H<sub>2</sub> concentrations from 0 to 4% (the accuracy on the determination of the H<sub>2</sub> concentration being equal to 1 %). The gas chamber is made of a 20 cm long and 1.5 cm wide glass cylinder with an inlet and an outlet to allow flowing in an out of the gas mixtures. Temperature and gas flow is continuously monitored. The amplitude spectrum of the tested gratings is measured by means of an ASE source covering the C+L bands (1 520nm to 1 620 nm) and an optical spectrum analyzer (OSA) with an accuracy of 15 pm

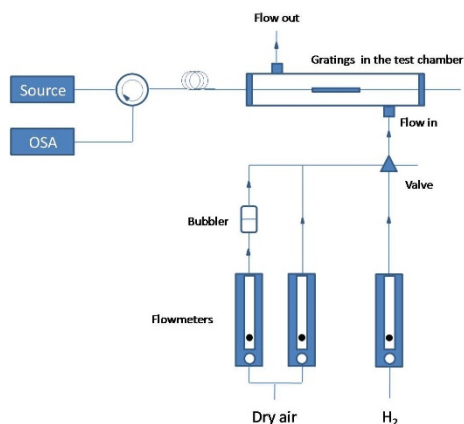


Figure 8: Experimental setup used to test FBGs response under H<sub>2</sub>.



Figure 9: Picture of the h<sub>2</sub> test bench.

## Results

Due to the need of activation energy (0.15 eV) to initiate the exothermic reaction, there exists a minimum of H<sub>2</sub> concentration below which the reaction will not start. In other words, there exists a threshold value in terms of H<sub>2</sub> concentration below which the sensor does not react. In practice, this threshold value can be decreased thanks to an external energy contribution. This could be done for instance by a local heating of the sensitive layer. One efficient way to do this is to profit from the light energy transported by the optical fiber. Indeed, at 1 500nm, the photon energy is about 0.7 eV and consequently, light that would be coupled from the core of the optical fiber towards the sensitive layer could favor the reaction for lower H<sub>2</sub> concentrations. This coupling mechanism is possible since the refractive index of the sensitive layer is slightly higher than that of pure silica and to achieve this, we have designed the FBGs to obtain a light coupling to the cladding and consequently to the sensitive layer

Figure 10: presents the results obtained on the transmitted spectrum of the 4 cm long FBG subjected to different H<sub>2</sub> concentrations in dry air at ambient temperature. A shift of the Bragg wavelength to the right appears due to the exothermic reaction that occurs between H<sub>2</sub> molecules and O<sub>2</sub> molecules inside the sensitive layer. For a 1% concentration of H<sub>2</sub> in dry air, the measured wavelength shift is equal to 2 nm, which is very easy to detect with a low cost interrogation system. This is equivalent to a local temperature increase of nearly 200°C.

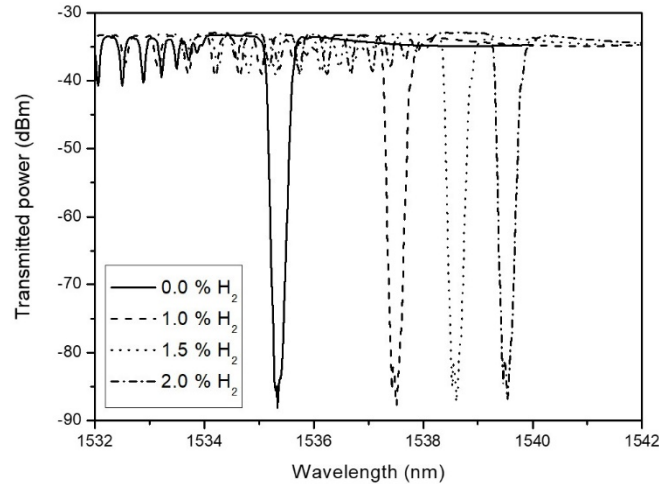


Figure 10: Transmitted spectrum of a 4 cm long FBG in response to different H<sub>2</sub> concentrations in dry air at ambient temperature

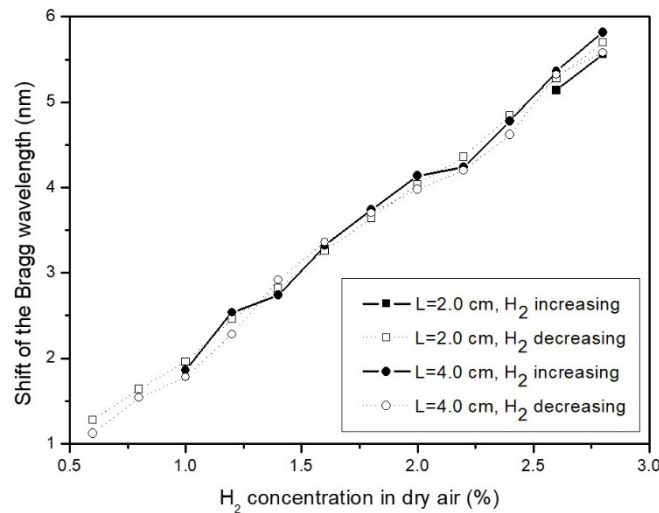


Figure 11: Shift of the Bragg wavelength as function of the H<sub>2</sub> concentration in dry air at ambient temperature for different physical lengths of the gratings

Figure 11 presents the wavelength shifts measured for two tested gratings as a function of H<sub>2</sub> concentration. The plain curves were obtained for increasing H<sub>2</sub> concentrations starting from 0% and thus revealed the threshold value. The dotted curves were obtained for decreasing H<sub>2</sub> concentrations starting from 3%. It can be seen from these last curves that the sensors are able to detect concentrations below the threshold value after it has been reached. This characteristic lasts only 2 to 3 hours and can thus be qualified as short term memory effect. Consequently, the plain curves are the only ones that represent the sensors characteristics in real-life applications

To properly determine the response time of the sensor, a valve was placed in front of the test cell so that its commutation ensures the direct contact of the sensor with the gas mixture. The OSA was set in continuous sweeping. The time between the valve commutation and the detection of the wavelength shift by the OSA thus reflected the response time of the sensor. It was computed of the order of 1 second for all the gratings when H<sub>2</sub> concentrations were above the threshold

The selectivity of the sensitive layer was also tested by immersing it into other gas such as carbon oxide, methane and pure nitrogen. No answer was obtained, demonstrating that our sensor is specific to the detection of hydrogen

in air.

The H<sub>2</sub> FBG sensors were also tested in wet air environments. The obtained results revealed that the detection threshold of H<sub>2</sub> concentration increases when the relative humidity level increases. For the 4 cm long FBG, it increased from 1.0% to 1.5% when the relative humidity level was changed from 0% to 90 %. We attribute this increase to the presence of H<sub>2</sub>O molecules that tend to inhibit the reaction. The sensitivity to H<sub>2</sub> concentrations did not change in wet air in comparison to that obtained in dry air.

Low temperature environments also led to an increase of the threshold value. At -30°C, the detection threshold reached 1.8% for the 4 cm long FBG. This value is still well below the 4% explosion limit and it can be accepted in our applications.

### Decrease of the threshold

As shown previously, when the sensitive layer is in contact with a gas mixture of air and hydrogen, the oxidation of H<sub>2</sub> molecules by O<sub>2</sub> molecules contained in air occurs on its surface. This reaction is exothermic so that the temperature locally increases around the gratings. H<sub>2</sub> sensing is therefore based on the monitoring of the resonance wavelength shift induced by the temperature change. To properly operate, this reaction requires an activation energy equal to 0.15 eV. This leads to a minimum detectable H<sub>2</sub> concentration called detection threshold that was equal to 3% in dry air for a 1 cm uniform FBG.

This threshold value was decreased to 1% in dry air with strongly reflective uniform FBGs (4 cm long gratings). However, in that case, the FBGs are so strong that the accurate measurement of their Bragg wavelength is difficult. Moreover, a drastic increase of the threshold was obtained in wet air and for temperatures below 0°C, which strongly limits the use of uniform FBGs for H<sub>2</sub> sensing.

In order to decrease the threshold sensitivity, the active layer needs to be heated and this has been realized by adding a long period fiber grating (LPBG) superposed to the FBG covered by the sensitive layer as depicted in figure 20. In that way, light energy is coupled by the LPBG into the cladding and heats the sensitive layer.

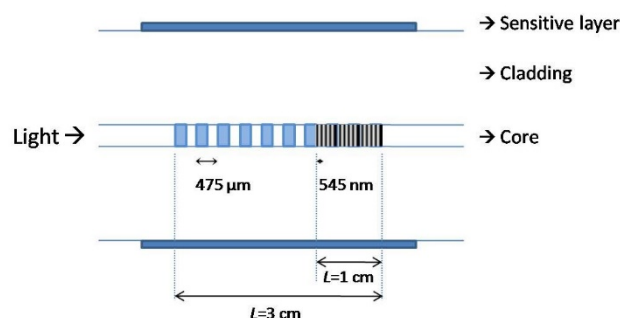


Figure 12: Uniform FBG superimposed in a LPBG for H<sub>2</sub> detection.

Both kinds of gratings were designed to minimize the detection threshold. The periodicity of the LPBG was chosen so as to obtain a strong resonance band (light coupled to the cladding) inside the spectral range of the optical source. A periodicity of 475 μm allowed us to obtain such a feature. A 1 cm long 545nm period uniform FBG was then superimposed on the 3 cm long LPBG so as to obtain a point sensor.



As shown in figure 20, it was written at the extremity of the LPFG to take a maximum profit of the light coupling provided by the LPBG.

The sensor behavior was then tested in wet air environments and at various temperatures. Figure 21 presents the Bragg wavelength shift of a hybrid sensor due to the H<sub>2</sub> concentration in different wet air environments. detection threshold increases as the relative humidity level increases. In 90% wet air, the threshold has been measured equal to 0.9% H<sub>2</sub> concentration. This is a real improvement in comparison to a single 1 cm cm long uniform FBG sensor for which the threshold value has been measured higher than 3% in 90% wet air

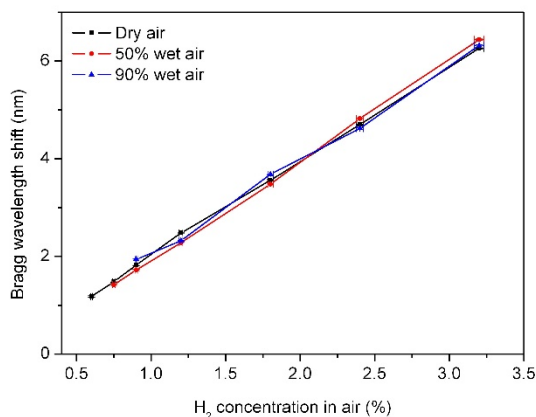


Figure 13: Bragg wavelength shift as a function of the H<sub>2</sub> concentration in wet air for a hybrid sensor.

Finally, figure 22 confirms that a surrounding temperature decrease limits the sensor performances since more energy is required to initiate the exothermic reaction for a given H<sub>2</sub> concentration. However, while a single FBG is not sensitive to H<sub>2</sub> concentrations up to 4% at -5 C, the hybrid configuration presents a detection threshold equal to 1.5 %.

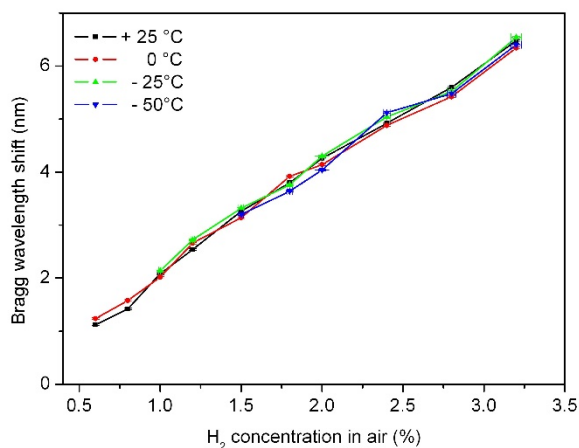


Figure 14: Bragg wavelength shift as a function of the H<sub>2</sub> concentration at different temperatures.

### Summary

Superimposed hybrid fiber gratings are coated by a catalytic sensitive layer that heats the gratings in the presence of hydrogen in air. In this hybrid configuration, the LPBG provided a light energy coupling to the sensitive layer to decrease the H<sub>2</sub> detection threshold while the FBG was used to track the temperature

increase. Very good sensing performances have been reported: fast response, high sensitivity, reversibility, frequency multiplexing capability and H<sub>2</sub> concentrations detection well below the explosion limit of 4 %, whatever the relative humidity level and for temperatures down to –50 °C. This sensor should now be tested under radiation to estimate its long term behavior and degradation mechanisms that could affect the sensitive layer

### 2.2.2.3 State of art about optical pH Sensors

While pH detectors in optical fiber are the subject of many recent publications, it is distinctly more difficult to locate publications that treat the extreme alkali regions of the pH scale using optical sensors. In order to give an in depth review of the state of the art in pH detection, this section will first treat a variety of optical pH sensors from recent publications and then continue by focusing on the specific pH region in question for our application.

Optical pH sensors rely upon the same approaches to sensing as those for hydrogen detection, that is to say that they rely upon coatings applied to the fiber that either swell or modify their own refractive index and then go on to affect the sensor through means such as cladding mode intensity modifications.

However, while a single parameter is present for hydrogen sensing, pH sensing is more complex as a range of levels conventionally require a number of different indicators that react to levels from extreme acidic through to extreme basic (also known as extreme alkali).

In general, coatings can be divided into polymers [28] polyelectrolytes [29][30] hydrogels [31][32][33] sol gels [34][35] nanoparticles [36] and fluorescent materials [37][38][39] Sensors can be based upon Bragg gratings [28][29][30][31][32][33] or simple intensity modifications [34][35][36][37][38][39] In contrast to hydrogen sensors, there is only a single case of non-coating modification in this bibliography [31] and this is difficult to analyze given the lack of temperature compensation present in other works. Below, notable examples representing distinct progressions are presented.

Table 3 compares the six pH sensors presented in this literature survey. Existing optical sensors demonstrate three distinct approaches to pH measurement; FBGs, optical intensity measurements and fluorescence intensity monitoring. While FBGs appear mostly aimed at the neutral pH band, other techniques appear more focused in the region of interest within the extreme basic region. One of the best sensors to date is sensor D, which, while very different to the FBG sensing intended, demonstrates the same objective and presents very positive characteristics in terms of sensor duration and repeatability.

However, it is unknown whether any of the technology could be adapted for use with FBGs as fluorescence itself may not induce the right region of refractive index change for monitoring using FBGs in silica fiber.

The best pure optical solution appropriate to the pH range appears to be sensor C, where the correct pH range is present and the sensor is potentially reusable. However, the relatively low intensity change and the questionable conversion for use with FBGs means that making specific recommendations from this example is difficult. While both A and B utilize FBG coated sensors, sensor A fails to be more than a single use sensor for the correct pH region.

and sensor B is not only confined to the neutral pH region but also has a very narrow range and a low sensitivity relative to the length of the FBG when considering sensor A.

However, one promising avenue of research is presented in the form of sensor E. While many characteristics are unknown and the pH range is far from suitable, the sensitivity is exceptionally good,



albeit one that could well be much worse above and below pH 5 as with many other sensors. Given that the optical is not remarkable in itself, the reason behind the sensitivity is either the restrictive nature of the testing or the polymer thin film. It could be interesting to further investigate polymer thin films and identify whether a similar approach could be explored for our pH range and whether this approach demonstrates a wideband response to pH or not

Table 3 : Comparison of pH sensors

	A	B	C	D	E
Sensing Method	FBG	FBG	Optical fiber	Fluorescence	D-shaped fiber
Sensing Material	Poly-electrolyte multi-layer	Hydrogel coating	Sol-gel coating	Polymer Tablet	Polymer thin film
Sensor Dimensions	4.2 $\mu$ m diameter 3 mm length	40 $\mu$ m diameter 10 mm length	60 $\mu$ m diameter 40 mm length	?	17 mm
pH Range	1-14	5-7	4.5-13	10-13	4-5
Sensitivity	0.25 nm (10-12 range) per pH	0.114 nm per pH	0.25 % intensity per pH	8.3 % intensity per pH	69 nm per pH
Response Time	?	12 min	5 min	50 min	?
Lifespan	Single use for 2 < pH < 10	?	?	Min. 20 months	?

### 2.2.3 pH sensor developed by UMONS

#### Tilted fiber Bragg gratings

A fiber Bragg grating acts as a wavelength selective filter around the so-called Bragg wavelength  $\lambda_B$  and the typical period  $\Lambda$  is usually around 500 nm. For a normal grating, the light stays inside the fiber core and can thus not interact with the surrounding medium. Tilted fiber Bragg gratings (TFBGs) present a refractive index modulation angled by a few degrees ( $\theta$ ) relative to the perpendicular to the optical fiber axis as shown in Figure 12.

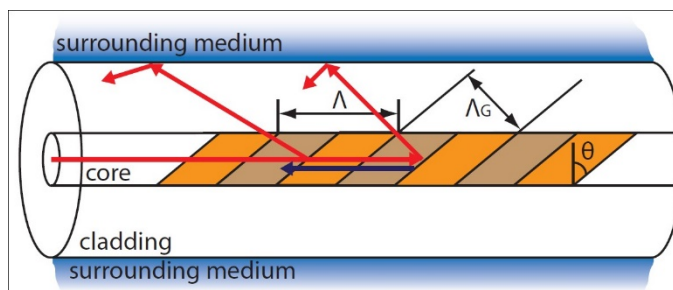


Figure 15: Scheme of a tilted fiber Bragg grating and its mode couplings.

They couple light between the core and the cladding according to the relation (4):

$$\lambda_{\text{cld},i} = (n_{\text{eff,core}} + n_{\text{eff,cld},i}) \frac{\Lambda}{\cos \theta} \quad (4)$$

Where  $n_{\text{eff,core}}$  and  $n_{\text{eff,cld},i}$  are the effective indices of the core mode and the  $i$ th cladding mode, respectively

As a result, they present a comb-like transmission amplitude spectrum comprising several tens of resonances, each one characterized by its own sensitivity to the surrounding refractive index.

The important point is that the position and the amplitude of these peaks depend on the refractive index of the surrounding medium. When immersed

in a medium with a refractive index next which matches the effective refractive index of some cladding modes (e.g. when  $n_{\text{cld},i}$  next), these modes become weakly guided and the narrow resonance peaks are replaced by a

smooth radiated continuum. As the refractive index of the cladding modes  $n_{\text{cld},i}$  is bigger when the wavelength increases, the peaks corresponding to shorter wavelengths disappear first when the refractive index next increases.

This means that TFBGs naturally yield refractometers accurate to 10<sup>-4</sup> RIU (refractive index unit).

Covering TFBGs with a dedicated coating that changes its refractive index when in contact with target chemical species leads to building a specific chemical sensor.

Here, we present a sensor based on relative index changes monitored by a TFBG covered with a mineral coating, a porous silica sol-gel encapsulating an indicator. Silica sol-gel is chosen because its refractive index is close to that of the silica fiber, enhancing in turn the response. Moreover, its chemical resistance and its good adhesion on silica fibers is an advantage. Bromophenol blue was used due to its convenient pKa (transition pH range 3.0 to 4.6). The alkaline and acidic forms are given in figure 30.

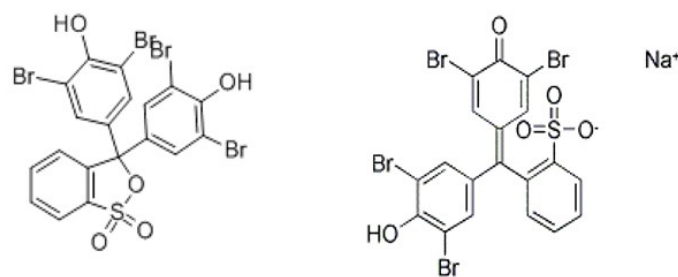


Figure 16: Bromophenol: left acidic form, right alkaline form.

### Sensor fabrication

Experiments were carried out on TFBGs classically manufactured into hydrogen loaded singlemode optical fiber by means of a 1 095nm uniform phase mask and a frequency-doubled Argon-ion laser emitting at 244 nm. The phase mask was tilted in the plane perpendicular to the incident beam. An external tilt angle of 6° was chosen. The protection coating was mechanically removed before inscription. After that, and before coating, gratings were annealed at 80°C during 12 hours in air to remove the hydrogen and stabilize their physical properties. TFBGs with maximum peak-to-peak amplitude of 25 dB around 1 562nm are obtained in air. The Bragg peak amplitude is about 4 dB.

The deposition of the coating induces a reduction of the peak amplitudes of

the cladding modes.

The sensitive sol-gel coating was obtained by incorporation of the pH indicator, here bromophenol blue, in an pure alcoholic solution (15ml) containing TEOS (TetraEthoxyOrthoSilicate) as precursor (15 ml), distilled water (3 ml), PEG 6000 (PolyEthyleneGlycol) (1 mg) and HCl as catalyst (2m, 0.25 ml).

The solution was heated at 60 C (reflux) for 1 hour and aged for 1 week before use. The sensitive layer was then deposited on the fiber by dip coating in one step and annealed at 80 C for 1 hour, yielding a 5  $\mu\text{m}$  thick transparent yellowish layer.

### Experimental setup

Amplitude transmission spectra of the TFBGs are measured using a broadband optical source (Amonics) and an optical spectrum analyzer AQ6317C from Ando as depicted in Figure 14.

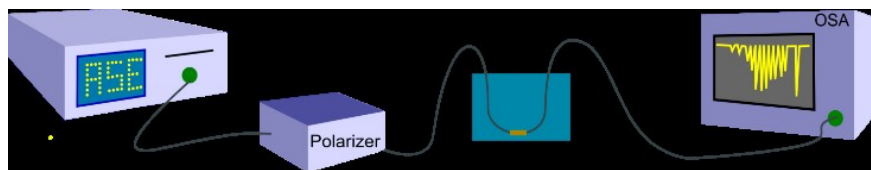


Figure 17: Experimental setup used to measure the transmitted amplitude spectra of the TFBG.

The fibers were immersed in a 1m NaCl solution and the pH was adjusted by adding 1m HCl and NaOH solution drops in a well stirred beaker. NaCl is introduced to ensure the refractive index of the solution remains constant during the injections. This was controlled with a refractometer (Reichert -accuracy 10<sup>-4</sup> RIU). The pH was controlled with a classical glass electrode pHmeter (Metrohm - accuracy 0.02 pH unit). The scanning time for 10pm resolution in the range 1 520nm to 1 590nm is about 40 s

### Results

Figure 32 displays the TFBG amplitude spectra for various pH values. It can be observed that the resonance modes are drastically affected by the pH variations.

The peak-to-peak amplitude decreases as pH increases while the wavelengths of the resonance peaks shift to longer wavelengths. As expected the Bragg peak remains unchanged and can be used as an internal reference for temperature variations.

From analysis of these peaks, the pH can be computed as shown in Figure 15 that shows the amplitude evolution versus pH for the peak centered around 1 562 nm.

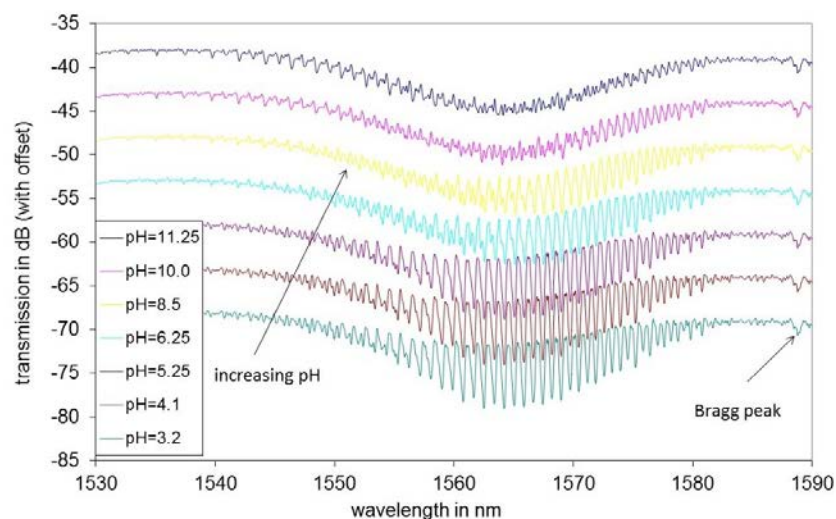


Figure 18: Transmission spectrum of the TFBG at different pH values.

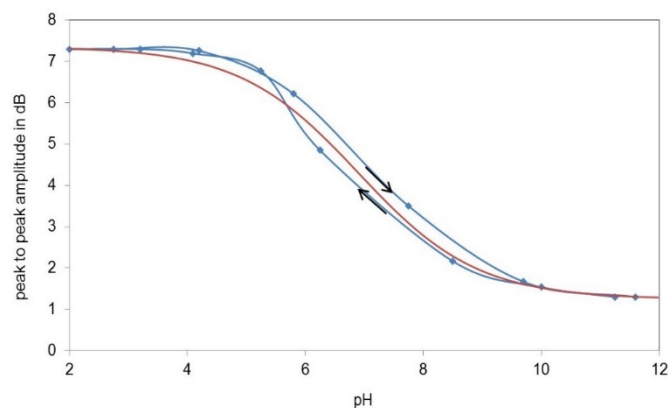


Figure 19: Peak-to-peak amplitude of the transmission spectrum at 1562 nm at different pH values. Experimental points and sigmoidal fitting

As could be expected, the response of the sensor presents a reversible sigmoidal shape although a small hysteresis (0.3 pH unit near 7) is observed. The hysteresis could be reduced by increasing the porosity of the film. We see that the response is almost linear in the range 4.5 to 9.5 centered around  $\text{pH} = 7$ . The slope of the variation of the transmission as a function of pH is  $-1.36 \text{ dB/pH}$  unit.

The wavelength shift of the peaks could also be exploited but for high pH values the amplitude of the peaks decreases and it is more difficult to accurately determine the position of the peaks.

When following only one given peak, the scan can be refreshed each second allowing to measure the response time. The response time is evaluated to about 10 s when going from pH 3 to pH 10 or vice-versa as shown in Figure 17.

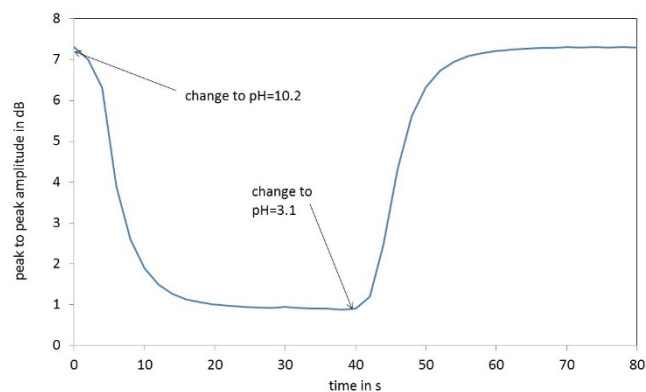


Figure 20: Response to pH change: Peak to peak amplitude around 1562 nm versus time for a change from  $\text{pH} = 3$  to  $\text{pH} = 10.2$  and  $\text{pH} = 10.2$  to  $\text{pH} = 3.1$ .

This sensor works correctly around a pH of 7. As for the hydrogen sensor, it should now be tested under radiation to estimate its long-term behaviour and degradation mechanisms that could affect the sensitive layer. As the target value of the pH to be monitored in the repository is not yet precisely known (one speaks about 11-13), we have not plan irradiation tests now.

Indeed the sensitive layer will be strongly dependent on the central pH to be measured and these radiation tests with bromophenol will therefore not be representative enough

## 2.2.4 Concept description and methodology

Having established precise application contexts for our sensors, the necessary steps to progress towards demonstrator grade testing are the following:

**ILW Hydrogen Sensor:** Our existing development of a Pt/WO<sub>3</sub> layer on silica fiber is arguably one of the strongest technologies known for this application with respect to response time, sensitivity and resolution. However, this sensor has never been exposed to any radiation and the layer itself is fragile. Recent efforts to improve layer adhesion resulted in total loss of hydrogen sensitivity. To move the sensor into a practical testing environment comprehensive radiation testing and qualitative testing on layer adhesion is needed before considering demonstrator testing.

**HLW Hydrogen Sensor** For non-ambient atmospheres, many technologies exist, however our university has not currently developed one. Within MODERN2020, a Pd-doped silica fiber sensor exists, however alternate modalities are possible. We have internally proposed a polymer fiber based palladium sensor, where the improved adhesion and increased sensitivity to pressure are considered significant advantages. Polymer fibers under consideration at 1 550nm are PMMA and CYTOP. Prior to sensor development for this application, polymer fibers need to be irradiated to assess wavelength specific losses and the effect on polymer fiber Bragg gratings (POFBGs). After this, sensor development can proceed and once a sensor of acceptable parameters is developed and tested, irradiation should be conducted on a viable sensor as with the ILW proposal.

**pH Sensor To date,** no pH sensor for corrosion within concrete has been developed or proposed based on optical fiber, with the exception of a fluorescence based sensor where the fiber is merely a conduit to a detector. For implementation, a viable concept must be presented and tested and then subjected to irradiation to observe viability.

**Humidity Sensor Humidity** sensors come in many forms, with the simplest being standard PMMA fiber. CYTOP fiber may also be susceptible due to the polycarbonate coating. Any concept for humidity based on POF needs to therefore follow the implementation set out in the HLW Hydrogen Sensor development plan.

### Test Objectives of the First Campaign

This first irradiation campaign is divided in two runs: the first test is designed to:

- Verify fibers can support low levels of radiation.
- Check fiber functionality for the Belgian test case.
- Verify the chemical layer can support low levels of radiation.
- Obtain results for POFBGs in this region in the event that the 2nd test will cause fibre destruction.

whereas the second test aims to:

- Expose fibers to doses approaching the French case.
- Understand the radiation induced trends to predict a maximum radiation level for future tests.
- Provide new academic knowledge on POFBGs in the telecoms region.



### Test Objectives of the Second Campaign

After the first campaign revealed interrogation problems and inconsistencies, a second campaign was agreed upon, with the express intention of providing high quality insight into polymer fiber radiation responsivity with a view to publication. The exact objectives of this campaign were expressed as:

- Produce two peer reviewed and published studies on PMMA and CYTOP Bragg grating radiation responsivity in the 1 550nm region.
- Examine CYTOP graded index, PMMA step index and PMMA microstructured fibers.
- Analyze the change in Bragg grating profile in each of these fibers with respect to their peak amplitude, peak wavelength and bandwidth.
- Provide specific failure cases to allow quality results even in the case of failure during any given stage of the tests.
- Establish the case for using polymer fibers as platforms for sensing within a radiative environment and specifically within the case of nuclear waste repositories.

For all tests, the following guidelines have been applied:

- Fibers are installed in an oven for temperature control, immersed into a pool and irradiated with a known and characterized source of gamma radiation.
- Interrogators are shielded 15 metres away from the pool and linked via waterproof cable to a container with the oven inside.
- Thermocouples are placed inside the container and the output logged in real time.
- UMONS interrogators were used for FBG tracking (see section 5.8).
- Fibers are irradiated using 'RITA' at SCK-CEN with specific doses attributable to given fiber placement heights.
- Test 1 (campaign 1) is designed to attain a total dose of 10 kGy.
- Test 2 is designed to attain a total dose of 100 kGy.
- Test 3 (campaign 2) is designed to attain a total dose in the region of 120 kGy for the polymer fibers.

### **Hydrogen Sensors under radiation**

While online measurements were possible for the FBGs, it was not possible to expose the sensors to hydrogen while under radiation. Analysis after the campaign has revealed that the sensitive layers were physically degraded and in some cases appeared destroyed to the naked eye. It is suspected that the problem mainly comes from a lack of adhesion of the layer and transport dislodging the layer in part or in totality. When transported but un-irradiated samples were tested for hydrogen sensitivity and all were found inoperative, our suspicions were confirmed to the point of halting radiation testing until a more robust layer can be fabricated and proven.

### **Results about radiation**

More details could be seen in the milestone 3.9

## **2.2.5 Conclusion**

Optical fiber technology is a promising technique for sensing nuclear waste disposal sites, especially for the Belgian case where the expected total dose is small. Indeed, silica-based fibers can be engineered to be either radiation insensitive or radiation sensitive depending on the application. Although hydrogen



sensors were successfully developed, radiation tests were not satisfactory. It is believed that the problem comes from a lack of adherence of the sensitive layer but no conclusion can be drawn on their radiation robustness.

pH sensors still require a lot of effort to be tested in radiation field. They should first be tailored for the pH range of 11-13, which is very challenging.

Finally, polymer optical fibers and gratings were tested as an alternative to silica-based fibers. First results show that these fibers are radiation sensitive and survive 100 kGy.



## 2.3 Design and performances of a sensing system to provide distributed radiation, H<sub>2</sub> strain and temperature measurements in geological repository environments (Andra, Xlim)

### 2.3.1 Introduction

For Andra, the main goal is Cigéo monitoring, the future French underground repository for high level and intermediate level long-lived radioactive wastes. The target monitoring parameters were detailed in [41] and in D2.2.

Optical fiber sensors (OFS) are mainly plan for temperature and mechanical evaluations. Temperature monitoring contributes to verifying the assessment basis for long-term safety, by allowing verifying whether prior predictions for the duration of the thermal period and the expected thermal peaks are consistent with in situ observation. Mechanical parameters are also required, to verify the conditions enable waste retrieval, if decided. Expected sensing range, target sensing uncertainties and measurement frequency are detailed in Table 4. To provide accurate and verified measurements, it is important to characterize all influencing parameters in the sensing chain.

This is why hydrogen and radiation also appear in the target monitoring parameters. Gamma radiation dose rate ranges from 1 to 10 Gy/h depending on the waste category. Since sensors would be partially protected by the structure (metallic liner in HLW repository cell), dose rate would be reduced by a factor 10. Over the target lifetime of 100 years, doses up to 10 MGy could be deposited on the sensors. The atmosphere is hydrogen-rich because H<sub>2</sub> emissions originate from anoxic corrosion of metallic materials. The parameters are not homogeneous around the repository cells. This is one of the reasons to focus developments on truly distributed optical fiber sensors.

Table 4. Main parameters to be monitor in the underground repository

Parameters	Typical Value/range	Uncertainty requirement	Spatial homogeneity of the parameter	Measurement frequency
<b>Temperature</b>	[20-90 °C]	±0.1 °C	20 cm	1 meas/day
<b>Displacement</b>	+ 0.5 mm/m to - 2.5 mm/m	1 µm/m	10 cm	1 meas/day
<b>Strain evolution in concrete element</b>	10 µm/m	3 µm/m	10 cm	1 meas/day
<b>Concrete Crack</b>	Threshold for openings : 200µm		10 cm	1 meas/day
<b>Gap evolution inside the cell</b>	10mm (in 100 year)	-	1 m	1 meas/day
<b>Hydrogen</b>	[0-4%] sensitivity of 500ppm [4-10%] sensitivity of 1%	100 ppm <1%	3 m (ILL waste package size) ~1.5 m (HL waste package)	1 meas/day

<b>Gamma radiation</b>	0.1-1Gy/h TIG = 10M Gy (100 years)	50mGy (?)	~1.5 m (HL waste package)	1 meas/month
------------------------	---------------------------------------	-----------	---------------------------	--------------

Sensor hardening is a major issue for the design of reliable, long-living equipment. Worst case will be considered for development, namely the vicinity of HLW repository cell. Strain and temperature distributed sensing

## 2.3.2 Distributed optical fiber technology

### 2.3.2.1 Backscattering technologies

Within MODERN2020 projet, Andra focused on “distributed optical fiber sensor”. It designates the case in which the silica-based material becomes a sensor, as sketched in Figure 18. Monitoring with a single fiber can provide information all along the structure behavior, and thus overcome limitations of traditional sensors, whose information is restricted to local effects.

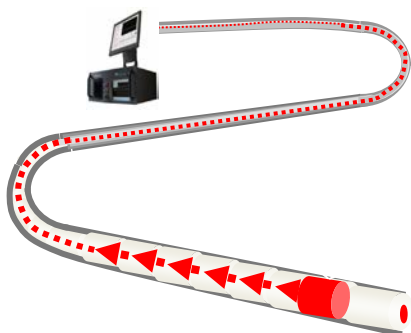


Figure 21: Sketch of a truly-distributed measuring system

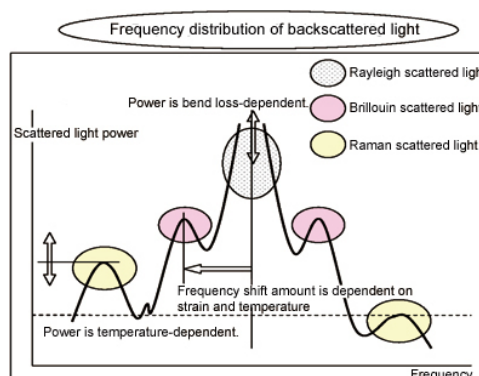


Figure 22: Spectrum of backscattered light inside an optical fibre: higher frequencies are called anti-stokes, shorter are called Stokes components

To obtain such a performance, the instruments combine (i) a sensitive phenomenon based on Brillouin, Rayleigh or Raman scatterings with (ii) a localization process, usually OTDR (Optical Time Domain Reflectometry) or OFDR (Optical Frequency Domain Reflectometry as in Luna-OBR device mentioned later) or coherent probe-pump technique (as in Neubrescope device mentioned later).

There are three main scattering processes in optical fibers. As illustrated in Figure 19, Rayleigh and Brillouin scatterings are sensitive to both strain and temperature whereas Raman scattering depends only on temperature.

Performances are summarize in Table 5. For comparison, values are orders of magnitude; performances may significantly change with the operation wavelength, the device supplier, the sensing optical fiber type, (etc...):

- Raman device performances should reach 0.1 °C uncertainty over 30 km, with a length resolution of 1m.
- Brillouin systems provide 1 °C or 20µm/m uncertainties, over 30 km, with a spatial resolution of 1m.
- Rayleigh scattering sensing devices exhibit higher performances than Brillouin based systems. Depending on the localization process, there is a trade-off to find between the

maximal sensing range and the spatial resolution. For the Luna company device called OBR, based on OFDR technique (respectively tunable-OTDR -Neubrex company device called NBS7020) measurement distance range is 70 m (resp. 20 km), and spatial resolution in the order of 1 cm (resp. 20 cm).

It is worth noticing that both Rayleigh and Brillouin instruments are using singlemode fibers (SMF) and operate at wavelength around 1.55  $\mu\text{m}$ . For distance range smaller than 20 km, most commercially-available Raman devices use multimode fibers (MMF) at around 1064 nm. It implies that the three device types cannot be paired with the same optical fiber. Raman singlemode devices exist but are less efficient on short distance (and more expensive).

Compared with Raman sensing systems, sensitivity is reduced by a factor 10 (see table below) when measuring temperature with Brillouin scattering. However, this measurement is wavelength-encoded, unlike Raman scattering based on intensity. It should be more reliable on the long term.

Table 5. Typical performances of distributed temperature and sensing systems based on Rayleigh, Brillouin and Raman scatterings in optical fibers.

Scattering	Rayleigh		Brillouin		Raman
Process	Elastic		Inelastic		Inelastic
Optical fiber type	Single-mode		Single-mode		Mainly multi-mode
Measuring principle	OFDR	TW-COTDR	BOTDR	BOTDA	R-OTDR
Access to fiber	Single end		Single end	Loop configuration	Single end
Maximal distance range	70 m	20 km	30km		30km
Best spatial resolution	10 mm	20 cm	1 m	10cm	1m
Temperature sensitivity	$C_r^R = -1.5 \text{ GHz}/^\circ\text{C}$		$C_b^B = 1 \text{ MHz}/^\circ\text{C}$		$0.1 \text{ }^\circ\text{C}$
Strain sensitivity	$C_{\epsilon}^R = -0.15 \text{ GHz}/\mu\epsilon$		$C_{\epsilon}^B = 0.05 \text{ MHz}/\mu\epsilon$		Not sensitive
Measurement Uncertainty	$0.1 \text{ }^\circ\text{C}$	$0.5 \text{ }^\circ\text{C}$	$5 \text{ }^\circ\text{C}$	$1 \text{ }^\circ\text{C}$	$0.01 \text{ }^\circ\text{C}$
Measurement duration	10 s	10 min	10 min		1 min
Optical budget	70 dB	10 dB	10 dB		10 dB

### 2.3.2.2 Cable purposes

Performances obtained with optical fibers in laboratories and is usually degraded significantly in real application.

For instance, standard fibers have acrylate as a primary coating, which is limited to 80°C temperature. For 90 °C expected on the metallic liner of HLW repository cells, polyimide coatings or metallic coatings (Al, Au, Cu) are available. Carbon coatings are also available. They are all the more attractive as they also prevent hydrogen diffusion into optical fibers.

These primary coatings are too fragile for a direct implementation into concrete structure or clay boreholes. To transfer laboratory results into real structure monitoring, optical fibers has to be inserted into strain or temperature sensing cables compatible with civil engineering conditions examples could be found [ref].

Part of the work performed within MODERN2020 project was focus on the sensing cable design and its realization: First, the choice of the primary coating, second the design and realization of the external sheath. Once realized, question was the possible strain sensing performance differences between “naked” optical fibers and jacked optical fiber (cable).

Many results has been obtained during the Modern2020 four years project, details can be fould in the dedicated milestones 3.9. In the deliverables 3.4 only the significant results is shown in the following paragraph.

### 2.3.3 Distributed Temperature sensing

This paragraph details the work performed on distributed temperature sensing and obtained results. Andra reference solution makes use of Rayleigh and Brillouin scatterings for strain sensing and Raman scattering for temperature measurements.

Indeed, Raman scattering provides better uncertainties (0.1 °C) than Brillouin scattering (1 °C) and does not require specific mechanical isolation since it is only sensitive to temperature.

Work performed on distributed temperature sensing based on Raman scattering is detailed in **Erreur ! Source du renvoi introuvable.-Erreur ! Source du renvoi introuvable.** Then a back-up solution is presented in **Erreur ! Source du renvoi introuvable.** : possibilities and limits of Rayleigh and Brillouin scattering paired with special cables, called “loose tubes”, which provide mechanical insulation, are considered.

#### 2.3.3.1 Raman technologies issues

Despite of some actions leaded at the international level (i.e. IEC and ASTM standardization committees) the dissemination of the Raman DTS technologies to the concerned industries is suffering from a lack of well-established standardization in this field. For that reason, users are often lost with the performances of Raman-DTS systems which are only based on the specifications proposed by manufacturers (as resulting of a heterogeneous – sometimes mistaken – vocabulary used for describing the characteristics of the Raman-DTS systems).

Andra has defined a set of metrological characteristics, and developed some dedicated experimental facilities and protocols for characterizing Raman-DTS devices [61]. The objective is to enable the users to perform a relevant comparison of such systems with a great confidence.

#### 2.3.3.2 Materiel and methods

To evaluate the metrological performances of our Silixa device, we collaborated with EDF and LNE (*Laboratoire National de Métrologie et d'Essais, France*) where we had access to a bench designed for optical fiber distributed temperature measurement evaluation, see [62]. It makes use of a standard commercial multimode fiber, OM-2 type, with 50 µm core and acrylate primary coating. Both the interrogator and the sensing optical fibre are placed in their own thermal enclosures. Two initiating/ending sections of the optical fiber are immersed into the thermal enclosure dedicated to the interrogator, in order to decouple them from the main part of the sensing optical fiber.

The temperatures of the two enclosures are controlled by the mean of 100 Ω platinum probes. The sensing/effective optical fiber has a length of 4 km and the two initiating/ending optical fibre sections have a length of 500 m each. Then, the whole optical fibre length is 5 km, the maximal distance range of the device. Each optical fibre section is wounded without any spool support, and just arranged on the floor of the thermal enclosure, in order to limit the mechanical constraints.

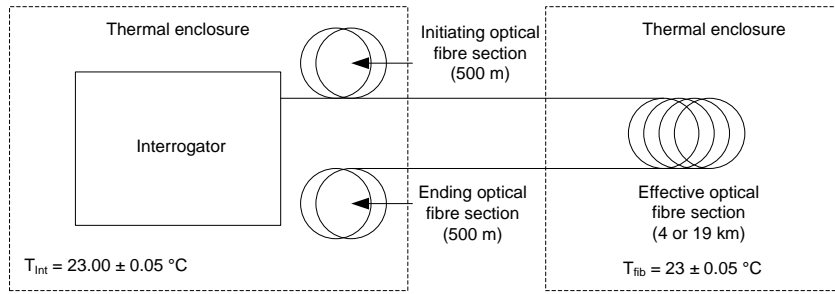


Figure 23: Schematic experimental arrangement for evaluating performances of DTS Raman interrogator

### 2.3.3.3 Raman metrological results

Figure 21 shows the raw measurement, a temperature trace, obtained with the Raman - Silixa instrument operating in single-ended configuration. The device and both initiating and ending optical fibre sections are stabilized at 23.00 °C and the main sensing optical fibre is stabilized at 23.10 °C. Measurement duration was 120 s.

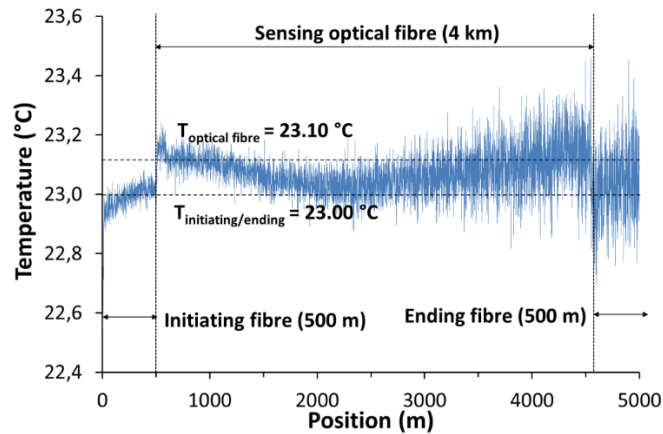


Figure 24: Temperature trace measured with the SILIXA device after calibration at 23°C.

As expected, temperature measurement uncertainty is very good, tenth of degree, and increases with the distance along the fiber. Surprisingly, the dependence is not linear.

More precisely, a mean temperature value is computed over an interval of 10 successive samples centred on a considered point along the optical fiber. The mean trueness error (MTE) is the difference between the mean temperature and the true temperature measured at the same time by a 100 ohms standard platinum resistance thermometer, positioned at the centre of the wound optical fibre coil. It was calculated every 500 m along the fiber; the experiment was repeated 4 times for four target temperatures, 3 °C, 23 °C, 40 °C and 60 °C.

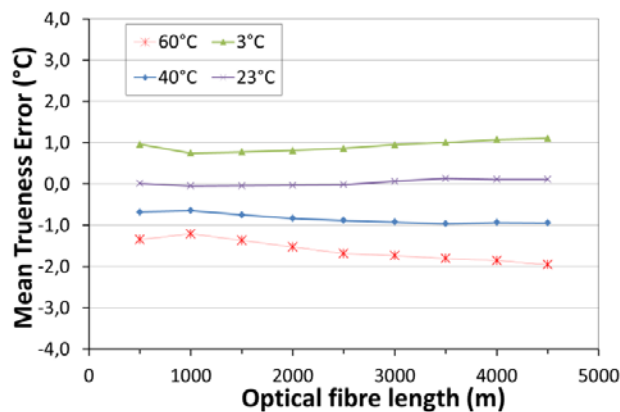


Figure 25: MTE measured with the sensing optical fiber stabilized at Four different temperatures - (23 °C, 3 °C, 40 °C and 60 °C)

Figure 22 compares the temperature returned by the Raman-DTS interrogator with the true temperature given by the SPRT, on each point of the sensing optical fibre. At 23 °C, at 500 m, the interrogator has a MTE of only 0.02 °C and -0.11 °C at 4.5 km. At 60 °C, it is -1.35 °C and -1.85 °C for the same two extreme positions. These tests confirmed that the device worked as expected with standard fibers, in laboratory conditions.

#### 2.3.3.4 Influence parameters

Based on previous work, we knew that (i) a special fiber is mandatory yet not sufficient to provide accurate temperature sensing based on Raman scattering in harsh environment (ii) double-ended scheme are promising. We had to verify these results with our own products.

We quantified the performances of the Silixa Raman sensing device (i) in single-ended versus double-ended schemes (ii) paired with a MM-Fibers (MultiMode), designed to endure high-level radioactive waste repository environment. More precisely, similarly with the developed singlemode fiber, iXBlue company designed and provided a fiber on Andra specifications.

#### 2.3.3.5 Summary of the temperature sensing elements

We evaluated the performances of distributed temperature measurement based on Raman scattering.

We had a special fiber developed by iXBlue to convey resistance to radiation and hydrogen-rich environment. We performed paired irradiated samples of such fibers with a commercial device, in single-ended and double-ended schemes.

Concerning radiation hardening, measurements done in a single-ended scheme are strongly affected by radiations: F-doped optical fiber is mandatory but not efficient enough to reduce temperature measuring errors based on Raman scattering. Main problems arise from Stokes and anti-Stokes differential attenuation and could not be solved with the different setups. A solution is to implement other Raman scattering measuring configurations, namely double-ended measurements. We have shown that double-ended measurement configuration allows obtaining a good evaluation of the temperature even for measurements done with irradiated MM fibers. However, temperature measurement quality is significantly degraded: measured temperature error reaches 5 °C. These results are consistent with recent studies. As a perspective of this work, there are new devices recently commercialized, based on other sensing architecture. Namely, since 2017, the French company VIAVI offers a DTS with two pumping

wavelength, one standard and the second placed at the corresponding Stokes wavelength. This solution might cancel the differential solution problem [67]. It should be tested in the future.

We have not performed the evaluation of coupled temperature and radiation influence because a PhD tackled this topic in the first year of MODERN2020 project, showing temperature limits and the negative influence of radiation. Hence, our results are pessimistic and we can be confident that temperature uncertainty will be smaller than 5 °C.

Perspective is to evaluate the influence of hydrogen on the irradiated carbon-coated samples.

TRL is presently estimated at 5 for distributed temperature measurement based on Raman scatterings.

We also evaluated the possibility to pair Brillouin or Rayleigh scattering with a loose tube, to get rid of strain influence and be able to provide temperature measurement only. We acquired a commercial loose tube and paid strong attention to implementation procedure. At the end, we proved that loose tube is efficient to isolate the sensing fiber from mechanical stress. It is an interesting back-up solution for temperature sensing, since temperature uncertainty actually remains similar for the three scatterings after radiation impact.

### 2.3.4 Distributed hydrogen sensing

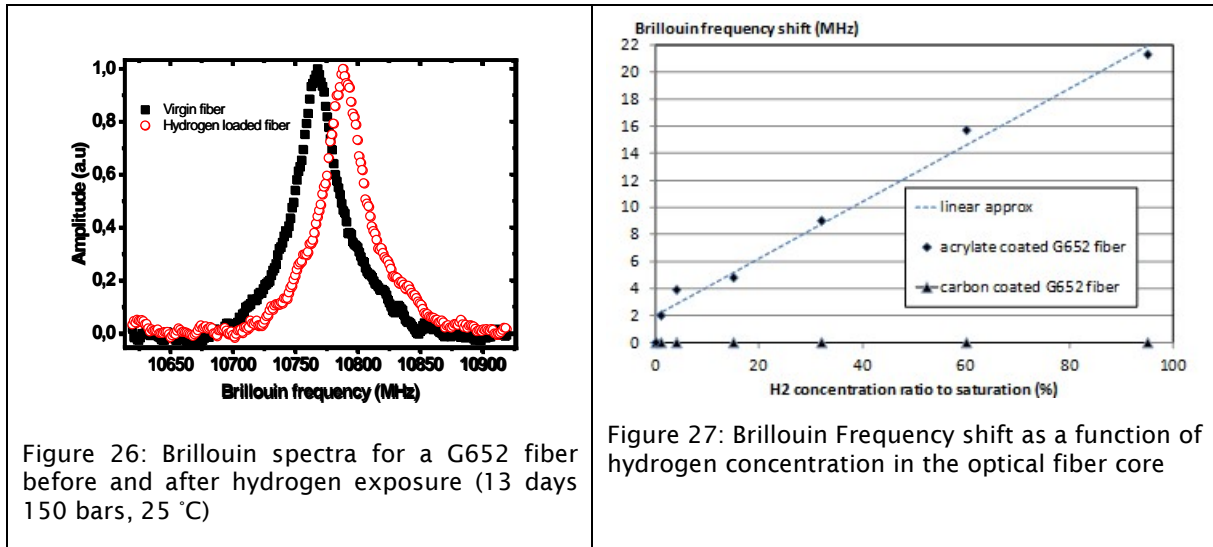
Hydrogen naturally diffuses into silica optical fiber and induces absorption bands, illustrated in Figure 26. This phenomenon is reversible: hydrogen is spread out when fibers are no longer exposed to H<sub>2</sub>. Efficient hydrogen sensing was achieved by using standard G652 optical fibers with

- i) Pd films deposited on the fiber cross-section [73],
- ii) laid around the fiber [74][75] iii) around the core [76] or
- iii) around tapered fiber [77].

In contact with H<sub>2</sub> gas, Pd forms an hydride PdH<sub>x</sub> (with x is a functions of the gas rate) leading to a variation of both the material refractive index [78] and lattice cell volume [78],[74]. However, these sensors suffer from untimely deterioration in harsh environments and poor robustness [79]. They are mainly dedicated to short-term measurements.

To develop distributed measurements, pairing the capacity of silica to absorb hydrogen with localization processes such as OTDR, provides truly distributed hydrogen sensing [80]. However, aging of optical fibers, radiations, unexpected mechanical solicitations also increase propagation losses. To obtain durable and long-term measurement, a wavelength-encoded principle, such as Brillouin scattering seems more attractive. Frequency shift of the Brillouin backscattered peak resulting from hydrogen diffusion into a standard G652 fiber tested at 1.55 μm has been demonstrated by Andra [80] (Figure 23), allowing distributed monitoring of H<sub>2</sub> concentration. At 25 °C, with an acrylate-coated fiber, the Brillouin frequency shift is almost linear with hydrogen concentrations in the silica core, with a factor of 0.21 MHz/%H<sub>2</sub>. Neubrescope device sensitivity is in the order of 1MHz; it corresponds to 5 %H<sub>2</sub>. Hence, resolution is poor in standard fibers, about 5%H<sub>2</sub>.





On the contrary, to avoid hydrogen influence fully hermetic coating has to be found like the carbon coating shown in the Figure 24 (triangle). In fact, 20MHz shift means 20°C or 400  $\mu\text{m}/\text{m}$  error on temperature and strain measurements. This is why carbon-coating, known to be hermetic to hydrogen, is mandatory for an implementation in repository cell.

#### 2.3.4.1 Developpement approaches to increase sensitvity and response time of hydrogen OFS sensor

In order to improve the sensitivity of standard singlemode silica fiber to hydrogen, Andra and Xlim proposed to introduce Metallic particles (Pd) into the silica cladding of optical fibers.

This design should protect the sensing metal from harsh environments, solving the well-known palladium deterioration [ref]. Embedding Pd into fibers should also improve the sensitivity and the response time of the distributed fiber gas sensor, by exploiting the mechanical strain induced by the crystal lattice expansion of Pd particles in contact with  $\text{H}_2$  gas.

The fabrication feasibility of this kind of optical fiber had been demonstrated using an original powder technology: many palladed fibers had been realized by Xlim before the beginning of the project [81] (Figure 28). Nevertheless, sensing performance of Pd particules fibers was not fully demonstrate. TRL was still around 2.

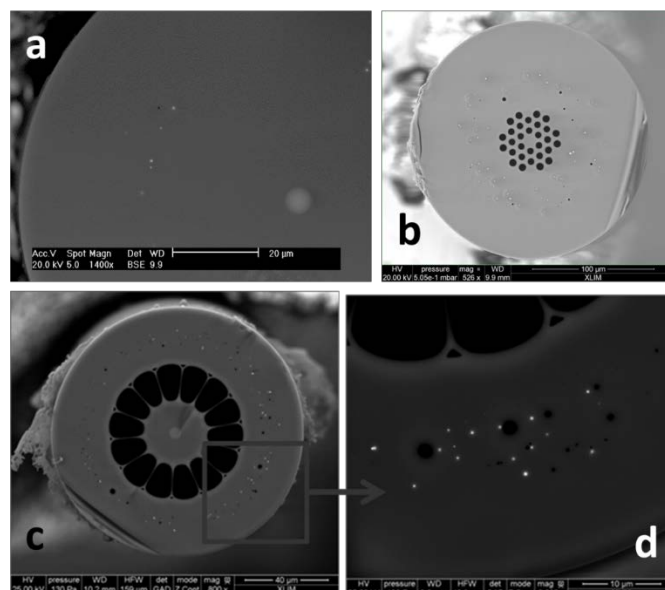


Figure 28: SEM pictures of cross-sections of three optical fibers with Pd particles embedded into the silica cladding realized by the powder in tube process: (a) a SiO<sub>2</sub>-GeO<sub>2</sub> core step index fiber. (b) a pure silica core microstructured fiber; (c) a SiO<sub>2</sub>-GeO<sub>2</sub> step index core with a microstructured cladding fiber; (d): zoom-in the cladding region of the fiber.

The work inside the modern2020 was dedicated

- Repeat and improve Pd-particles fibres and characterize performance during on\_line measurement under hydrogen
- Secondly, understand the diffusion mechanisms of hydrogen inside silica optical fiber in function of temperature, pressure, and optical fiber size. This work initiated in 2014 [82] where complete by the realization of calibration curve in order to help us to better link hydrogen concentration in air versus hydrogen concentration inside the fiber core

#### 2.3.4.2 Material & methods

Stack and Draw method were used to obtain optical preforms, which transformed into optical fibers thanks to the Xlim drawing tower.

Umons hydrogenation test bench (description could be found in paragraph 2.2.2.2 ) were used for on-line measurement performed by the NBS7020 Neubrescope (see neubrex line up in the neubrex.com website)

#### 2.3.4.3 Results

##### 2.3.4.4 Modeling hydrogen calibration curve

As illustrated in Figure 26, hydrogen concentration in air induces hydrogen migration into the optical fiber silica core. It is a reversible phenomenon with a saturation level. The maximal concentration level depends on temperature and pressure. It is very important to keep these dependencies in mind because they modify the calibration curve of the developed hydrogen sensors.

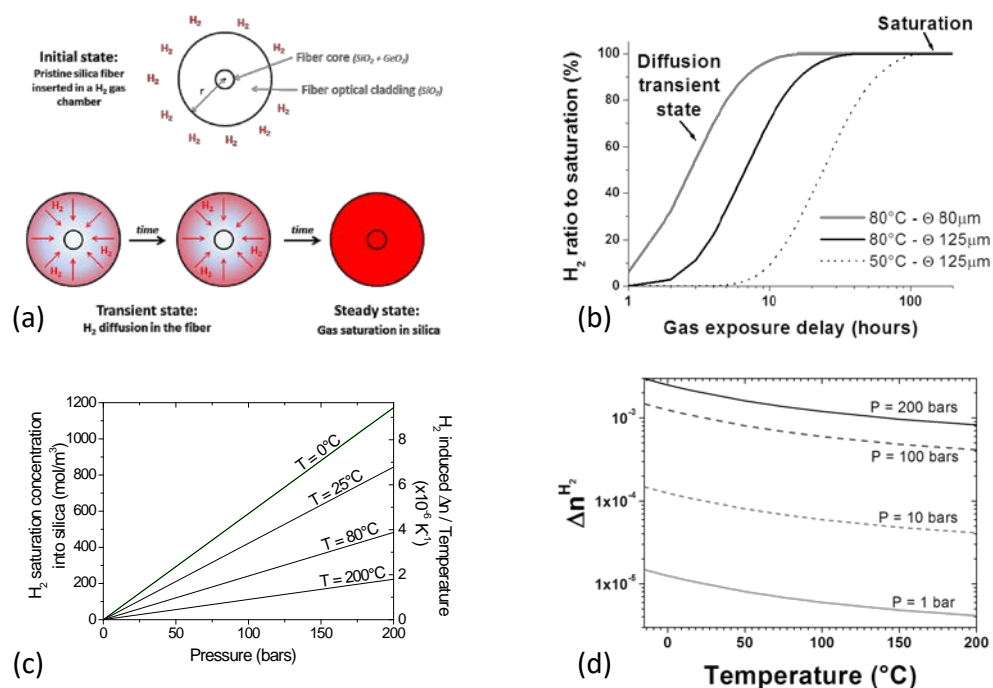


Figure 29: (a) Scheme of H<sub>2</sub> diffusion process into a silica fiber, (b) Evolution of H<sub>2</sub> concentration (normalized to saturation concentration) in the fiber center for different fiber diameters (80 μm and 125 μm) exposed to H<sub>2</sub> gas under a pressure 175 bars and at different temperatures (50 °C and 80 °C). (c) Evolutions of H<sub>2</sub> concentration at saturation and of the variation of the refractive index of the fiber core, versus H<sub>2</sub> gas pressure applied on the exposed fiber, at different temperatures. (d) Variation of the refractive index of the fiber core induced by H<sub>2</sub> at saturation for different pressures versus the temperature

Once hydrogen diffusion process is understood, the second step is to model the physical mechanism that provokes Brillouin frequency shift when H<sub>2</sub> diffuses into silica. We discovered that it is not only due to refractive index change, but also to acoustic velocity change. We performed Rayleigh and Brillouin backscattering simultaneously on H<sub>2</sub>-loaded and pristine fiber samples with the instrument Neubrescope NBX-7020F (see Figure 30). Shifts of backscattered Rayleigh and Brillouin frequencies have been continuously measured during 15 days following the hydrogenation stage (i.e. during H<sub>2</sub> out-gassing at ambient air). Rayleigh frequency shift provides the refractive index variation according to the following equation

$$\Delta n^{H_2} = -n \frac{\Delta V_R}{V_R}$$

We checked this measurement associating another optical fiber sample that included a Bragg grating. We injected this value into the measured Brillouin frequency shift and deduce the evolution of acoustic velocity  $V_A$ :

$$\Delta V_A^{H_2} = \frac{\lambda}{2n} \left( \Delta V_B - \frac{V_B}{n} \Delta n^{H_2} \right)$$

As detailed in [82], when hydrogen diffuses into silica, it induces a variation of refractive index, up to  $1.2 \cdot 10^{-3}$ , and an acoustic velocity increase in the order of 5.2 (m/s) / (% mol H<sub>2</sub> dissolved in silica).

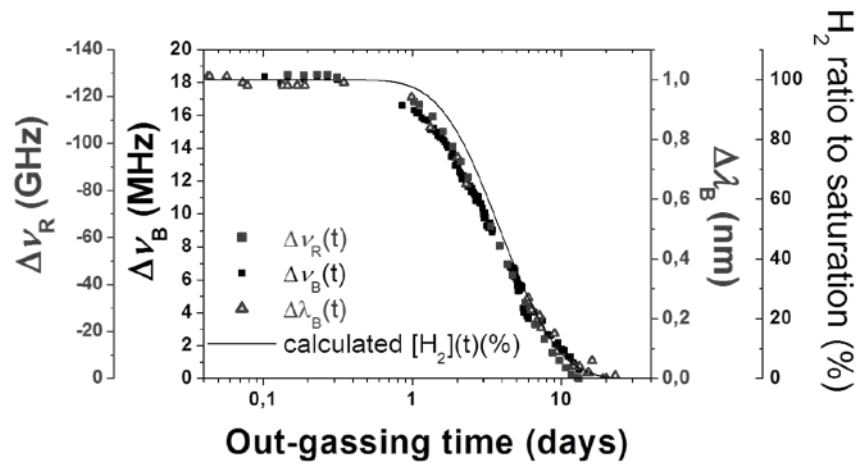


Figure 30: Time-evolution of (i) the Rayleigh frequency shift (grey squares with left axis), (ii) the Brillouin frequency shift (dark squares with left axis), (iii) the Bragg grating wavelength (opened grey triangles with right axis), (iv) calculated normalized concentration of H<sub>2</sub> (dark line with right axis), during H<sub>2</sub> out-gassing of the SMF (exposed up to 200 bars of H<sub>2</sub> at 80 °C during 60 hours).

Based on these results, the sensitivity of the sensing chain can be derived and is not sufficient. We then had to quantify how the embedded palladium particles were enhancing the sensitivity to hydrogen.

### 2.3.4.5 Experimental results with Palladed fibers

New fibers based on the previous approach built: a Germanium doped core surrounded by an air-hole-layer, itself surrounded by a silica cladding including Palladium particles. We varied the palladium quantity, the size of the holes (d) and the pitch (Δ).

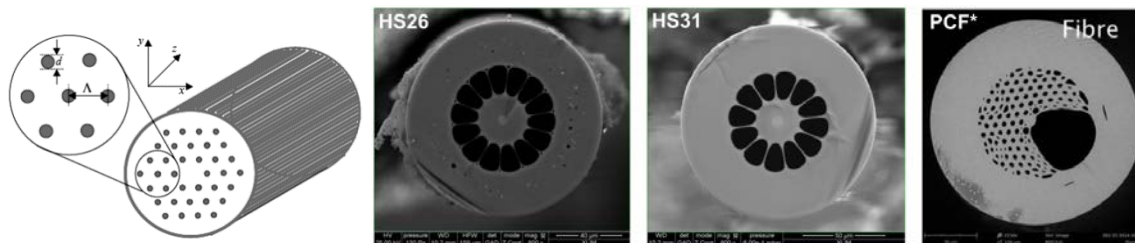


Figure 31: sketch of the special fiber with Pd in the cladding and SEM pictures of the three drawn fibers

Three fibers were obtained, illustrated in Figure 28. Several samples were prepared and provided for hydrogenation stage. The palladed fiber is called HS26. Xlim also drew its twin (similar optogeometrical parameters), however without palladium in the silica cladding, in order to be able to quantify the impact of metallic particle. Then Xlim designed and drew a fiber whose material ratio is strongly different, to determine the effect of the silica material desorption. It was called “PCF”. Optical fiber characteristics are detailed in Table 6.

Table 6. Optical fiber characteristics and measured scatterings under hydrogenation.

Fiber	Sample Name	Lg Length	Optical losses	Hydrogenation	
				$\Delta v_R$ , GHz	$\Delta v_B$ , MHz
“HS26”: 0.5% mol. PdO, $\phi_c=5.7\mu\text{m}$ , $\Delta n=8.10^{-3}$ , $d/\Lambda=0.94$	HS26-G	2 m	8.4 dB	Not exploitable	
	HS26-H	1.1 m	9 dB	Not exploitable	
	HS26-I	1.2 m	7.9 dB	-90	-18
	HS26-J	1.5 m	9 dB	Not placed under hydrogen	

	HS26-K	1.45 m	9.15 dB	Not placed under hydrogen	
“HS31”: Air-hole fiber without palladium. 0% mol. PdO, $\phi_c=7\mu\text{m}$ , $\Delta n=5.10^{-3}$ , $d/\Lambda=0.9$	HS31-B	8 m	0.55 dB	150	-26
Standard Fiber G652	G652	5 m	0.16 dB	150	-21
PCF	HS-PCF	< 1m	5 dB		-22.5

Samples were exposed to hydrogen at 200 bars, 80 °C, 60 hours for two days in 2016, January. All the samples were characterized in desorption by using a Neubrescope NBX-7020F. Measured Brillouin and Rayleigh frequency shifts are detailed in Table 6. Results are disappointing, opposite to expectations.

First, the palladed fiber HS26 has smaller frequency shifts that the reference fibers HS31 and G652. We are not confident in the acquired measurements because attenuation losses were very important, more than 8 dB/m prior to hydrogenation. When the sample is placed under hydrogen, this value increases even more, reaching the total signal to noise ratio of the Neubrescope, about 10 dB. The losses come from (i) the fiber itself, (ii) its splices (iii) its poor tolerance to curvature. To endure hydrogenation the sample must be wounded on a drum, increasing drastically the attenuation losses of the sensor, and compromising the measurement. Finally, it is worth noting that 2 days of hydrogen exposure is short to reach saturation, especially with special fibers whose response are not already known; HS26 fiber might not have reached saturation of hydrogen in the core.

Second the PCF fiber with large access to the fiber core should sense the hydrogen more rapidly, which is not obvious.

Figure 29 plots the Brillouin frequency shift evolution versus time. Hydrogen diffuses out of the reference G652 more rapidly that our opened fiber “PCF”.

Since the fiber HS31 has similar desorption kinetics that the PCF fiber, we assume the holes play an important role in the diffusion process and should be modeled prior to further experimental investigation.

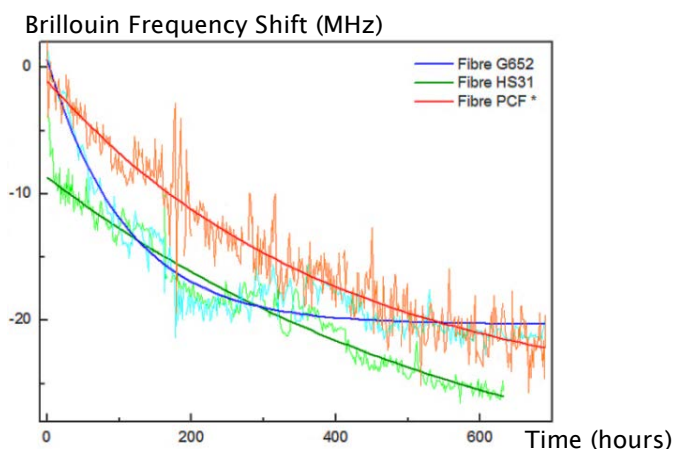


Figure 32: Comparison of Brillouin peak shift for G652, HS31 et HSPCF Fibers in desorption.

A second hydrogenation run with in-situ measurements has thus been organized in July 2016 in UMONS facility, at 60 bars of hydrogen and 70 °C. Measurements are illustrated in Figure 30. To be able to compare with the previous desorption test, the temperature influence should be decorrelated. However, noise is too high to be able to conclude and process data correctly. Two other fibers have been drawn and once again faced very high losses, especially when wounded (bad tolerance to curvature).

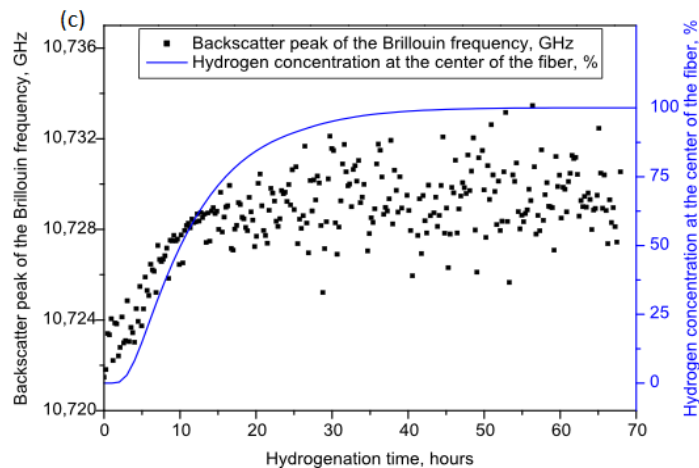


Figure 33: measured Brillouin frequency of the palladed fiber HS26 during hydrogen loading

To summarize, Rayleigh and Brillouin measurements in palladed fibers remains a challenge because of very high propagation losses. To improve attenuation losses, an important modification of the synthesis process, based on a powder method, is required. These developments are time consuming. Instead, we decided to explore, in parallel of these improvements, a new fiber design.

#### 2.3.4.6 Implemented back-up solution: birefringence approach

High losses of Pd-particles fiber attributed to small amounts of metallic particles diffusing from the cladding to the optical core. To prevent such spreading, we decided to localize palladium inside capillary; more precisely, we made use of the Stress Applying Parts (SAPs) of birefringent fibers.

Measuring birefringence offers larger working amplitude. It is more promising that Brillouin scattering in situation of high propagation losses. It remains an interferometric process (not based on intensity variation). As such one can expect durable and long-term measurement.

The sensing parameter is birefringence of polarization maintaining optical fibers, with and without palladium in the rods (that create stress inside fibers). Design relied on modeling, regularly validated from experiments. Calculations were performed in silica rods with a surrounding corona/ring, with and without stress parts. The developed model also enabled to explain hydrogen diffusion kinetics difference. One example is proposed in Figure 31. It shows that hydrogen diffusion in the rods is the process that fits the experiment, rather than the hypothesis of hydrogen diffusion in the optical core.

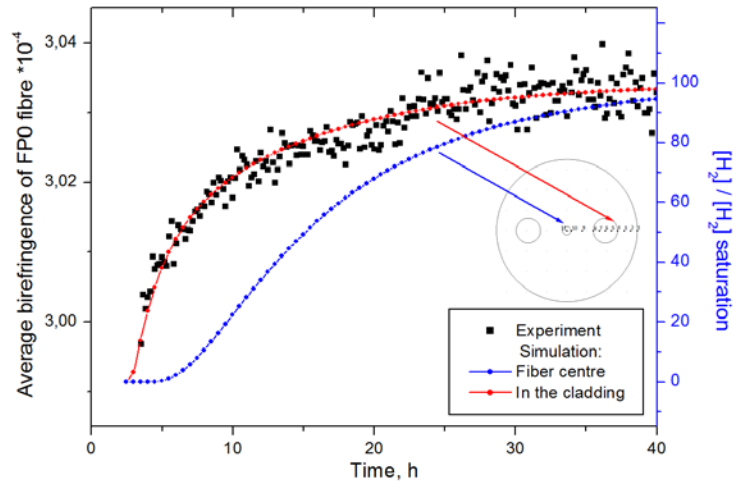


Figure 34: Comparison of Birefringence and hydrogen concentration in SAPs versus time.

2.3.4.7 Experimental results

Several fibers were realized The best fibers characteristics are listed in Table 7. They were placed in the hydrogen tank at 70 bars and 70 °C. The experimental set up were specific in order to distinguish the effects of temperature and pressure from the direct effect of hydrogen on the palladed optical fibers. We have quantified temperature and pressure dependence, which enables to isolate hydrogen influence. **Temperature results to be ten times more influent than pressure on birefringence.**

Table 7. realised birefringent fibers.

Fibre name	Material	Attenuation losses	Birefringence
FP0 (Undoped fibre)	SAL Glass	0.06 dB/m (L <sub>cut-back</sub> = 27 m)	3.19.10 <sup>-4</sup>
FP7	Mix of powders: SAL+PdO	20 dB/m (L <sub>cut-back</sub> = 0.7 m)	1.95.10 <sup>-4</sup> (2/2 Full SAPs)

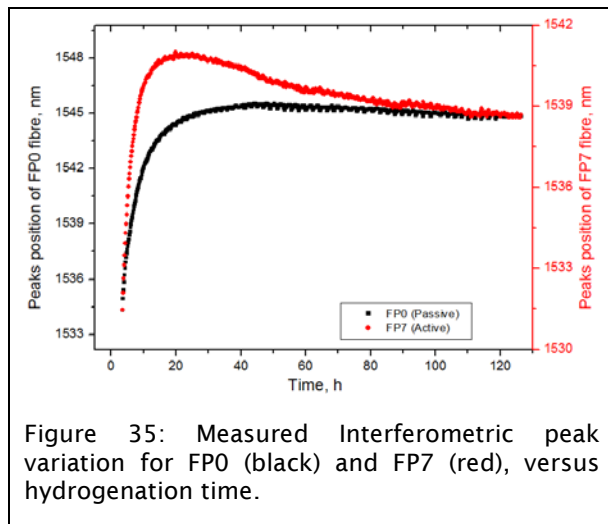


Figure 35: Measured Interferometric peak variation for FP0 (black) and FP7 (red), versus hydrogenation time.

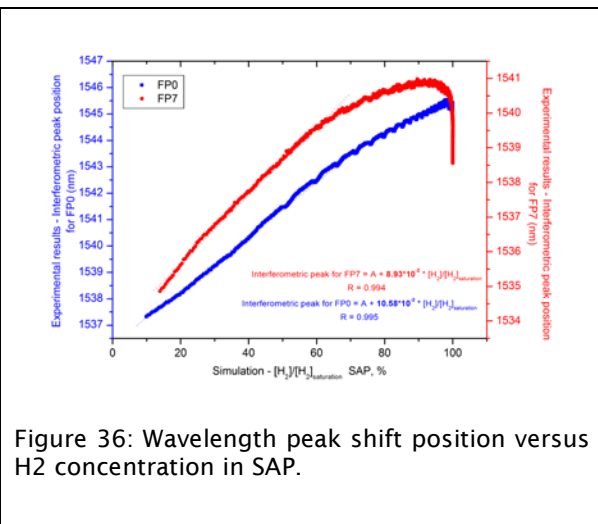


Figure 36: Wavelength peak shift position versus H2 concentration in SAP.

As illustrated in Figure 32, kinetics of hydrogen diffusion is different in the two optical fiber types. Birefringence variation in the palladed fiber changes under hydrogen exposure 0.6 % higher than the reference fiber without Pd. To increase the influence, in the future, more palladium should be inserted in the two rods.

What is more, the response of the palladed FP7 fiber is much faster than the reference FP0 fiber. As expected from modelling (see Figure 35.), under hydrogen exposure, birefringence passes through a maximum. Yet it presently remains difficult to anticipate the hydrogen sensing performances from these experimental curves.

These results demonstrate the influence of Palladium in the SAP compared to a fiber without metallic particles. Palladium increases the sensitivity and decreases the response time of the sensor.

Andra and Xlim applied for a patent in November 2017 [83] [83]. Currently, the demonstration is obtained on average along the samples: we have not yet a distributed sensor of hydrogen concentration.

#### **2.3.4.8 Summary for hydrogen sensing**

The goal of this subtask was to evaluate the performances of H<sub>2</sub> sensor, based on optical fiber. Two systems have been tested, both with palladed silica optical fibers: one based on Brillouin scattering in microstructured optical fiber (PCF), the other one based on birefringence in polarization maintaining fiber. Modeling and experiments were performed. A strong collaboration with University of MONS, a project partner, has been initiated and enabled to save time and improve results.

Both solutions proved to be sensitive to hydrogen, more than standard optical fiber. However, we have not managed to quantify the influence of palladium of the Brillouin frequency sensitivity to hydrogen. Optical losses compromise the measurements. Presently samples were less than 10 m long and, at saturation, measurements were too noisy.

The polarization maintaining fiber appears to be an interesting alternative solution of the Brillouin solution, being far less sensitive to optical losses, and less expensive.

A patent application has been submitted in November 2017 by Xlim and Andra on this new sensing scheme. Now publications are on progress. We are not able to perform distributed measurements inside palladed fibers. Feasibility was demonstrated in average along the samples. However distributed measurements are not identified as a bottleneck.

There remain to make hydrogenation cycles, with smaller amounts of hydrogen. Despite very promising results, we estimate that the TRL presently remains at 3.



### 2.3.5 Distributed gamma sensing

This paragraph details the work performed on distributed radiation sensing and obtained results. It relies on a Literature review and an experimental test performed during the IRMA irradiation campaign.

#### 2.3.5.1 Gamma sensing issues

Al or P doped fibers are known to be highly radiation sensitive [46]. Andra initially planned to make use of RIA (radiation induced attenuation) measured inside fibers with several dopant types and concentrations. Prior Modern2020, Andra had never done any test with such sensitive fibers.

Sensitivity of radiation measurements will increase with sensitivity of fibers, while reducing maximal distance range. For instance, if RIA reaches 10 dB/m at 1550 nm, if the OSA has 100 dB dynamic with 0.1 dB resolution, maximal length of samples is 10 m. A trade-off is to be found between distance range and sensitivity.

Another limitation is curing effects: RIA is not stable with time (at least in the first minutes). Thus on-line measurements are mandatory.

#### 2.3.5.2 Materials and methods

The attenuation measurements have been performed either using an OTDR from VIAVI operated at 1550 nm with one meter resolution or with a setup consisting in a white light source and a spectrophotometer, both from Ocean Optics. With the OTDR, only the RIA at 1550 nm is accessible whereas with the second setup, the RIA in the 900 nm – 2000 nm can be characterized.

The irradiation experiments were carried out at the IRMA facility of the IRSN at Saclay. The characteristics of the irradiation were:

- Continuous regime irradiation;
- Photons energy ~1.2 MeV (<sup>60</sup>Co source);
- Radiation doses up to ~1 MGy;
- Radiation dose rates of about ~2.6 kGy/h

We carried out some RIA measurements on three singlemode fibers with VIAVI's OTDR operating at 1550 nm. The investigated samples are called Ge, GeP, Al. These three fibers were all acrylate-coated. They had the following characteristics:

- Ge-sample: CMS fiber from iXBlue this singlemode optical fiber contains only Ge in its core, but in high concentration. As a consequence, it possesses a medium sensitivity to radiation and can act as the reference for this experiment.
- GeP sample: from Alcatel, this prototype singlemode fiber contains Ge in its core and a small amount of P in its cladding. It corresponds to a fiber with enhanced radiation sensitivity as typically about 20% of the light at 1550 nm propagates into the optical cladding.
- Al sample: provided by SCK-CEN, Modern2020 partner. This fiber was selected from A. Faustov PhD [46]. This singlemode optical fiber contains Al in its core, this dopant is known to strongly increase the fiber radiation sensitivity.

#### 2.3.5.3 Results

Figure 34 and Figure 35 contain the main results of these IRMA preliminary experiments: they plot the optical intensity measured at 1.55 μm inside three optical fiber samples connected together, before,

during and after irradiation. Time can be converted into considering the dose rate being 2.6 kGy/h for this set of experiments.

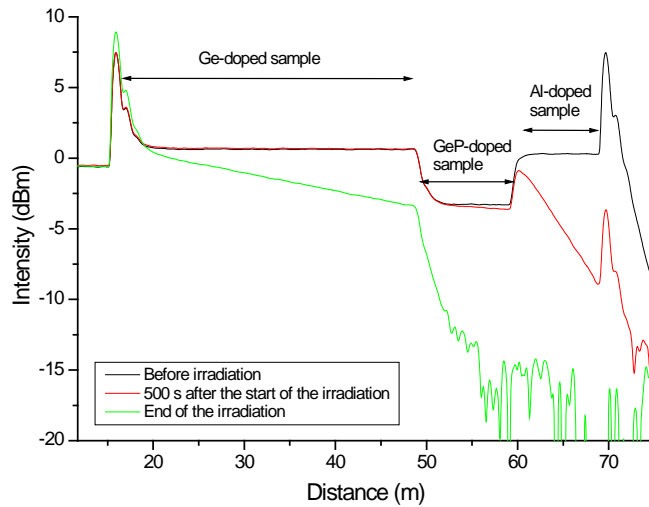


Figure 37 OTDR trace at 1550 nm measured before irradiation, at the starting and at the end of the irradiation. The three fibers have been spliced in series

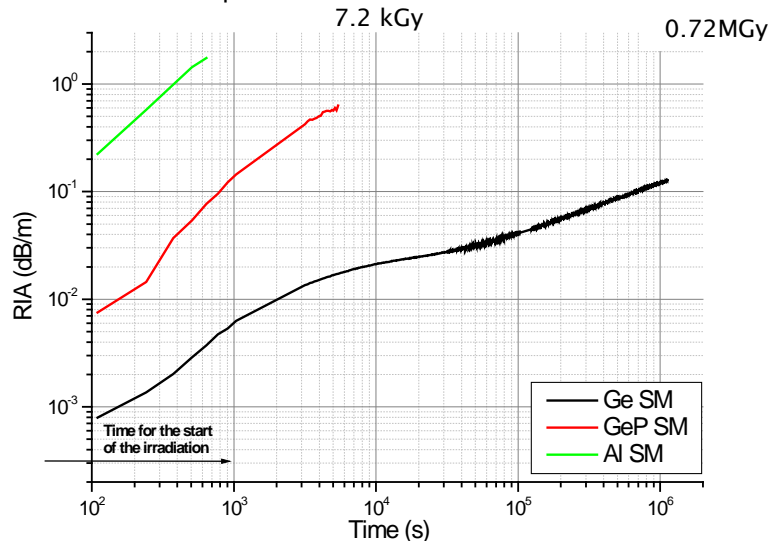


Figure 38: extracted RIA time evolutions at 1550 nm

By selecting the appropriate fiber, at 1.55  $\mu\text{m}$  we can cover the entire target radiation sensing range, from 0 to the MGy. As expected, the Al-doped sample is clearly the most radiation sensitive and such dose levels, only a few meters of this fiber is sufficient to totally absorb the signal. This fiber is the first one that is lost due to the strong losses at a dose of 470 Gy at 1.55  $\mu\text{m}$ . Then we lost the GeP-doped fiber at around 4 kGy, whereas the Ge-doped could be measured till the end of the irradiation. It is impressive to notice how a small amount of P in the fiber core is sufficient to increase its radiation sensitivity by a factor of more than 10.

In parallel with the OTDR measurements we performed spectral measurements on the GeP optical fiber that presents the intermediate radiation response in terms of sensitivity. The spectra obtained at different irradiation times are reported in Figure 36. 80000 s corresponds to 57 kGy

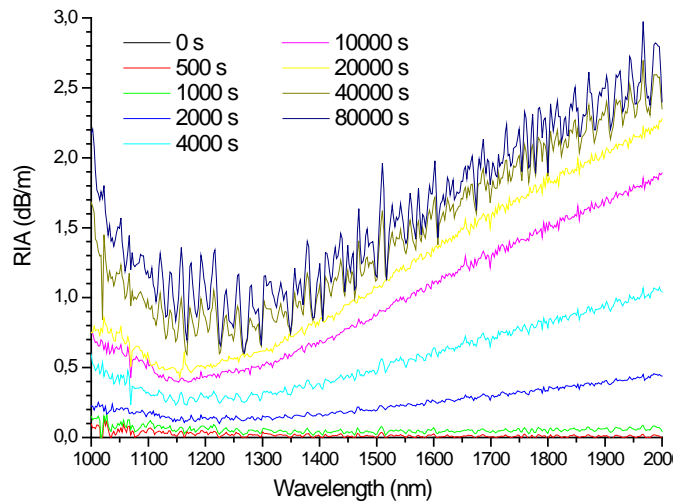


Figure 39: RIA spectral dependences measured in the GeP sample at different times during irradiation

Radiation influence is smaller around 1250 nm than 1.55  $\mu\text{m}$ . During the first year of radiation monitoring in Cigéo, to enhance sensitivity, longer wavelength such as 1800 nm could be favored, then working around 1250 nm could enlarge the radiation sensing working range.

Finally, Figure 37 compares the RIA recorded via the OTDR and the spectrometer to highlight if the differences between the used power levels (mW for OTDR,  $\mu\text{W}$  for white light source) lead to some differences in the GeP radiation response due to photobleaching.

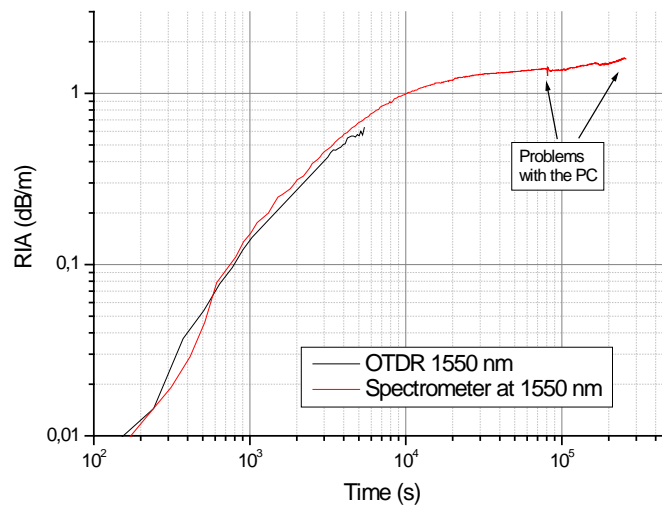


Figure 40: Comparison between the RIA growth kinetics at 1550 nm for the GeP fiber deduced from either OTDR or spectral measurements.

Even if the spectral measurements were interrupted by a failure of the computer controlling the spectrometer, this comparison shows similar results for the two acquisition chains: results were not affected by photobleaching.

#### 2.3.5.4 Summary of the radiation sensing

During Modern2020, Andra has managed to reproduce several Literature results. We tested three singlemode optical fibers selected for their various sensitivities towards radiation. Al-doped sample is clearly the most radiation-sensitive: 1m of fiber measured at 1.55  $\mu\text{m}$  could provide distributed measurement until a dose of 470 Gy, with a sensitivity of about 5dB/Gy. Then the GeP-doped fiber should be favored. It worked until 4 kGy. The Ge-doped could be measured until the end of the irradiation,

despite lower sensitivity. The optical fiber lengths and the working wavelength are two other parameters to adjust to the application.

However, while obtaining these calibration curves, a strong dependence of curing effect and coupled temperature and radiation influences was demonstrated. As a consequence, this work must be reproduced taking into consideration many more parameters. We cannot conclude yet on the best solution for underground repository monitoring. TRL remains at 3.

### 2.3.6 Compatibility of temperature and strain OFS with harsh environment

RIA does not directly inform on the radiation influence on temperature and strain sensing based on Rayleigh, Brillouin and Raman scatterings. Propagation losses will reduce distance ranges, from several kilometres to hundreds of meters. Then specific studies have to be performed to quantify the impact on temperature and strain sensing.

At the beginning of MODERN2020 project, recent results were reported [48]. Radiation influence on temperature measurement based on Raman scattering is not restricted to distance range limitation. Dramatic influence is observed (*Figure 38*): up to 50°C error on a 100 m sample. Error increases linearly with distance. Appropriate composition for the fiber allows reducing the amplitude of the temperature errors due to permanent effects of radiations but this is not sufficient to obtain acceptable resolution. Clear explanation of this phenomenon has been provided. It is due to the differential attenuation at the Stokes and Anti-Stokes wavelengths created by RIA.  $\alpha_S$  and  $\alpha_{AS}$  differ rapidly under radiation, and equation should be modified to take that effect into account.

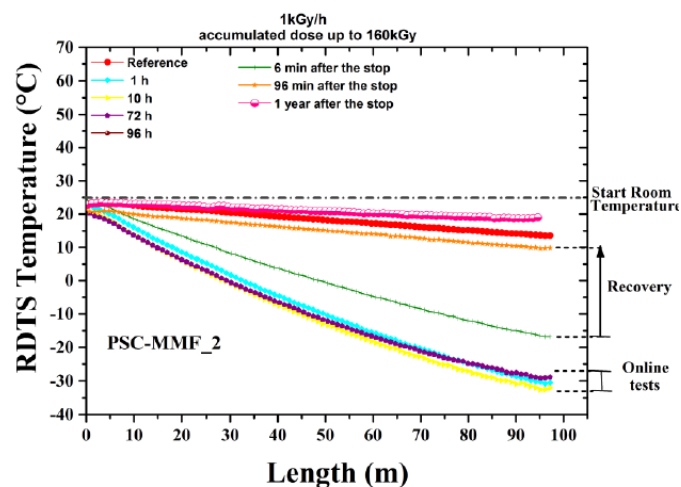


Figure 41: Measured temperature obtained from Raman scattering in a 100 m long sample of F-doped fiber, pristine (blue) and exposed to radiation doses.

Part of the work performed within MODERN2020 project by Andra was dedicated to a specific architecture, if any, able to provide truly distributed temperature sensing based on Raman scattering. Possibilities and limits of Rayleigh and Brillouin scattering paired with special cables, called “loose tubes”, which provide mechanical insulation, had also to be considered as a possible back-up solution.

The impact of radiation on Rayleigh based sensing system was poorly known at time of MODERN2020 project application. This is why Andra had initially planned to perform Rayleigh measurements on several optical fibers samples (with different dopants, primary coatings, virgin and irradiated fibers...) in order to compare Brillouin and Rayleigh strain sensing performances.

Finally, when MODERN2020 project was launched, Andra had already evaluated the influence of radiation on strain sensing based on Brillouin frequency shift. From post-mortem analysis presented in *Figure 39*, it seemed that influence is unneglectable but could remain appropriate for Cigéo application for a specific F-doped fiber. Then two questions remained to be considered: whether these post-mortem analyses were representative and if this special fiber could be implemented in a strain sensing cable.

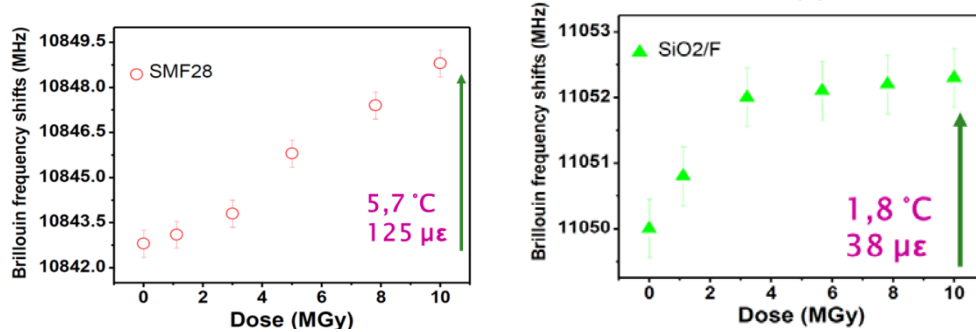


Figure 42: Measured Brillouin frequency shift for standard fiber with Ge dopants (left) and F-doped fiber (right) [47]

Finally, on top of radiation, hydrogen influence has to be considered when performing accelerated ageing tests on sensors. Figure 40 shows the dramatic influence of hydrogen on strain and temperature sensors based on Brillouin scatterings. It is even worst for temperature sensors based on Raman scattering, as illustrated in Figure 40 and presented in [49]. Prior MODERN2020, Andra had tested carbon coating, which proved to be efficient (and mandatory) to prevent hydrogen diffusion.

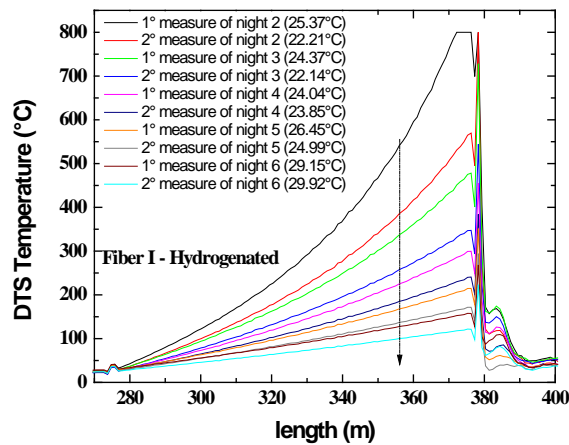


Figure 43: Influence of hydrogen exposure on Raman scattering.

Question to be addressed within MODERN2020 project is whether the hermiticity of carbon-primary coating is stable in time, despite irradiation conditions.

### 2.3.6.1 Challenges on distributed Strain sensing

Brillouin scattering is the reference solution selected to obtain distributed strain measurements. Nowadays, there are about 10 suppliers worldwide that offer Brillouin strain distributed sensing devices. Maximal distance range is larger than 30km; best spatial resolution is 1cm. Since the interrogator can be placed in safe rooms, far from repository cells, where maintenance is possible, the interrogation technique was not a development topic during this project: measurement were performed with a commercial device that provides stimulated Brillouin scattering profile (SBS). Andra work was dedicated to the sensitive cable design, realization, and performance evaluation, both in normal conditions and after accelerated ageing stress. First, the choice of the primary coating, second the design and realization of the external sheath. Once realized, question was the possible strain sensing performance differences between “naked” optical fibers and jacked optical fiber (cable).

Previous studies regarding the permanent radiation effects on the Brillouin scattering signature of optical fiber have shown that two phenomena impact the SBS sensor response:

- i) the Radiation Induced Attenuation (RIA) which limits the sensing distance,
- ii) a Brillouin frequency shift, up to 5 MHz, is observed at a cumulated dose of 10 MGy [48] on Ge-doped fibers, reduced to approximately 2 MHz with F-doped fibers [47] [47]. This type of fiber was our target. We will call it radiation-hard (RH) fiber in the following. It had to be designed, realized then inserted into a strain sensing cable.

The first question to answer was whether these promising results obtained post-mortem remain valid on-line or if transient effects are observed. In 2016, in addition to post irradiation analysis, through on-going collaboration (independent from Modern2020), Andra and its partner performed steady-state measurements to follow the transient mechanisms occurring during the irradiation. Online  $\gamma$ -ray tests revealed no transient degradation of the Brillouin response during a low dose/rate exposure (1 kGy/h for ~ 6 days) up to cumulated doses of 160 kGy, in various types of fibers [49][52]. Within Modern2020, Andra had to evaluate whether the large tolerance to radiation of Brillouin scattering remains valid in case of on-line irradiation at our high dose rates.

Apart from Brillouin scattering, in the last year period, abundant literature has reported on the radiation influence on Rayleigh based sensors[53][54][55]; it seems Rayleigh scattering is poorly sensitive to gamma rays until 1MGy total dose. Andra wanted to confirm these promising results. In the same optical fiber samples, both Brillouin and Rayleigh scattering would be measured during gamma irradiation.

Meanwhile, it has been shown that the radiation influence may significantly differ as a function of the fiber surrounding temperature, both on Rayleigh [56] and Raman scattering processes[57]. This is why a complementary goal was to evaluate possible coupled influence of temperature and gamma rays on Brillouin and Rayleigh scattering properties in silica optical fibers.

Finally, to the best of our knowledge, there is no aging test performed on optical fiber sensing cables yet; Literature reports in radiation influence on optical fibers in their primary coating, not in its external sheath yet. What is more, the durability of the primary coating is poorly documented. A challenging issue to tackle was therefore the choice of all the constitutive layers of the strain sensing cables, not only the silica core and cladding but all the surrounding layers.

Andra work could thus be summarized as follows:

- (i) design a radiation-hard optical fiber compatible with insertion into strain sensing cable
- (ii) (ii) select a primary coating suitable for harsh environment (both radiation and hydrogen)
- (iii) (iii) realize such optical fiber
- (iv) (iv) select or design a strain sensing cable
- (v) (v) insert the specific optical fiber (in its primary coating) inside the cable
- (vi) (vi) evaluate Brillouin and Rayleigh strain sensitivity \*(vii) and the possible evolution during aging of this global product. This last topic means checking whether the radiation influence on Brillouin and Rayleigh scatterings obtained post-mortem at room temperature remain similar on-line and at the working temperature. It also include verifying the durability of the hydrogen hermiticity of the product.

### 2.3.6.2 Material & methods

Andra owns several optoelectronic instruments to perform all kinds of distributed measurements. More precisely, for the project we used a Brillouin device from Omnisens, a Rayleigh unit from Luna, a Combined Rayleigh and Brillouin from Neubrex company. MODERN2020 enabled to buy a multiplexer for the Neubrescope instrument. With such devices, we can measure the Brillouin and Rayleigh shifts while creating events along silica optical fiber samples, with a total distance range of several kilometers, spatial resolution of few centimeters.

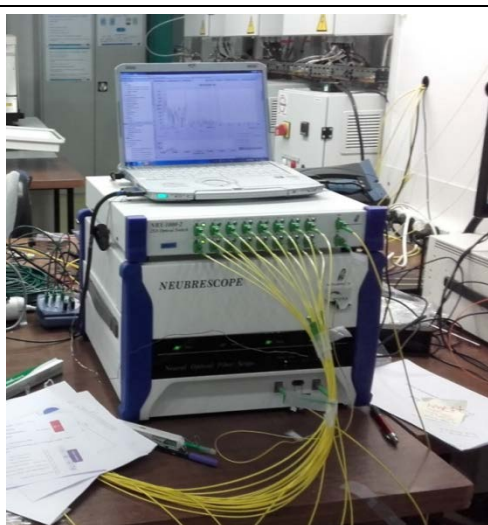


Figure 44: Picture of the Neubrescope instrument and its multiplexer bought with modern2020 funds, to enable measuring Brillouin and rayleigh scatterings in 8 optical lines sequentially and automatically

Flexible, mini armored fiber optic strain sensing cable with central metal tube, structured PA outer sheath, one optical fiber.  
strain range up to 1% (10000 µstrain)  
LLK-BSST V9 3.2 mm

Construction:

- 1) PA outer sheath, with structured surface with interlocking system
- 2) Metal tube SS316L for protection and hermetic seal
- 3) Multi layer buffer and strain transfer layer with interlocking system
- 4) Special strain sensing optical single mode fiber

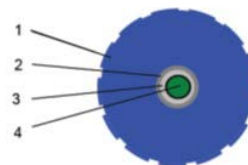
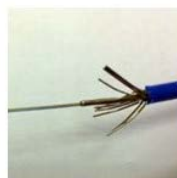


Figure 45: strain sensing cable developed within MODERN2020 project: Schematic of the cross section (left) and picture of the cable prior splicing, longitudinal view

Andra was assisted by two subcontractors to cover the entire sensing chain realization, namely to supply and develop special optical fiber sensing cables. iXBlue (France) has developed and supplied the optical fibers for strain sensing (singlemode fibre) and temperature sensing (multimode fiber). They used F-dopant exclusively, for high-tolerance to radiation. They selected a special primary coating (carbon) to prevent hydrogen migration into silica (the fiber material). BRUGG company (Switzerland) has inserted

the iXblue fibers into a sensing cable, made the cable external sheath to obtain a product suitable for civil engineering outdoor test. Andra selected the sensing cable called V9 whose schematic is proposed in Figure 42. The inner metallic tube should provide durability, on top of hermetic sealing (against hydraulic stress and hydrogen migration). The corrugated external profile should enhance the grip once embedded into concrete. The external diameter, 3.2mm, remains small which limits invasiveness.

Strain sensing cable are usually made of a tight sheath around the optical fiber, to ensure optimized transfer of mechanical field from the host material (where the strain measurement is requested) to the core of the optical fiber (where the measurement is actually performed). A drawback of such design is that the external sheath might induce (micro-) curvatures on the optical fiber, hence optical losses if the guiding properties are not carefully selected. Several performances of the final strain sensing cable are highly dependent on the optical fiber performances. For instance there are (i) the minimum bending radius, supposed to be 15 times the diameter, (ii) the crush resistance, claimed at 250 N/cm for standard V9 product (iii) the optical attenuation at 1550 nm, smaller than 0.5 dB/km, the central Brillouin frequency, 10.6 GHz, the Brillouin strain sensitivity, 450 MHz/%. Since the iXBlue fiber had to be inserted into a Brugg sensing cable, time has been taken to agree on required specifications: Product release in iXBlue and entry control in Brugg. We discussed on the maximal tolerated optical losses and the tensile strength the fiber should handle (in the present case, 200 kPsi, which was not a standard evaluation at iXBlue). We also agreed on the methodology to quantify these parameters. For instance, the measured optical losses depend on the size of the wheel where the fiber is wounded. Regarding temperature tolerance, we initially planned to replace acrylate constitutive material by polyimide. This was too different from Brugg standard production lines. This is why we decided to stick with acrylate material, yet high-temperature acrylate. The carbon-coated fiber also had to be covered by acrylate to enter the production line.

Once this product is realized, we would evaluate the performances of sensing cable performances, comparing them with naked fiber ones. We initially planned to perform:

- Optical losses evaluation to quantify whether the encabling process has degraded the optical fiber performances
- Rayleigh and Brillouin strain sensitivities measurements will be measured and compared, on the fiber alone and the sensing cable (the fiber in the external sheath)
- Irradiation tests to evaluate possible influence of the external sheath (degradation of material constituting the sensing cable?) on radiation tolerance. This include the possible influence of radiation on hydrogen hermiticity of the optical fiber and its coatings.

### 2.3.6.3 Ageing under irradiation

Ageing tests were designed in collaboration with several partners, IRSN (France) and SCK-CEN (Belgium) who could provide access to irradiation chambers, and University of Mons who was also willing to irradiate optical fiber sensors.

Total dose and dose rate are two influencing parameters. Regarding Cigéo application case, at the external surface of the HLW repository cell metallic liner, where OFS would be implemented, gamma dose rate reaches 1 Gy/h. For 100 years measurement, total dose reaches 1 MGy (air). This is why the IRMA <sup>60</sup>Co facility of IRSN (France, Modern2020 partner) was selected. In November 2017, optical fibers were measured on line while being exposed to dose rate of about 3.2-3.4 kGy/h, exact value depending on the sample position, up to a total dose of about 1MGy (in air, which is similar for SiO<sub>2</sub>).





In literature, no evidence of any evolution of strain and temperature sensitivity coefficients under gamma irradiation was ever reported. This is why we worked on loose samples and did not spend time to characterize systematically the strain sensitivities of fibers.

To ensure temperature regulated during irradiation, samples were packaged inside thermally-controlled silicones able to withstand radiation environments up to 1 MGy and to regulate temperatures up to 150 °C. They consist of a moisture-resistant braided heating resistor between two reinforced silicone layers. The assembly is vulcanized so as to achieve a homogeneous structure. Temperature is monitored and recorded by three thermocouples located inside the silicones (see Figure 43). Another thermocouple is positioned near the room temperature sample, to guarantee afterwards the independence of the result from chamber temperature variations. Fibers were coiled with a 9 cm diameter to limit curvature influence. In November 2017, samples have been irradiated at different temperatures, representative of the targeted application: room temperature (RT), 80 °C, 100 °C and 120 °C.

The fiber samples were taken from a reference Ge-doped fiber and the custom F-doped fiber. Indeed, on top of the developed samples (F-doped fiber), as a reference, we made use of a standard commercial Ge-doped fiber: Ge-doped fibers from Fibertronix (now Fibercore), with 5.2% Ge-SiO<sub>2</sub> core and pure silica cladding, with a carbon-polyimide primary coating.

For the online measurements, every sample was connected to the Neubrescope measuring device, located in a radiation-free zone. More precisely, the heated fibers were put in series after 60 m length of a connection cable fiber, while the sample at room temperature was connected after a 20 m long patch-cord. Each sample was measured on a specific optical line, thanks to the Neubrescope switch. Samples at ambient temperature were not inserted inside silicones. Both Brillouin and Rayleigh scatterings were measured during this ageing campaign. Regarding the large number of measurements to be performed, a trade-off between the measurement duration, the frequency scan range and the signal level was needed. For this reason, the following acquisition parameters were selected for the fibers tested at high temperature: distance range of 200 m, 100 cm of spatial resolution, 20 cm sampling interval, averaging count of 217, +1 dBm and +30 dBm respectively for the probe and the pump output powers, frequency range of [10.70 – 11.40] GHz with span of 2 MHz. For the sample tested at room temperature similar settings were used, except for different distance range limited to 100 m and another frequency range of [10.60-11.30] GHz.

Another sample, only with the specific F-doped fiber, was prepared and placed for on-line optical spectrum measurement, to determine the RIA.

Finally, on top of primary-coated optical fiber samples, the developed sensing was included into the accelerated ageing tests to evaluate whether the strain transfer function of optical fiber strain sensing cables (in other words, the function that links the concrete host material to the optical fiber core through the coatings and sheaths of the cable) might change after gamma exposure. 200 m of strain sensing cables were exposed to gamma rays. However, only Brillouin and Rayleigh scatterings were measured on-line on the sensing cable. Later in 2018, the irradiated cable samples will be placed on mechanical loading machines to evaluate possible evolution of the strain transfer function of the cable.

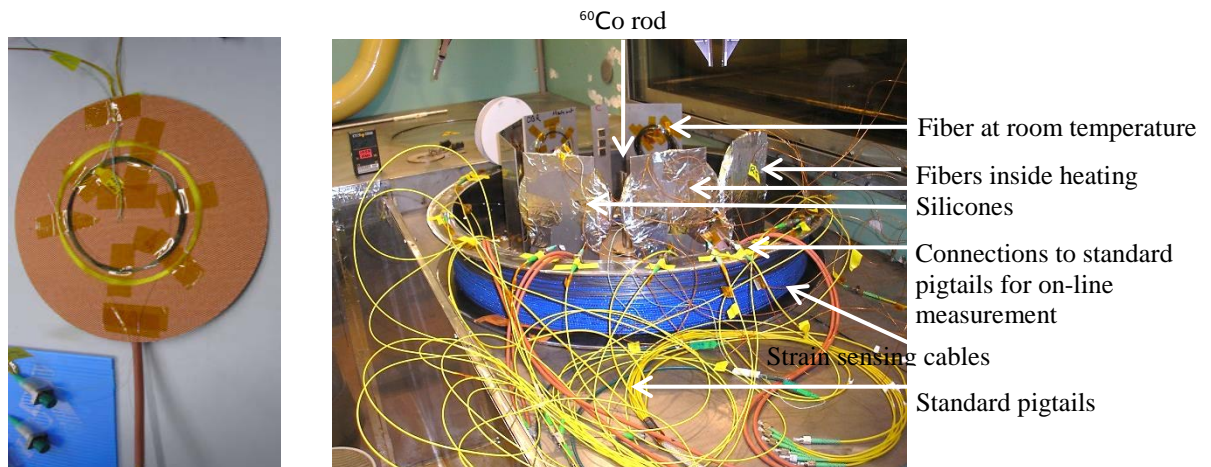


Figure 46 Pictures of the silicone with the optical sample and thermocouple (left) and the irradiation test (right) prior to the radioactive rod emplacement with optical fibers heated at three controlled temperatures

### 2.3.6.4 Results

### 2.3.6.5 Ageing: coupled Gamma and temperature influences on Brillouin scattering

Figure 44 illustrates three raw measurement acquired along the first optical line during the irradiation test. Reference measurement was selected before the heating and the irradiation started. The Brillouin frequency shift is plotted as a function of the distance along the optical fiber (s), in other words along (i) the jumper that links the instrument to the irradiation chamber, (ii) the F-doped fiber placed inside a heating silicone (approximately 30 m long) under irradiation, (iii) the reference Ge-doped fiber placed inside the same heating silicone (approximately 30 m long) under irradiation and (iv) the last jumper which ensures a loop configuration, required for Stimulated Brillouin measurement. The strong difference of about 70 MHz observed in the samples is induced by the imposed temperature. In the following, we will take the reference measurement after heating has started. What is more, distributed measurement is not useful in the presented test. This is why average measurement taken in the center of the samples will be extracted.

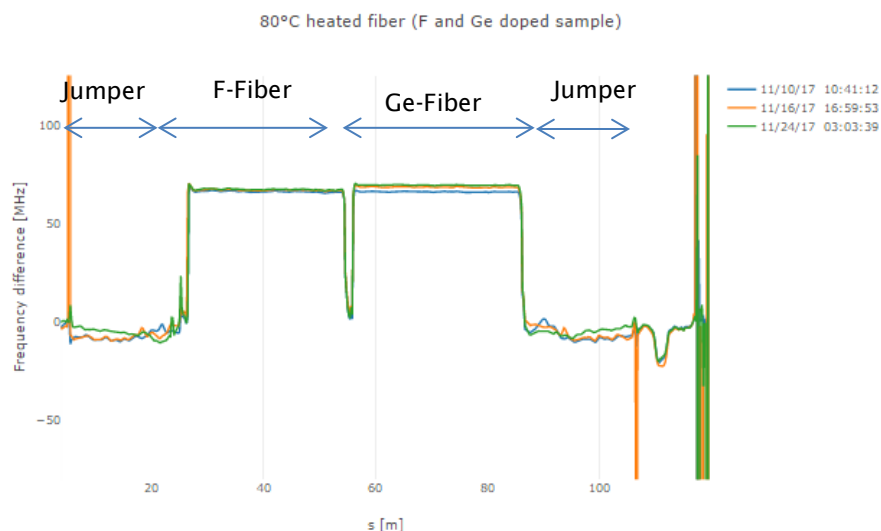


Figure 47 : Example of raw measurements: Brillouin frequency shift along one optical line (2 samples at 80 °C) while irradiated

More precisely, the heating procedure started several hours prior to the irradiation process, which allowed acquiring the references needed for comparisons of the radiation induced Brillouin frequency shifts at the four targeted temperature values. As the measurements could not be performed simultaneously for all samples, each test had its own reference. The choice then falls, for each sample, on the last measurement done right before the irradiation starting time. In this way, the retrieved Brillouin frequency shift, illustrated in Figure 46, is only due to the increasing radiation dose accumulated by the fiber, as the reference measurement already takes into account the sample temperature.

At room temperature, the slight irradiation chamber temperature variation, in the order of 2 °C, affects the measurement outcome. For instance, the Brillouin frequency shift measured in the reference Ge-doped fiber is presented in Figure 45, together with the measured ambient temperature. Temperature influence is obviously in the same order as the impact of radiation (if any). In the future, a regulation system should be added around the sample at room temperature, to ensure a very stable temperature and avoid the fluctuations due to the night-and-day temperature cycles.

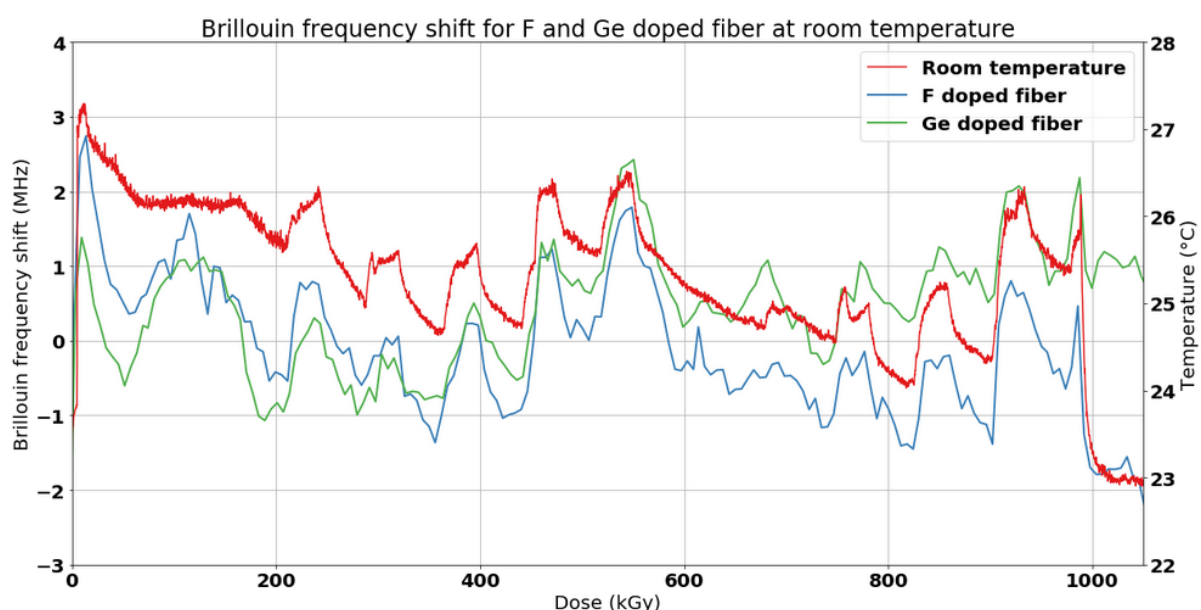


Figure 48 Brillouin frequency shifts measured in the two samples (Ge- and F doped fibers) placed at ambient temperature and the measured ambient temperature as a function of the received dose

For all reference samples, based on Ge-doped fiber, it is possible to observe a slight increase in frequency of less than 4 MHz at 1 MGy (see Figure 46). This result fully agrees with previously published measurements, where larger shifts correspond to larger total doses and/or higher Ge-doping concentrations [47][48][49].

3 MHz is very promising for Cigéo monitoring because it corresponds to only 60  $\mu\text{m}/\text{m}$  error in strain measurements, for the total dose of 1 MGy and for a Ge-doped fiber, which is not supposed to be the optimized fiber.

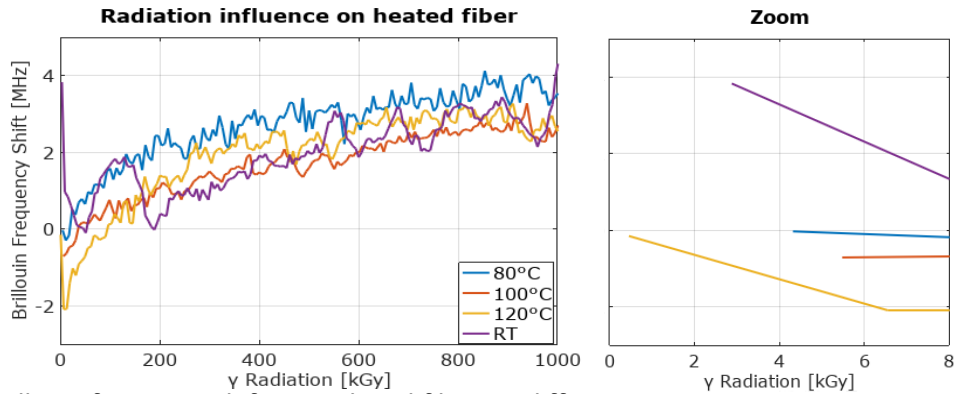


Figure 49 Brillouin frequency shift in Ge-doped fibers at different temperatures: total dose trend (left) and zoom at irradiation start (right)

The three Ge-doped-fiber samples placed at 80 °C, 100 °C and 120 °C did not suffer from room temperature variations; the regulation in the silicone was efficient. They all reveal the same trend with an increase of about 4 MHz, with a sublinear trend. Unlike Raman and Rayleigh scatterings, where temperature reduces the radiation impact, the coupled effect of temperature and radiation on Brillouin frequency shift is not significant, at least for this class of optical fibers. The main influence appears to be driven by different reference measurements, as highlighted in the Figure 46 (right).

The evaluation of the expected reduction of RIA under high temperature is also performed along with highlighting the temperature benefit effect in strain measurement based on SBS. In Figure 47, the Brillouin gain spectrum (BGS) central peak amplitude, relative to the reference value, is plotted as a function of the distance along the four samples, after a deposited total dose of 1 MGy. This amplitude is provided in dB by the device, which automatically subtracts the noise amplitude. The impact of radiation is huge with approximately 5 dB reduction in only 30 m propagation in the sample at room temperature. The three heated samples instead benefit from the reduction of the RIA reported in literature, with 2 dB attenuation over 30 m length, thanks to temperature increase. The three tested temperatures have similar positive influence on the samples and it is not possible to distinguish clear differences in the temperature effects between 80 °C, 100 °C and 120 °C. At the sample's entrance end, the Brillouin amplitude variation of approximately 1 dB is attributed to the connectors and the optical line quality.

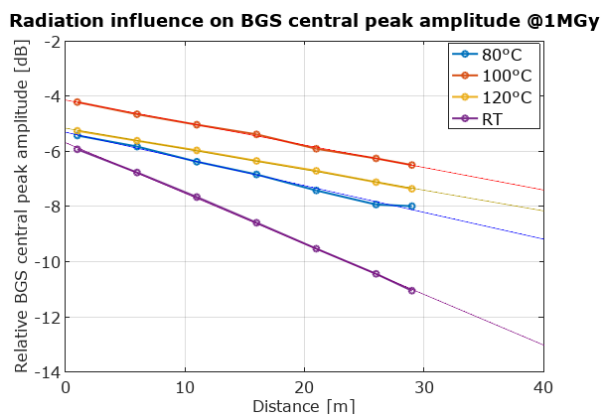


Figure 50 Radiation influence on the Brillouin central peak amplitude on the four samples at 1 MGy. A linear fit is plotted along the traces.

In Figure 48, the difference between the BGS central peak amplitudes considered at both the entrance and the exit ends of the Ge-doped fiber, divided by the sample length, is represented. This value is plotted as a function of the deposited dose.

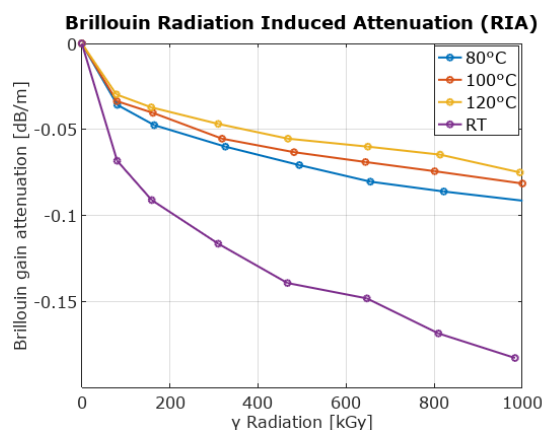


Figure 51 Radiation induced attenuation for the Brillouin gain spectrum central peak amplitude

Coupled effects of temperature and radiation are here evident. The environmental conditions, as here the presence of elevated temperature, while performing strain measurements based on SBS, should not be neglected during ageing tests. In our application, the temperature conditions that will be present in the underground repository for long-lived radioactive wastes are actually an advantage for Brillouin based optical fiber sensors, limiting measurement quality degradation, by approximately a factor 2. However, the maximal distance range of strain sensing based on SBS in radiation environment would not reach tens of kilometers anymore, several hundred meters seem in better accordance with available signal to noise ratio levels.

Preliminary evaluations were presented in a technical meeting dedicated to radiation impact on silica [59]. Then the results have been submitted to a prestigious conference, called OFS, organized in Lausanne in September 2018 [60].

Regarding the F-doped fiber, as expected, results are similar and even more promising than Ge-doped fiber performances. Brillouin frequency shift is presented as a function of received dose in Figure 49. With this customized optical fiber, we managed to reduce the Brillouin frequency shift down to 2 MHz, which approximately corresponds to 40 μm/m maximal error at 1 MGy total received dose.

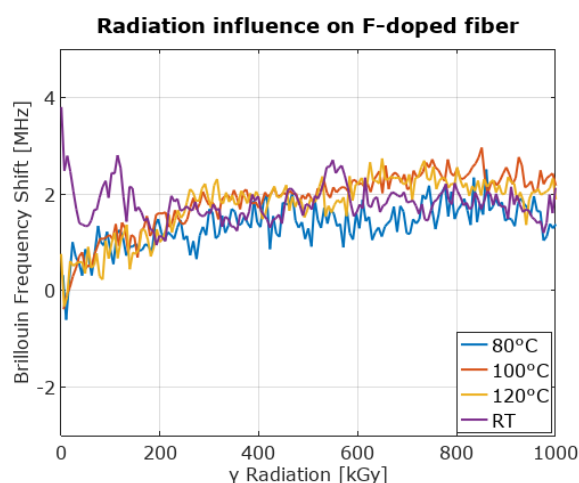


Figure 52 Brillouin frequency shift in F-doped fibers at different temperatures as a function of the received gamma dose, up to 1 MGy

Further analysis is on-going to determine the Brillouin gain, the signal to noise ratio, that is to say the maximal distance range one can expect with such optical fiber instrumenting a repository cell.

### 2.3.6.6 Summary for strain sensing

This work is a very positive result in view of the integration of OFS in nuclear facilities such as deep geological repository for nuclear waste. We are confident distributed strain sensing based on optical fibers is possible for decades despite harsh conditions.

Coupled effects of temperature and radiation improve the sensing performances of strain distributed sensors exploiting the Stimulated Brillouin Scattering in Ge-doped and F-doped single-mode fibers. At 80 °C, 100 °C and 120 °C, compared to room temperature, the radiation induced attenuation is significantly reduced. However, the Brillouin frequency shift is not modified by coupled temperature influence, as it remains in the order of 4 MHz at 1 MGy (air) for the Ge-doped fiber and only 2 MHz with the developed F-doped fiber, which approximately corresponds to 40  $\mu\text{m}/\text{m}$  maximal error in strain measurement.

Rayleigh scattering has proved to be a very promising solution for strain sensing. It is even less affected by radiation than Brillouin scattering. With the custom fiber based on F-dopants instead of Ge-dopants, the influence of radiation on Rayleigh frequency shifts is as small as -4 GHz, or 2.5  $\mu\text{m}/\text{m}$  error, whatever the working temperature (80, 100 or 120 °C). The influence of temperature is fully novel and should probably be published rapidly.

Further work is required to finalize data analysis, for all measurements acquired during the experimental campaign organized at IRMA facility (IRSN partner). From the Radiation Induced Attenuation, maximal distance range of distributed measurements will be determined.

The main difficulty is the degradation of carbon-coating hydrogen-hermiticity after 10 MGy dose. We must reproduce the test with the optical fiber we have developed within the project (the preliminary test was performed on a commercial fiber) and after several gamma doses.

Finally, we will evaluate the coupled impact of temperature and radiation on the external optical fiber coating (the sensing cable), whose influence might be important too for accurate strain sensing. Perspective for Autumn 2018 is to evaluate if sensing cable performances are similar with naked fiber ones. We plan to perform:

- Optical losses evaluation to quantify whether the encabling process has degraded the optical fiber performances
- Rayleigh and Brillouin strain sensitivities measurements will be measured and compared, on the fiber alone and the sensing cable (the fiber in the external sheath)

### 2.3.6.7 Overall conclusion: Towards a global sensing system

Based on the presented design and results, we can imagine the future system to obtain distributed measurements of strain, temperature, hydrogen and radiation.

Temperature is retrieved from Raman scattering in a multimode fiber. We have shown that

- Carbon-primary coating is mandatory to prevent hydrogen diffusion. Its efficiency was experimentally demonstrated. Its durability under harsh environment remains to be evaluated.
- F-doped fiber is mandatory to reduce the RIA but is not sufficient to suppress dramatic radiation impact on temperature sensing. Double-ended configuration proved to be mandatory and efficient, at the expense of temperature uncertainty, which reach 5 °C at 1 MGy.
- Maximal distance range remains to be quantified. We expect more than 100 m even at 1 MGy received dose.

TRL is presently estimated at 5 for distributed temperature measurement based on Raman scatterings.

Perspectives of the work are

- a. Evaluation of coupled temperature and radiation. Literature proves that temperature limits the negative influence of radiation. Hence, our results are pessimistic and we can be confident that temperature uncertainty will be smaller than 5° C.
- b. Evaluation of the influence of hydrogen on the irradiated carbon-coated samples.

As a back-up solution for temperature sensing, we evaluated the possibility to pair Brillouin or Rayleigh scattering with a loose tube (enclosing a singlemode fiber), to get rid of strain influence and be able to provide temperature measurement only. We proved that loose tube is efficient to isolate the sensing fiber from mechanical stress if implementation is carefully realized. It is an interesting back-up solution for temperature sensing, since temperature uncertainty actually remains similar for the three scatterings after radiation impact.

**Strain is retrieved from Brillouin scattering in a singlemode fiber.** We have shown that

- Carbon-primary coating is mandatory to prevent hydrogen diffusion. Its efficiency was experimentally demonstrated. However, its durability under harsh environment remains to be evaluated. Preliminary test have revealed a degradation of carbon-coating hydrogen-hermiticity after 10 MGy dose. Tests should be repeated for different doses and carbon-coating suppliers.
- F-doped fiber is mandatory to reduce the RIA and Brillouin frequency shift. Coupled effects of temperature and radiation have been quantified. Temperature reduces the negative impact of radiation on distributed sensors exploiting the Stimulated Brillouin Scattering. At 80 °C, 100 °C and 120 °C, compared to room temperature, the radiation induced attenuation is significantly reduced and maximal distance range will thus be improved. It remains to be quantified. The Brillouin frequency shift is in the order of 4 MHz at 1 MGy for the Ge-doped fiber and only 2 MHz with the developed F-doped fiber, which approximately corresponds to 40 µm/m maximal error in strain measurement.

We are confident distributed strain sensing based on optical fibers is possible for decades despite harsh conditions.

Rayleigh scattering has proved to be a very promising solution for strain sensing. It is even less affected by radiation than Brillouin scattering. With the custom fiber based on F-dopants instead of Ge-dopants, the influence of radiation on Rayleigh frequency shifts is as small as -4 GHz, or 2.5 µm/m error, whatever the working temperature (80, 100 or 120 °C). The influence of temperature is fully novel and should probably be published rapidly.

The qualified optical fiber has been inserted into a strain sensing cable. It has been placed under irradiation. We plan to evaluate if sensing cable performances are similar with naked fiber ones in Autumn 2018.

TRL is presently estimated at 5 for distributed strain measurement based on Rayleigh or Brillouin scatterings.

Regarding distributed radiation sensing, we tested three singlemode optical fibers selected for their various sensitivities towards radiation. Al-doped sample is clearly the most radiation-sensitive: it could provide distributed measurement until a dose of 470 Gy. Then the GeP-doped fiber should be favored. It worked until 4 kGy. The Ge-doped could be measured till the end of the irradiation, despite lower sensitivity. The optical fiber lengths and the working wavelength are two other parameters to adjust to the application. However, while obtaining these calibration curves, the strong dependence of curing effect and coupled temperature and radiation influences was demonstrated. As a consequence, this work must be reproduced taking into consideration many more parameters. We cannot conclude yet on the

best solution for underground repository monitoring. **TRL remains at 3**. Fortunately, many research teams have recently published on this topic and we can now expect rapid progresses.

Hydrogen sensing was initially envisioned with palladed silica optical fibers paired with Brillouin scattering in microstructured optical fiber (PCF). Xlim, in charge of this topic, established a model and provided calibration curves. Many special fibers were realized. A strong collaboration with University of MONS has been implemented to perform on-line measurements, during hydrogen exposure, for several temperature and pressure conditions. Optical fiber losses compromise the technical solution: presently, samples length cannot exceed 10 m and measurements remain very noisy. Xlim explored a back-up solution, based on birefringence measurement in palladed polarization maintaining fiber. Modeling and experiments were performed. Feasibility of hydrogen measurement has been demonstrated. A patent application has been submitted in November 2017 by Xlim and Andra on this new sensing scheme. Now publications are on progress. There remains to make hydrogenation cycles, with smaller amounts of hydrogen. Despite very promising results, we estimate the TRL remains at 3.

Based on these developments, we published[59][60][61][71] and patented [83] the results.

Figure 53 summarizes the proposed distributed measuring system. It is only a schematic and we are still far from an industrial system:

- The first three boxes are commercial equipment's, yet separated. Distributed birefringence measuring device is not off-the shelf but focuses many research developments and should become an industrial product in the coming years.
- The fibers are almost qualified but naked fibers would not endure repository cell construction. The strain sensing cable developed in the project will surely prove its durability in the coming months! For temperature and radiation sensing, blowing fibers into capillaries enables (i) placing sensors after the construction stage, and (ii) maintenance. Huge developments are not required to implement this solution; it would be an efficient and promising scheme. The main research topic is hydrogen sensing. Even if rapid and important results are obtain in laboratory, how to implement the sensitive optical fiber next to the wastes without deteriorating at emplacement should focus attention.

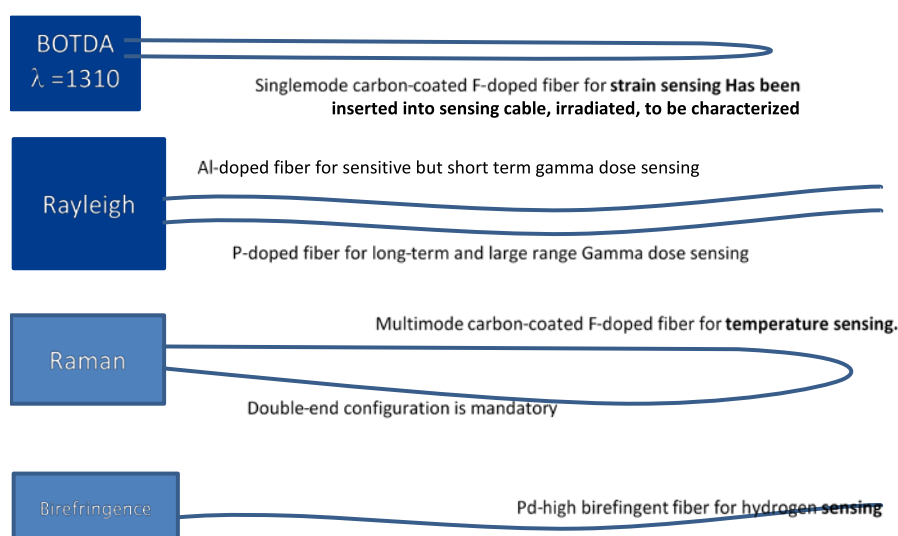


Figure 53: Schematic of the whole sensing system to provide strain, temperature, hydrogen and radiation distributed sensing



## 2.4 Active DTS for investigations of thermal conductivity, density and water content in the EBS (Nagra)

Distributed temperature sensing (DTS) is a well-established technology for measuring temperature along a fiber-optic (FO) cable. It yields a continuous temperature profile along the cable over a length of up to 10 km with a spatial resolution from decimeter to meter and temporal resolution of seconds to hours. Active heating of a FO cable combined with DTS, referred to as the "active DTS", has been receiving much attention recently as a tool to estimate soil moisture [87]

The method involves electrical heating of the FO cable and measuring temperature responses along the cable, which are strongly affected by the soil's thermal properties as in the case of a classic single needle heat pulse probe [84]. The needle length typically ranges from 3 – 10 cm (e.g. [88]) and, thus, the heat pulse probe measurement is considered as a point measurement. The advantage of the active DTS over the heat pulse probe is that it enables the estimation of thermal properties along a long profile with a typical spatial resolution of 0.25 – 2.0 m as defined by the DTS unit.

In the unsaturated porous media, thermal conductivity depends on density, porosity and water content. For an engineered barrier system (EBS) consisting of granulated bentonite mixture (GBM), emplacement density and water content are key monitoring parameters. These parameters determine the thermal conductivity of the EBS which controls the heat transfer from the waste.

The water content of the GBM is a known parameter at the time of emplacement. The dry density distribution of the GBM that basically determines the thermal conductivity distribution, is an essential quality control indicator at the time of EBS emplacement. The dry density of GBM was found to be heterogeneous when emplaced with screw feeders ([95][96]). Water content, on the other hand, provides information on a long-term resaturation of the EBS due to water influxes from the tunnel wall.

Therefore, demonstration of the applicability of the active DTS method to monitoring the state of the GBM of EBS is crucial.

Nagra installed a set of heatable FO cables in the Full-scale Emplacement (FE) Experiment underway at the Mont Terri rock laboratory (FMT) in Switzerland during its construction phase from 2012 until 2015 (e.g. [93]). The numerical (performed by Jung 2016 in Sakaki et al. 2017 see [97][98][99]) and experimental (performed by Jung 2015 in Sakaki et al. 2017) pre-studies conducted by Nagra indicated that the active-DTS generates data from which not only the moisture content of the GBM but also its emplacement density at the time of backfilling could be inferred. Based on these pre-studies, the applicability of the active-DTS method to monitor the state of the GBM was further examined through various tests in the EU Project MoDeRn2020. A series of experimental tests on estimating dry density and water content of the GBM used in FE experiment using active DTS were performed at the Grimsel Test Site (GTS) and Mont Terri rock laboratory (FMT).

This section summarizes the activities done by Nagra and results obtained from the experiments performed at these underground laboratories under well-controlled conditions:

Basic performance of the active DTS system (including identification of the optimal test parameters such as the heating power, heating time, sampling time, and so on). Experimental setup

Based on the pre-studies described above, a new experimental setup was designed and developed for the joint project as described in detail below.



### 2.4.1.1 Heatable fiber-optic (FO) cable

The heatable fiber-optic (FO) cable used in this study was the multi-component cable (BRUsens LLK-BSTH 85 °C) manufactured by Brugg Kabel, AG in Switzerland. Its outer diameter is 4 mm and smallest bending radius is 60 mm. Four optical fibers (two single-mode, two multi-mode) are embedded loosely in the center stainless tube that are surrounded by stainless and copper wires.

The total length of the FO cable used in this study was 150 m.

**Construction:**

- 1) Double layer PA outer sheath
- 2) Copper wires, total 0.83 mm<sup>2</sup> cross section
- 3) Stainless steel 316 wires
- 4) Gel-filled, stainless steel 316L, metal loose tube
- 5) Optical fibers with dual layer acrylate coating for increased micro bending performance

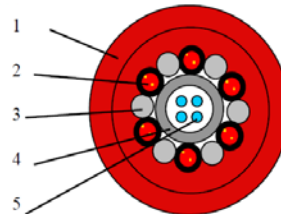


Figure 54: Schematic cross-section of the heatable FO cable (taken from Brugg Cables, 2015 [85])

Note: Fibers in metal tube are for temperature sensing, copper wires are for heating. Both ends of the 150 m-long FO cable were equipped with E2000 end connectors. The copper wires on both ends were extended by attaching a copper cable with a larger cross-section. This was done to avoid unnecessary temperature rise along the extended part.

### 2.4.1.2 DTS UNIT

The DTS unit used in this study was a Raman DTS in Fig. 2-13 (Silixa Ultima S). The cable length can be up to 5 km. Sampling resolution can be set to 0.127, 0.254, 0.508 and 1.017 m (spatial resolution is twice as much).



Figure 55 : The main DTS unit. Silixa Ultima-S (Silixa Ltd. 2015[103])

The typical temperature resolution depends on the distance and sampling time for a fixed sampling resolution as shown in Fig. 2-14. According to the user's manual, the ULTIMA-S offers a temperature resolution (the minimum temperature difference that can be distinguished) of approximately 0.1 °C for a distance of 0–200 m over a period of 30 s for a 0.127 m sampling resolution (gray line in the figure). At longer sampling time intervals the temperature resolution can be improved to 0.01 °C. Two PT100 temperature sensors can also be hooked up to the DTS unit for calibration.

As noted above, the length of the FO cable used was 150 m over which the temperature resolution does not change significantly as seen with a red box in Fig. 2-14. Throughout this report, all the DTS measurements were performed with the single-ended configuration.

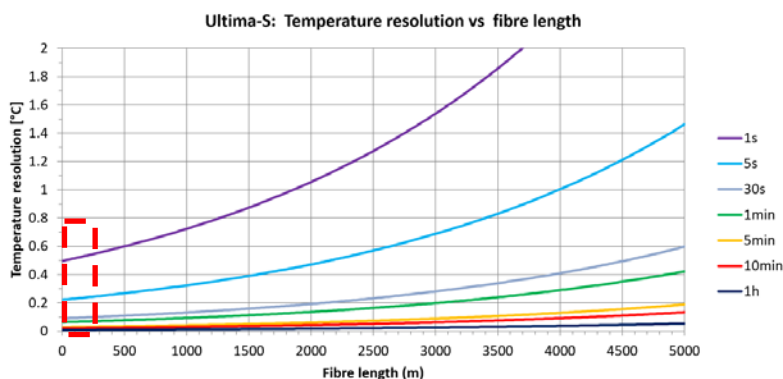


Figure 56: Temperature resolution over a distance of 5 km with 0.127 m sampling resolution

Note: Red box indicates the distance considered in this study (total FO cable length was 150 m, only cable meter 7-90 m installed in the GBM was considered).

### 2.4.1.3 Power unit

The power supply unit is to induce heat along the FO cable. Based on the pre-studies, a power supply unit shown in Fig. 2-15 (Delta Elektronika Model SM 52 AR 60, max current 15.6 A, max voltage 53.1 V) was selected. This unit can generate a power up to ~5.5 W/m with the 150 m long cable according to the calculation below;

$$\text{Max. power } P_{\text{max}} = I_{\text{max}} * V_{\text{max}} = 15.6 \text{ A} * 53.1 \text{ V} = 828.4 \text{ W}$$

$$\text{Thus, max power per meter} = 828.4 \text{ W} / 150 \text{ m} = 5.52 \text{ W/m}$$



Figure 57: Electrical current generator

Note: The values seen in the photo corresponds to  $37.9 * 11.9 \text{ W} / 150 \text{ m} = 3 \text{ W/m}$ .

The voltage and amperage to be used for the heating tests at the GTS were tabulated in advance for various power levels of 1, 2, 3, 4 and 5 W/m.

### 2.4.1.4 Grain size distribution of GBM

The first GBM material used in the early part of this study was known as mixture 2 ([91]) produced for pre-tests before the Full-scale Emplacement (FE) experiment underway at the Mont Terri rock laboratory (Müller et al. 2017). It was made by compressing the raw material to a dry density of 2,180 kg/m<sup>3</sup> and crushing it by an industrial blender to have the grain size distribution shown in Fig. 2-2. The initial water content was between 5.5 – 6.0 %. When analysing the experimental data, the water content used for the dry density calculation was fixed to 5.5 %.

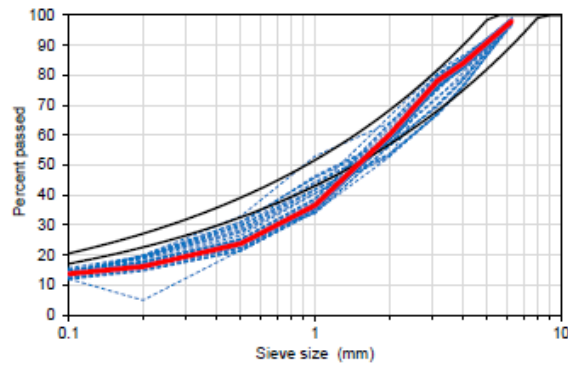


Figure 58: Grain size distribution of mixture 2 (Garitte et al. 2015)

## 2.4.2 General experimental setup

A series of heating experiments were performed in the VE cavern of the GTS. The setup was refined through the early phase of the experiments. Fig. 2-18 shows the schematic image of the current setup. The test section is illustrated as one box, however, in the real setup, this section comprises multiple boxes with different GBM conditions.

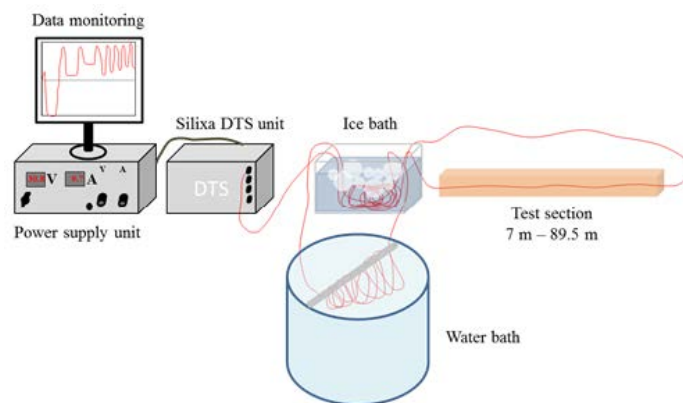


Figure 59: Schematic image of the experimental setup

Note: Note that the first ~ 90 m of the FO cable was used for the tests. The majority of the remainder of the FO cable was submerged under water in a large barrel to avoid unnecessary temperature rise along this part.

The FO cable starting at the DTS first runs through an ice bath where the temperature is controlled at or close to 0 °C. This part of the FO cable yields the temperature of the ice water also monitored by one of the two PT100 sensors attached to the DTS. Then, some meters of the FO cable run in air followed by the test boxes filled with GBM materials with varied conditions. The ambient air temperature was monitored with the other PT100 sensor. The temperature values from two PT100 sensors were used to check the temperature data in the ice bath and air (or calibrate the DTS measurements if needed). Finally, the rest of the FO cable (roughly 90 m) was submerged in a large water barrel. Due to the low thermal conductivity of air, without the water barrel, this long part of the FO cable heated up at the highest rate during the heating. This issue was resolved by placing the unused part of the FO cable (remainder) under water.

In the test boxes, the FO cable was fixed at the centerline of the boxes every 0.25 m using a tie wire (Figure 57). These small tie wires caused no influence on the DTS data. On the end plates, a 5 mm wide slit was

made. The cable length at the inlet and outlets of each box were checked via fingerprinting described above using a hair dryer



Figure 60: The FO cable fixed along the centerline of the test box

The setting parameters examined in this series of tests are as summarized in Table 8. Although testing all possible combinations was not possible, the tests were performed as systematic as possible.

Table 8 : Setting parameters examined

Parameter	Tested values	Remarks
Sampling resolution, $dx$ (m)	0.127, 0.254, 0.508, 1.017	All available setting with ULTIMA-S
Sampling time, $dt$ (s)	5, 10, 20, 30, 60, 120	Any values between 1-9,999,999 s
Heating power, $Q$ (W/m)	1, 2, 3, 4, 5	Max 5.5 W/m with the current setup w. 150 m FO cable
Heating duration, $t_h$ (hours)	0.25, 0.5, 1, 2, 3, 6	Reference heating 60 min was selected later.

## 2.4.3 Calibration test

### 2.4.3.1 Tests with varied density

Based on experimental results and data analyses, the major findings and conclusions can be as summarised as follows:

- The GBM material used (mixture 3, granulated, grain size distribution as shown in Fig. 2-3, water content = 5.5 %) exhibited a wide range of thermal conductivity as in Fig. 2-4. For this material, heating of FO cable induced temperature rises that were distinctly different so that the GBMs dry density can be inferred.
- The estimated thermal conductivity using the slope of the  $dT \ln t$  data indicated that their accuracy depended largely on two factors; 1) heating power, and 2) time duration of the  $dT \ln t$  (referred to as the data duration which is not necessarily the same as the heating duration) to be used.
- With a low heating power of 0.5 or 1 W/m, temperature rise induced was relatively small. The thermal conductivity estimated from the slope of the  $dT \ln t$  data seemed to have been affected by the noise in the data, thus, a low S/N ratio.

- With a higher heating power (i.e., 2 – 5 W/m), the estimated thermal conductivity values approached those estimated from the thermal analyzer results showing that higher heating power led to a better S/N ratio which resulted in more accurate estimation of the thermal conductivity.
- Thermal conductivities estimated with  $dT\text{-}lnr$  data duration of 15 min or shorter resulted in lower accuracy likely due to an insufficient number of data points to compute the slope. When  $d_t = 30$  s was used and with the first 3 min data were excluded, not much data points can be obtained.
- Thermal conductivities estimated with data duration of  $dT\text{-}lnr$  data from 20 up to 60 min led to an accurate estimation without the adverse effects from the box boundaries. Although the  $dT\text{-}lnr$  response was expected to be linear for the range of heating powers tested, the boundary effects may become detectable before 60 min for higher heating powers. For such cases, a shorter data duration, e.g., 3 – 30 min, is recommended. In the analysis shown above, 3 – 30 min and 3 – 60 min data led to practically similar results.
- Thermal conductivities estimated with data duration of  $dT\text{-}lnr$  data longer than 60 min showed that the estimated thermal conductivity was affected by the low thermal conductivity of the material boundaries, thus, underestimated. This was the most pronounced for 120-180 min data in the GBM with the highest dry density.
- The FO cable calibrated to varied dry densities of GBM mixture 3 showed a quasi-linear relationship. The fitted linear functions showed a high  $r^2$  value of 0.985 and the 95 % CIs around the target dry density of 1,450 kg/m<sup>3</sup> that Nagra has set when emplacing the buffer was found rather narrow ( $\pm 15.4$  kg/m<sup>3</sup>). The calibration functions also indicated smaller 95 % CIs for higher heating powers due to a sufficiently high S/N ratio.

The estimation of dry density based on the thermal conductivity computed using the slope of the  $dT\text{-}lnr$  data can be most accurate when the FO cable is heated with a power of at least 2 W/m and for a duration of 20 – 60 min.

It has to be emphasized that the duration of  $dT\text{-}lnr$  data to be used to compute the slope will have to be shorter if the GBM sample size is smaller, and/or with heterogeneity nearby such as in the case when the FO is attached onto shotcrete. Under such conditions, the heat will reach the boundary at earlier times. In addition, if the material components are different, e.g., with more water or sand particles, volumetric heat capacity would change. This might result in different behavior regarding the timing at which the non-linearity becomes distinct.

#### 2.4.3.2 Tests with varied water content

can be as summarised as follows:

- The GBM material used (mixture 3, granulated, grain size distribution as shown in Fig. 2-3, water content range of 5.5 – 24 % with a target dry density of 1,350 kg/m<sup>3</sup> exhibited a wide range of thermal conductivity as in Fig. 2-5. For this material, heating of FO cable induced temperature rises that were distinctly different so that the GBMs saturation can be inferred.
- The estimated thermal conductivity using the slope of the  $dT\text{-}lnr$  data indicated that their accuracy depended largely on two factors; 1) heating power, and 2) time interval of the  $dT\text{-}lnr$  (referred to as the data duration which is not necessarily the same as the heating duration) to be used.

- Only for the  $w_c = 24\%$  sample, the DTS-estimated thermal conductivity was substantially lower than that of the thermal analyzer. This observation was independent of the heating power and/or data duration. The cause for this remained unidentified.
- With a low heating power especially with 0.5 and 1.0 W/m, temperature rise induced was relatively small. The thermal conductivity estimated from the slope of the  $dT\text{-}Int$  data seemed to have been affected by the noise in the data, thus, a low S/N ratio.
- With a higher heating power (i.e., 2 – 5 W/m), the estimated thermal conductivity values approached those estimated from the thermal analyzer results showing that higher heating power led to a better S/N ratio which resulted in more accurate estimation of the thermal conductivity.
- Thermal conductivities estimated with  $dT\text{-}Int$  data duration of 15 min or shorter resulted in a lower accuracy likely due to an insufficient number of data points to compute the slope. When  $dt = 30$  s was used and with the first 3 min data were excluded, not much data points can be obtained.

#### 2.4.4 On-site verification of effects of shotcrete at Mont Terri

In the FE tunnel at the Mont Terri rock laboratory (FMT), the heatable FO cables were installed at the 11:30 and 0:30 o'clock positions as seen in Fig. 6-1a. The FO cables were loosely fixed using plastic clips roughly with 60 – 70 cm increments. Due to the highly undulated (resulting from irregular rock excavation surface) and rough surface conditions of the shotcrete, the FO cables appeared to be surrounded dominantly by air before the backfilling and, thus, by the GBM after the backfilling. With the goal to investigate how much the temperature evolutions due to heating of the FO cable are affected by the presence of the shotcrete, a set of heating tests were performed at FMT.

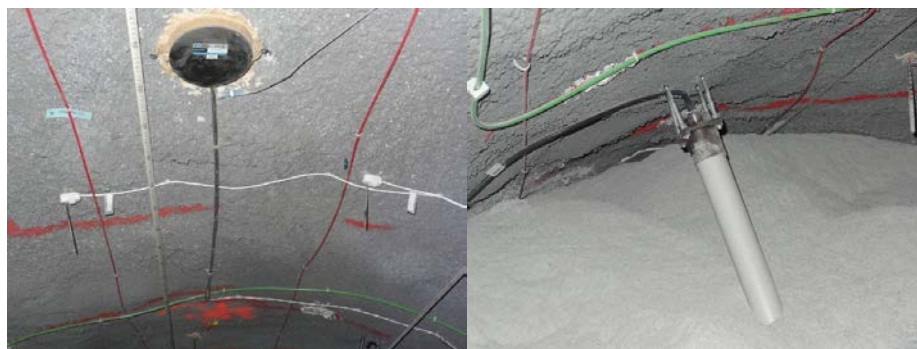


Figure 61 : Heatable FO cables (red) installed in the FE tunnel.

Note: a: In the photograph, the FO cables were attached loosely onto the shotcrete surface with 60 – 70 cm increments. Note that the surface of the shotcrete is highly rough; b: FO cable (in red) during backfilling.

##### 2.4.4.1 Experimental setup and procedures

A sufficiently large shotcrete domain in Gallery 08 at FMT was selected for the on-site verification heating tests. Three boxes with an "L-shaped" cross-section (2 m in length, 10 cm in width and height) were fixed onto the shotcrete as shown in Figure 59. The fiber-optic cable was fixed in the middle in height and at 5, 2 and 0 cm away from the shotcrete in top, middle and bottom boxes, respectively. The same plastic clips as used in FE experiment were used to fix the cable at 50 – 60 cm intervals. The FO cable was then connected to the DTS and heating units as schematically shown in Figure 59.

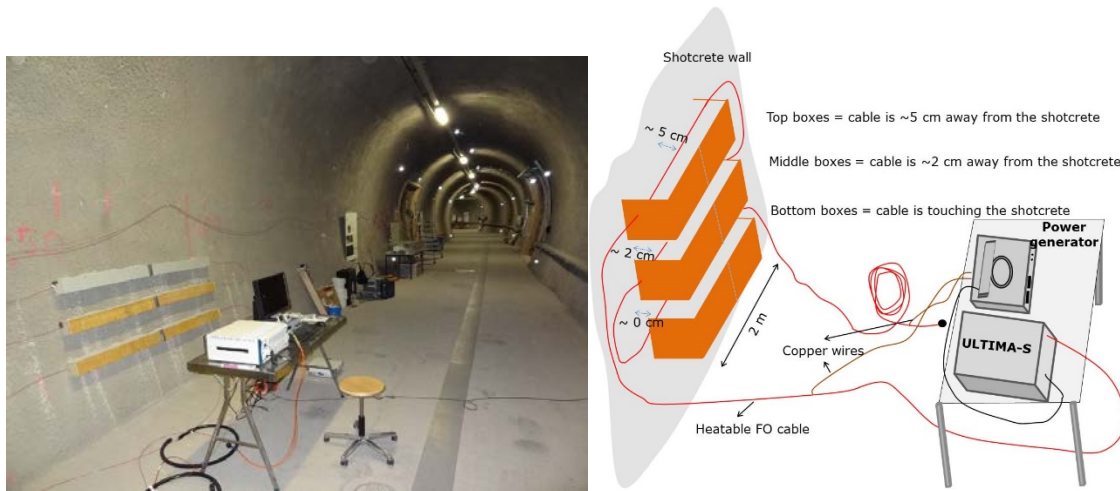


Figure 62: (left) Heating test site in Gallery 08 at FMT Switzerland (right) Schematic illustration of the heating test setup

In FE Experiment, the dry density of the GBM near the tunnel ceiling (Fig. 6-1 b) was estimated roughly as 1,350 kg/m<sup>3</sup>. These boxes were, thus, packed with GBM mixture 2 to a target dry density of 1,350 kg/m<sup>3</sup>.

table 9 : Selected conditions in three test boxes

Box	Packing condition	Cable condition*	Mass [kg]	Volume** [m <sup>3</sup> ]	Dry density* [kg/m <sup>3</sup> ]	Thermal conductivity*** K (W/mK)	Cable length [m]	
							Start	End
Top	Loose	~ 5 cm	31.13	21.20	1,390	0.263	7.41	9.19
Middle	Loose	~ 2 cm	31.27	21.17	1,390	0.263	11.35	13.13
Bottom	Loose	~ 0 cm	31.92	22.10	1,390	0.263	15.42	17.20
Shotcrete	-	-	-	-	-	1.38	-	-

\* Approximate cable distance to the shotcrete

\*\* Volume was determined based on the distance between the box wall and shotcrete. Surface roughness was not included in the volume computation, thus, the actual volume is slightly larger leading to a higher dry density.

\*\*\* Separately measured by thermal analyzer KD2 Pro under the similar dry density conditions, i.e., GBM mixture 2, 1,390 kg/m<sup>3</sup>

Three heating tests were performed with different heating powers of 0.5, 1.0 and 2.0 W/m. These powers were chosen because the heating of FO cables in the FE Experiment in early times (during 30.04.2014 until 02.02.2016) were conducted with 0.41 (102.72 W power-250 m cable) W/m and later tests to present have been performed with 1.03 W/m (257.64 W power 250 m cable). A separate detailed study at Grimsel Test Site (GTS) to further investigate the performance of the active DTS indicated that for the thermal conductivity range expected with the GBM being tested, 2 W/m results in a better sensitivity (i.e., good S/N ratio) to evaluate the state of the GBM material

## 2.4.5 Summary

The on-site heating experiments for investigating the effect of the shotcrete on the bulk thermal responses led to the following findings:

- The thermal conductivity heterogeneity resulting from the shotcrete-GBM interface had negligible effects in cases where the FO cable was 2 and 5 cm away from the shotcrete. For a longer heating/higher heating power, the effect may become visible.
- When the FO cable was fixed directly (but loosely) on the shotcrete, the effects from the shotcrete started to appear after a certain heating time (roughly 15 – 20 min or longer).



- Low heating power of 0.5 W/m resulted in more scatter in the estimated thermal conductivity. Higher heating powers of 1 and 2 W/m improved the noise-signal ratio.
- For the 1 W/m heating (the same power as those currently performed in FE experiment), heating duration of 15 – 20 min seemed optimal without introducing the effects from shotcrete.
- For the 2 W/m heating, the results indicated that the heating time may be shortened to 10 or 15 min. When such short heating time is used, sampling time may need be shortened in order to have a sufficient number of data points.

## 2.4.6 FE Experiment: Estimation of GBM state in June 2017

In the FE tunnel at the Mont Terri rock laboratory (FMT), the heatable FO cables installed at the 11:30 and 0:30 o'clock positions have been heated on a regular basis. During April 30, 2015 until February 2, 2016, the heating was done with a power of 0.41 W/m. From March 7, 2016 to present, the heating power was increased to 1.0 W/m.

The tests described in Chapter 6 indicated that the heating power of 1 W/m is the lower end and a higher power is preferred. Therefore, a set of heating tests were performed in June 2017 using the DTS and heating units whose performance and response have been well studied in the previous tasks.

### 2.4.6.1 Test setup and conditions

In the series of tests, the DTS unit and the current generator described in Section 2.5.3 (Fig. 2-15) were used. With this configuration and the 250 m-long FO cable installed in the FE tunnel, the heating can be done with a power up to 1.9 W/m. The heating tests were done with the following conditions. In this chapter, results from the heating power of 1.9 W/m are described.

- Sampling time: 30 s
- Sampling resolution 0.127 m
- Heating power: 0.5, 1,0 and 1.9 W/m
- Heating time 60 min (data duration: 15 min)
- Test dates: June 06 – 07, 2017
- Temperature was also recorded by Smartec DiTemp SR (sampling resolution: 1.02 m, sampling time 120 s) and Neubrex Neubrescope NBX-7020 (sampling resolution: 0.05 m, sampling time 30 s) simultaneously.

Figure 60 illustrates the schematic FO cable routing configuration along the FE tunnel. The FO cable starts at CM 97.8 m (Silixa at plug) at the 00:30 position o'clock position just behind the concrete plug. It extends above three heaters until CM 124.09 (Silixa at entrance of Loop1), then makes three rings in Gaps 2, 4 and 6 (each of which starts at 4:00 o'clock position and ends at 3:00 o'clock position, Fig. 7-2). After the third ring in Gap 6, the FO is routed at 11:30 and comes back to concrete plug.

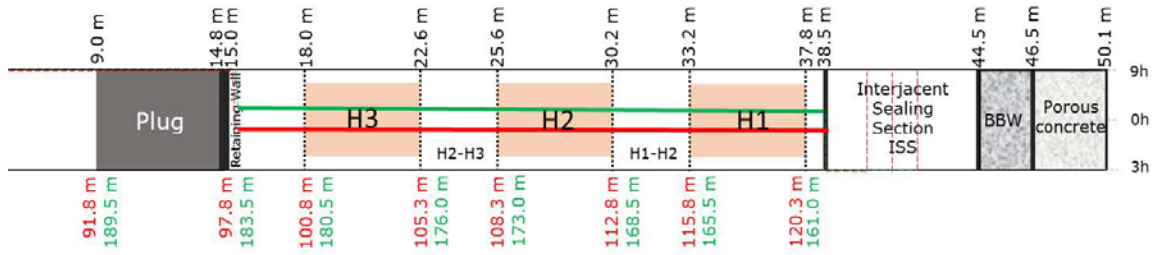


Figure 63: FO cable installed configuration.

Note: Black values: Gallery meters (GM), Red values: FO cable running in (CM in) meters with Silixa DTS, Green values: FO cable running out (CM out) values with Silixa DTS

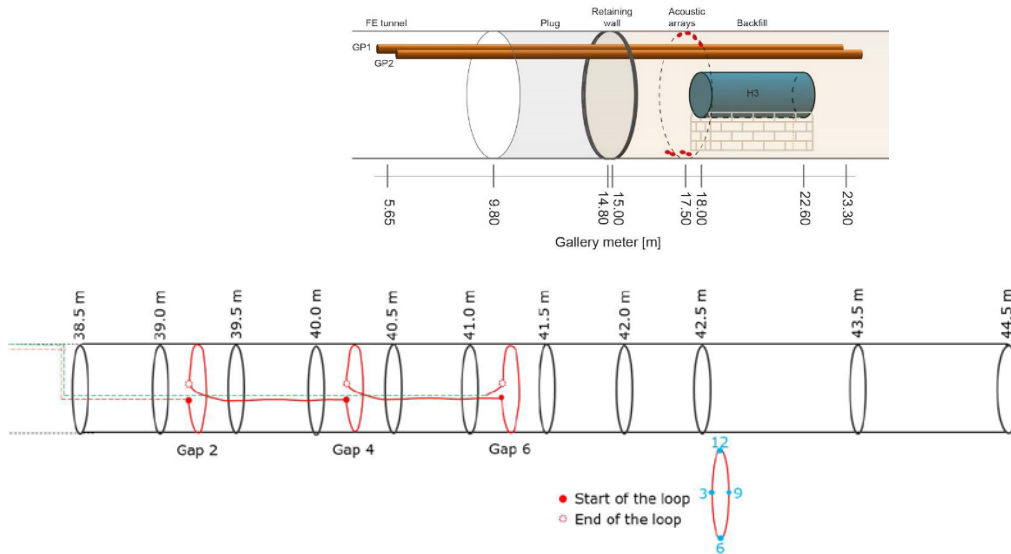


Figure 64: Side view of FO cable configurations

Note: Top: near plug and heater 3, Bottom: ISS; Black values: Gallery meters (GM). (see table 7-1 ISS for cable meters (CM))

For a proper interpretation of the FO heating data, it is essential to take into account of the FO cable conditions as precisely as possible. In Figure 62, a photographs showing the important features regarding how the FO cable are installed.



Figure 65: Behind the concrete plug

In table 10, FO cable meter values at selected key points are provided. These values are allocated by the DTS unit based on the length of the FO cable and the sampling resolution used.

table 10: Cable meters for Silixa DTS unit at selected points

Tunnel section	Cable running in (m) 00:30 o'clock		Cable running out (m) 11:30 o'clock		Remark
	Start	End	Start	End	
Plug	91.8	97.8	183.5	189.5	Start (or End) position of the cable running out corresponds to End (or Start) position of cable running in.
H3	100.8	105.3	176.0	180.5	
H2	108.3	112.8	168.5	173.0	
H1	115.8	120.3	161.0	165.5	
ISS					
Tunnel Section	Loop-start (m) 04:00 o'clock	Loop-end (m) 03:00 o'clock	Remark		
Gap 2	124.09	132.78	Total length = 8.69 m		
Gap 4	134.89	143.93	Total length = 9.04 m		
Gap 6	146.02	154.80	Total length = 8.78 m		

In Figure 63 and Figure 64, measured temperature profiles along the FO cable at different times are plotted. It is clearly seen that, before the FO cable heating has started, the temperature was about 50 °C, 42 °C and 25 – 30 °C, at the position of the heaters, between the heaters, and shotcretefree interjacent sealing section (ISS), respectively. The FO heating with a power of 1.9 W/m for 1 hour induced a temperature rise of about 4 °C in general, and more at some localized positions.

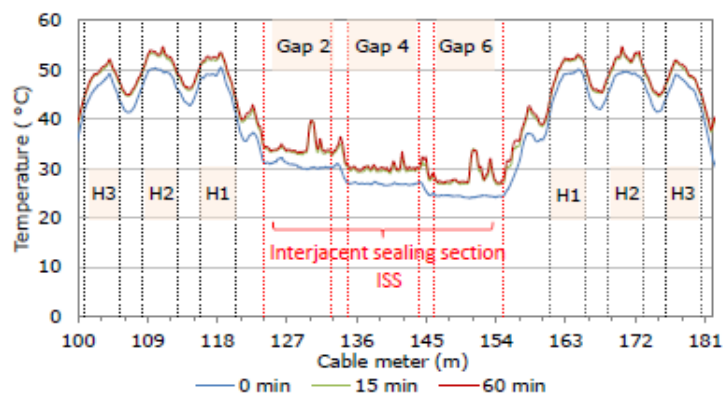


Figure 66: Temperature profiles at different times along the FO cable with 1.9 W/m (two ways, going in and coming out)

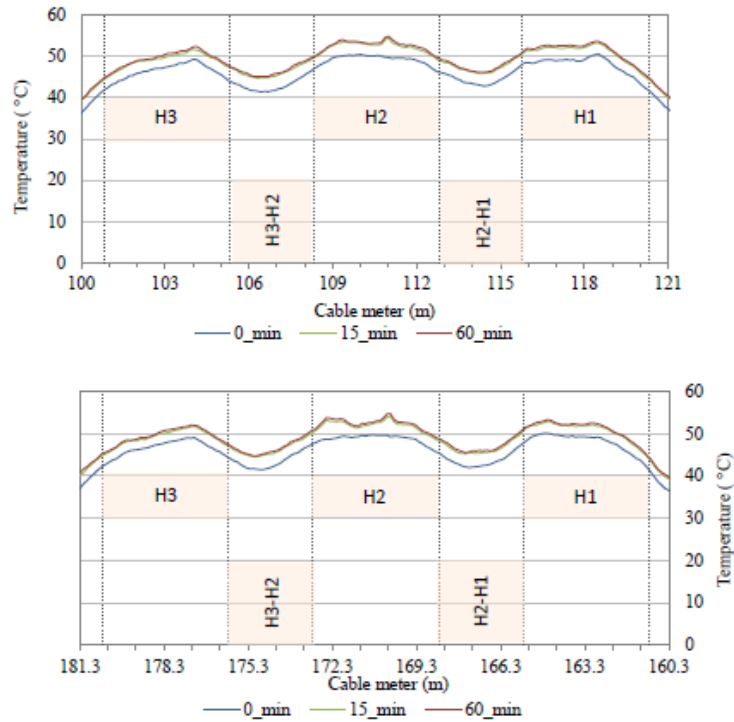


Figure 67: Temperature profiles along the FO cable (one way) at different times

Note: Top: along the 00:30 o'clock position; Bottom: 11:30 o'clock position with CM reversed

Figure 65 shows the temperature changes along the FO cable above the heaters. In general, the temperature rise due to the heating of the FO cable with 1.9 W/m is on the order of 3 °C at 15 minutes after the heating has started. At a couple of localized positions above Heater 2, the temperature rise is distinctly higher suggesting a low thermal conductivity at these locations

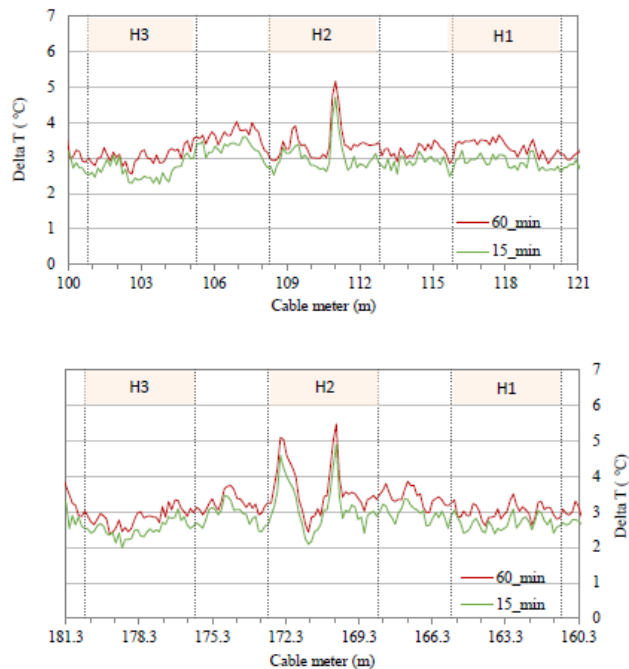


Figure 68 : Temperature changes at different times along the FO cable with 1.9 W/m

Note: Top: in-00:30; Bottom: Out-11:30

Figure 66 shows the temperature changes along the FO cable in ISS. In general, the temperature rise due to the heating of the FO cable with 1.9 W/m is on the order of 3 °C at 15 minutes after the heating has started. At a few of localized positions in the ISS, the temperature rise is distinctly higher. This again suggests that thermal conductivity at these locations is lower.

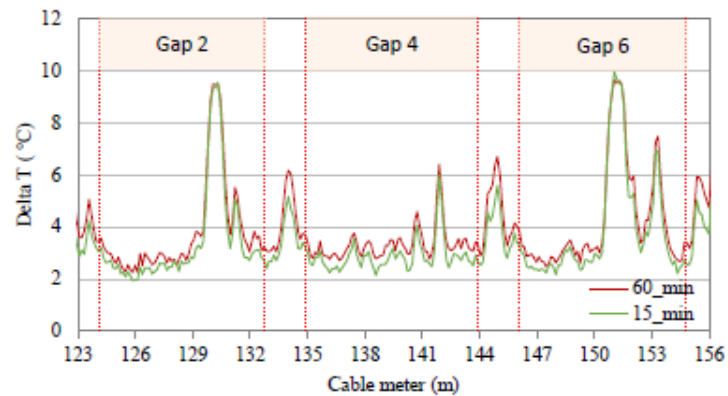


Figure 69: Temperature changes along the FO cable in ISS at different times with 1.9 W/m.

Thermal conductivity estimated using  $dT/\ln t$  data for 3 - 15 min data duration with 1.9 W/m heating (ISS)

Position	Gap 2		Gap 4		Gap 6	
	Cable meter (m)	K (W/mK)	Cable meter (m)	K (W/mK)	Cable meter (m)	K (W/mK)
04:00 – 05:00	124.09 – 124.79	0.449	134.89 – 135.59	0.473	146.02 – 146.72	0.474
05:00 – 06:00	124.79 – 125.49	0.498	135.59 – 136.29	0.508	147.72 – 147.42	0.560
06:00 – 07:00	125.49 – 126.30	0.659	136.29 – 137.28	0.449	147.42 – 148.25	0.614
07:00 – 08:00	126.30 – 127.12	0.588	137.28 – 138.27	0.495	148.25 – 149.09	0.453
08:00 – 09:00	127.12 – 127.93	0.549	138.27 – 139.26	0.469	149.09 – 149.92	0.433
09:00 – 10:00	127.93 – 128.78	0.441	139.26 – 140.07	0.367	149.92 – 150.80	0.232
10:00 – 11:00	128.78 – 129.64	0.310	140.07 – 140.89	0.306	150.80 – 151.68	0.098
11:00 – 12:00	129.64 – 130.49	0.116	140.89 – 141.70	0.410	151.68 – 152.55	0.210
12:00 – 01:00	130.49 – 131.25	0.208	141.70 – 142.44	0.249	152.55 – 153.30	0.214
01:00 – 02:00	131.25 – 132.01	0.334	142.44 – 143.19	0.362	153.30 – 154.05	0.209
02:00 – 03:00	132.01 – 132.78	0.350	143.19 – 143.93	0.462	154.05 – 154.8	0.455

### Summary

The on-site heating experiments for investigating the effect of the shotcrete on the bulk thermal

responses led to the following findings:

- • The thermal conductivity heterogeneity resulting from the shotcrete-GBM interface had negligible effects in cases where the FO cable was 2 and 5 cm away from the shotcrete. For a longer heating/higher heating power, the effect may become visible.
- • When the FO cable was fixed directly (but loosely) on the shotcrete, the effects from the shotcrete started to appear after a certain heating time (roughly 15 – 20 min or longer).
- • Low heating power of 0.5 W/m resulted in more scatter in the estimated thermal conductivity. Higher heating powers of 1 and 2 W/m improved the noise-signal ratio.
- • For the 1 W/m heating (the same power as those currently performed in FE experiment), heating duration of 15 – 20 min seemed optimal without introducing the effects from shotcrete.
- • For the 2 W/m heating, the results indicated that the heating time may be shortened to 10 or 15 min. When such short heating time is used, sampling time may need be shortened in order to have a sufficient number of data points.

### 2.4.7 Summary and conclusion

Application of the heated fiber-optic and DTS (active DTS) to monitor the state of GBM was examined through a series of laboratory tests at the Grimsel Test Site (GTS) and Mont Terri rock laboratory (FMT) in Switzerland. The experimental setting parameters to obtain thermal responses that best reflect the GBM conditions were first identified. It was then followed by calibration of the active DTS tool to the dry density and degree of saturation of the GBM, and evaluation of effects of shotcrete.

The FO cable installed in the FE tunnel at the Mont Terri rock laboratory was then heated with the recommended setting parameters and the temperature responses were closely analyzed to estimate the state of the GBM along the FO cable in the FE tunnel. Finally, the results from the early heating tests in the FE tunnel was interpreted to extract information about the initial dry density at the time of the emplacement.

As summarized below, the active DTS results showed positive insights for estimating the dry density and saturation of the GBM materials.

## 3. Non-invasive techniques:

---

### 3.1 Introduction

Harsh conditions suggest to studying alternative approaches for measurements, for instance methods not based on cables or buses for detecting relevant data. Using cables for data transmission or energy supply can affect the behavior of the engineered barriers. Therefore, cables will be acceptable only where it can be demonstrated that their use will not degrade the long-term waste repository performances.

A possible approach is substituting cables with wireless sensors. But if cables can not be used and the use of wireless techniques is required, new sensors must assure reliable transmission through the isolated areas of a repository without affecting the engineered barriers performance and reliable use of energy supply for the measuring equipment over long periods.

More in general, it is better to enlarge the investigation range to include not only wireless technologies (i.e. EM waves) but also other physical techniques coming from non-EM physical principles, provided that the connection between the detected parameters and the detection system is a non-contact one.

### 3.2 Objectives

The objective is to better understand whether *non-contact techniques* could be a promising solution for measurements in a harsh environment.

In this activity the focus has been given to *monitoring displacements*. The degradation of repository structures along time is one of the critical issues to be continuously monitored. The degradation could give rise to several deformations, e.g. deformation of openings (orientations and apertures, propagation rates) or canister movements. Detecting displacements is the typical measurement method for the monitoring of repository structures and structural stability of openings.

So far, the effective changes in the position of the dummy canisters (heated or not) used in experiments carried out in European URLs were tracked using *contact* type sensors, i.e. extensometers attached to the rock walls at one side and to the canister at the other one. For instance, this was the case for the experiments called FEBEX, PROTOTYPE, or EB (see Figure 67).

Results gathered so far demonstrate that these sensors suffer the mechanical effects of the surrounding buffer plus chemical attack, which derives with time on clear deformation of the mechanical components of the sensing chain and serious damages in the attachments. This makes the measurements not always valid and reliable. Furthermore, as they are punctual measures, the correct tracking of the canister position requires installing several devices to be capable of recording all the possible components of such movements (combination of horizontal and vertical displacements, rotations...). One more successful example so far is the FE-E experiment (see Figure 68).

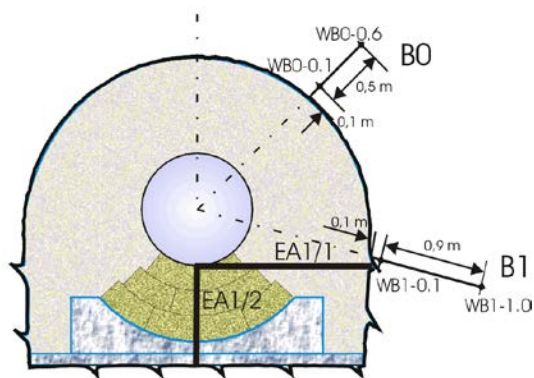


Figure 70. Extensometers (EA1/1 & EA1/2) installed in EB experiment



Figure 71: Extensometers (white pipes) installed in FE experiment

One of the conclusions of the Project was that displacements can become relatively large over time and, if their monitoring is envisioned, then adequate measurement ranges should be considered [107]

It should be noted that the indicated ranges for possible displacements are closely related to several features [107]:

- Elasto-plastic properties of the host rock,
- Design of any structural elements,
- Design and emplacement of backfill, buffer or seal material.

In particular, it was underlined that the ranges of such environmental conditions of interest are depending on the potential monitoring area and specific parameter to consider. For displacement, values rang from 10 mm to 100 mm, being up to 1000 mm for salt rock.

Therefore, the objective of the proposed research is to find alternative measuring methods with respect to the *contact* type sensors to track the position of the future canisters in the Repository, in order to avoid the lack of reliability and to better follow the movements, or to improve the retrievability of the canister by checking the gap between canister and metallic liner.

On the basis of the above-mentioned results, in this work we investigate three different non-contact techniques for monitoring displacements. It should be observed that the presented approaches do not represent all possible approaches. They are only the methods that, to the authors' knowledge and expertise, give some potentialities for the design of realistic sensors for the considered problem. The three possible approaches have been here extensively taken under investigation are the following:

1. Ultrasonic techniques,
2. Gradiometric techniques,
3. Electromagnetic techniques

In general, such investigation seems to naturally start from wireless technologies (i.e. EM waves), even if other physical techniques based on non-EM physical principles can be proposed (e.g. acoustic sensors). The aim of this work is to better understand whether non-contact techniques could be a

### 3.2.1 Reference scenario

In order to focus the problem, a standard test case has been used although other geometries are possible depending on the repository concept and hosting rock. The test case is based on the concept adopted so far by ENRESA and NAGRA for the deposition of nuclear waste in competent clayish rock, which is well represented by the configuration of the already dismantled EB experiment or the recently launched FE experiment, both in Mont Terri URL (Switzerland) [106].



In this case, the future Geological Repository will consist on underground horizontal galleries excavated using a pneumatic hammer or a road header machine (irregular drift surface) where the canisters confining the nuclear waste are disposed off.

An additional isolation method (engineered barrier) is foreseen, based on the combined use of a lower bed made of highly compacted bentonite blocks, and an upper backfill made with a bentonite pellets based material. The geometry of the deposition galleries is horseshoe section, 2.65 m high and 3 m wide for EB or 2.7 m in diameter for FE. The waste canister is 4.5 to 4.6 m long and 97 to 105 cm in diameter. Therefore the distance from the rock walls to the canister surface is approximately 83 to 84 cm (engineered barrier thickness). The location of the canister is relevant because if it moves the thickness of the engineered barrier could be reduced in some parts [106]

The desired measuring device should be capable of tracking the changes in locations of the canister with no contact. The device could be located at the rock walls or in the surrounding buffer material. The accuracy of such measurements should be better than 1 cm. This is of course a very stringent requirement, which will be considered at this stage only a future target. In other words, we started without assuming such a value as a requirement, but as a target value the results of this work will be compared with.

Measurements should not be affected by the expected changes in the buffer (increase of water contents, salinity changes, increase of temperature, increase of mechanical pressure due to the swelling of the bentonite and the elevation of the pore pressures) and by the presence of the radioactive source (the waste) and to the corrosion induced by the media or the potential release of gases. The duration of the measuring solution is expected to be of the order of decades.

To fix the ideas, a sensor network (wired and/or wireless) is installed inside the disposal tunnel. Sensors are buried into the engineered barrier structures, located in non-contact, close proximity with the measured surfaces. Data are transmitted to a Data Acquisition System located in the access tunnel by means of a wired and/or wireless transmission technique in

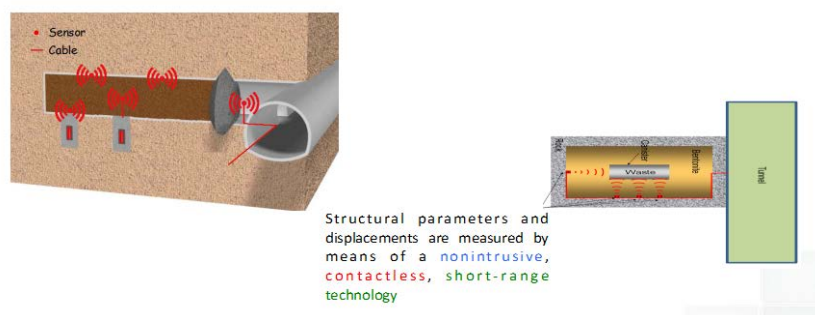


Figure 72 : Schematic of potential implementation of the sensor. (a) Overall view from the tunnel. (b) View inside the hole

The main purposes of the activity is giving a preliminary answer to the following important questions:

- define the best minimal sensor configuration needed for the canister displacement study
- study the optimal (wave) frequencies
- indicate the distances assuring the desired detectable displacement
- propose a concept design for the detection system
- study the response of the system in different operative conditions

In what follows, the proposed investigation is aimed at discussing part or all of these items. It should be observed that in literature there is a wide variety of works giving results that could be potentially useful

for tackle the problem. To the best authors' knowledge, no specific studies are available for the considered problem. All papers found in the literature refer to situations that only vaguely could be associated to the one taken here into account, so that only general considerations can be applicable to the current case study. A comprehensive review of literature is out of the scope of this work. Here, we just focus on three different possible approaches, without exhausting the variety of potential techniques that could be applied to the considered problem.

### 3.2.2 Electromagnetic waves sensor

The proposed methodology is based on a specific application of the well-known GPR technique [116]. for the contactless displacement measurement of a container immersed and suspended in a material with a high degree of water retention. This approach can be considered a classical one.

Even if a specific sensor for the considered problem has not been presented in the literature, several studies in this field could suggest that this approach could be the most applicable to the problem [107][108][109][110][111].

The analytical models and EM characteristics of the waste containment materials are implemented in a simulation model in order to evaluate the instrumental limits of the GPR system in terms of penetration depth and resolution, or the maximum dimensions of the individual constituent parts of the confinement system.

This kind of analysis allows evaluating the response of the medium to an electromagnetic stress as a function of depth and the intrinsic characteristics of the medium (density, viscosity, electromagnetic properties).

Through this analysis, it is therefore possible to evaluate the most appropriate diagnostic method to be used according to the following requirements:

- Topology of the site,
- Type of information that the diagnostic method must acquire (depth of the objects to be detected, electromagnetic and dimensional characteristics of the individual objects to be detected),
- Wavelength of the electromagnetic radiation.

Several diagnostic methods are available in the literature [116][11]. In order to properly understand the propagation properties, it is necessary to study the EM wave propagating in the medium. In the studied case the medium is given by bentonite. Bentonite is a type of clay consisting predominantly of smectite minerals, usually montmorillonite and beidellite. This particular type of material is highly swelling in the presence of moisture, and its large double-layer can be deployed for the retention of cations, toxins, etc. Because of this particular feature, bentonite is widely used for different purposes, such as clarification of wine and beer, or beauty products, confinement of hazardous, nuclear and radioactive wastes, e.g. some bentonite crossapplications with concrete for retention of contaminants in waste solidification/stabilization techniques [106][117].

Most of the studies conducted on the electromagnetic properties of bentonite are concentrated only on the determination of the electrical conductivity change in correspondence of the variation of the chemical composition and the state of hydration [108][110][112].

### 3.2.2.1 Results

In this work, attention has been paid to the possibility of using GPR and NMR techniques to realize a non-contact displacement sensor for monitoring of waste canisters.

As each method must be evaluated in terms of depth of penetration and accuracy of the detected signal, this requires perfectly knowing the dielectric medium crossed by the signal.

In order to do that, a specific characterization of the dielectric parameters should be performed. This is a crucial point. Several works proposed validated models that could be used in the simulations.

It should be underlined that the diagnostic systems based on the propagation of RF waves are limited from the maximum depth of penetration. This in turn is inversely proportional to the AC conductivity of the medium penetrated by the RF wave and therefore inversely proportional to the water concentration of the medium. In the presence of non-negligible water concentrations, it is therefore necessary to reduce the frequency of the RF wave so that it penetrates in the medium and can be detected with sufficient signal-to-noise ratio. In the presence of a medium with a high water content, the spatial resolution limited by diffractive phenomena tends to overall decrease, although in these cases there is a reduction of the RF wavelength as shown by N. Wagner et al. (Figure 2)[127] .

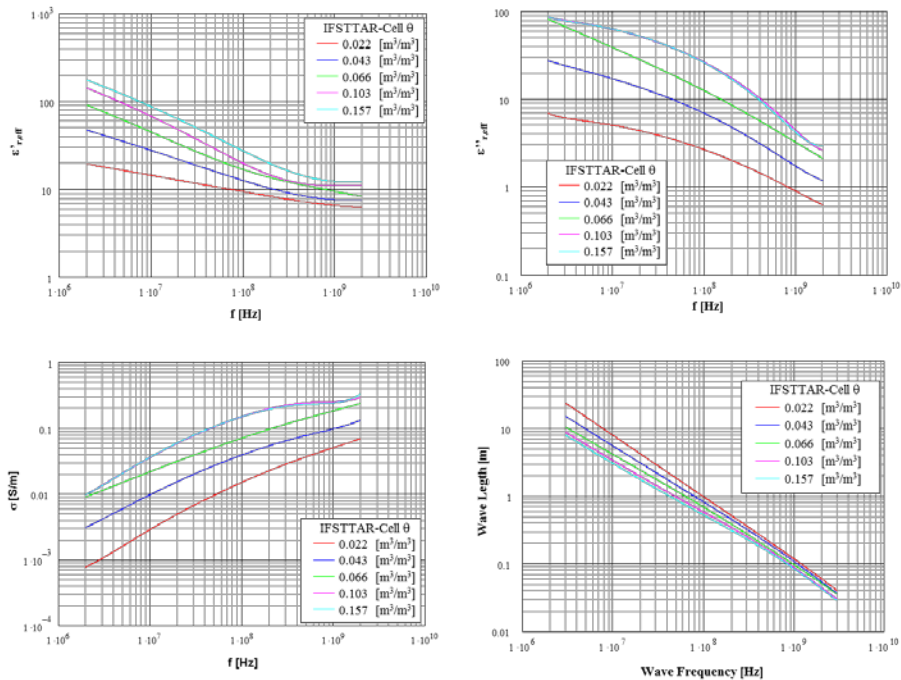


Figure 73: Dielectric, conductivity and wave length spectra of the clay-rock from series 4 (S4) as a function of frequency at different states (results obtained with the IFTTAR cell measured with Anritsu VNA as well as R&S and Agilent PNA).

A summary of literature results for all possible combinations in terms of frequency range, penetration range and diagnostic method have been reported on Table 1.

table 11 : Comparison among different diagnostic methods in terms of all relevant parameters

Frequency Range	Antenna Aperture $D = \frac{\lambda}{4}$	Applicable diagnostic method	Penetration Range	Type of the electromagnetic field Region	Spatial accuracy	Cost	Summary
-----------------	---	------------------------------	-------------------	--	------------------	------	---------

				$d_F = \frac{2D^2}{\lambda}$			
10-100 MHz	Low (7 - 0.7 m)	RMN tomography	Good (1-10m)	Near field	Good (0.1-1 mm)	High	Good system performance both in terms of detail and property of the detected objects; high infrastructure costs
100 - 1000 MHz	Medium (0.7 - 0.07 m)	GPR	Medium, Low (0.1-1m)	Near field Far Field	Medium (1-10cm)	Medium	Poor system performance both in terms of details and properties of detected objects; medium infrastructure costs
1 - 10 GHz	Good (7-0.7cm)	GPR	Low, Very Low (0.1-10cm)	Far Field	Good (0.1-1cm)	Medium High	Low and very bad system performance with high infrastructure costs

The table has been compiled evaluating for each frequency range the most convenient diagnostic method in terms of the spatial and / or temporal resolution, peculiarity of the method and limits of applicability. It should be observed that the considerations that made it possible to fill in Table 1 are rather general or do not take into account the fact that the boundary conditions of the scenario can be well defined and immutable over time.

Therefore, by appropriately choosing the frequency range of the electromagnetic field according to the geometric configuration of the repository where the canister is stored, even in the presence of dissipative medium (non-negligible medium conductivity), it is plausible that some auto-resonant modes can be detected with sufficient reliability by the receptive devices.

This allows to detect canister displacements even below the limit resolution due to diffractive phenomena. In order to give a preliminary answers to the considered problem, i.e. the evaluation of the displacement for a canister in a geological disposal, we should define the specific environment from an EM point of view. This allows simulating the propagation field inside the considered materials. In Figure

3 the scenario used for the EM simulation is presented. Assuming to use a chirp signal as an excitation signal, the signal detected by the sensor will be modulated in amplitude and phase according to the geometrical characteristics of the scenario in which the electromagnetic field propagates.

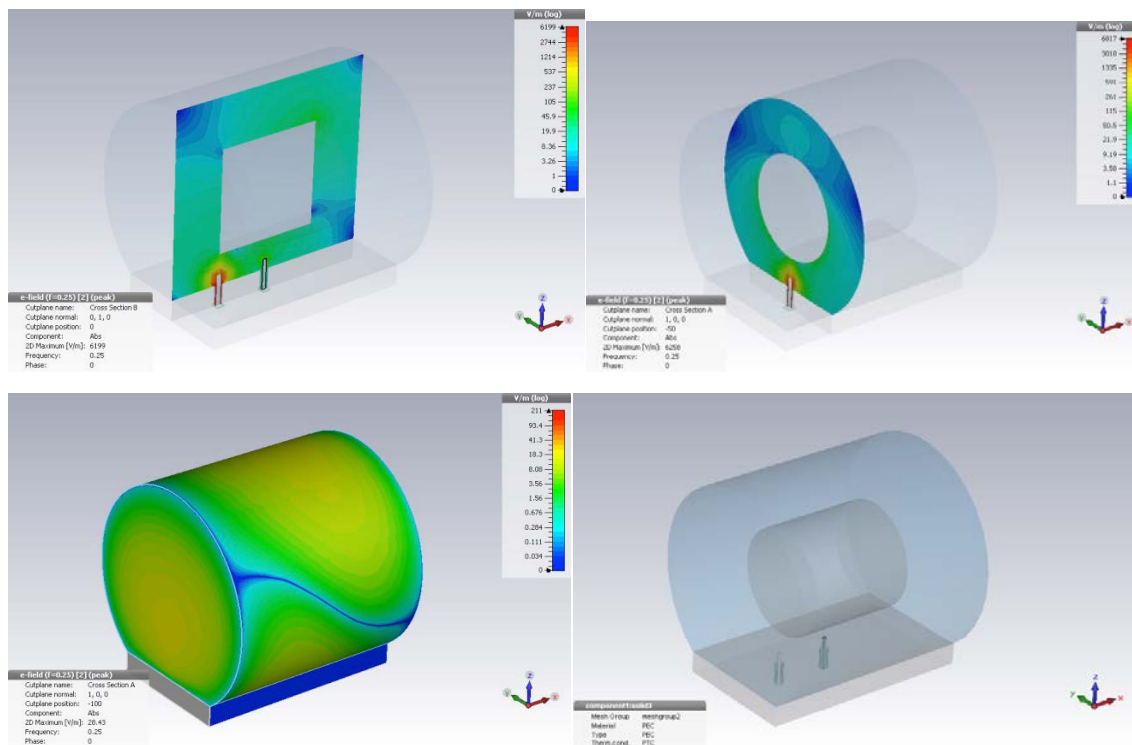


Figure 74 : Simulation scenario in a reduced scale for a canister where a propagating EM field is generated by one dipole antenna

In fact, the amplitude spectrum of the detected signal will show one or more Lorentzian-type patterns centered within the resonant modes peculiar of the chosen geometric configuration in which the field propagates (Figure 4).

However, the greater the conductivity of the irradiated medium and the water concentration, the greater the bandwidth of these resonances.

Instead, the spectrum of the phase derivative of the detected signal will show relative maxima at the frequencies of the resonant modes. These maxima will decrease in amplitude as the concentration of water in the medium increases.

A modal analysis of the reflected signal, when the position of one of the objects changes, will allow to detect variations in amplitude and phase that in principle are linked to the object deviation. The resolution depends here on the factor of merit of the analyzed resonant mode, which in turn is inversely proportional to the water concentration of the medium.

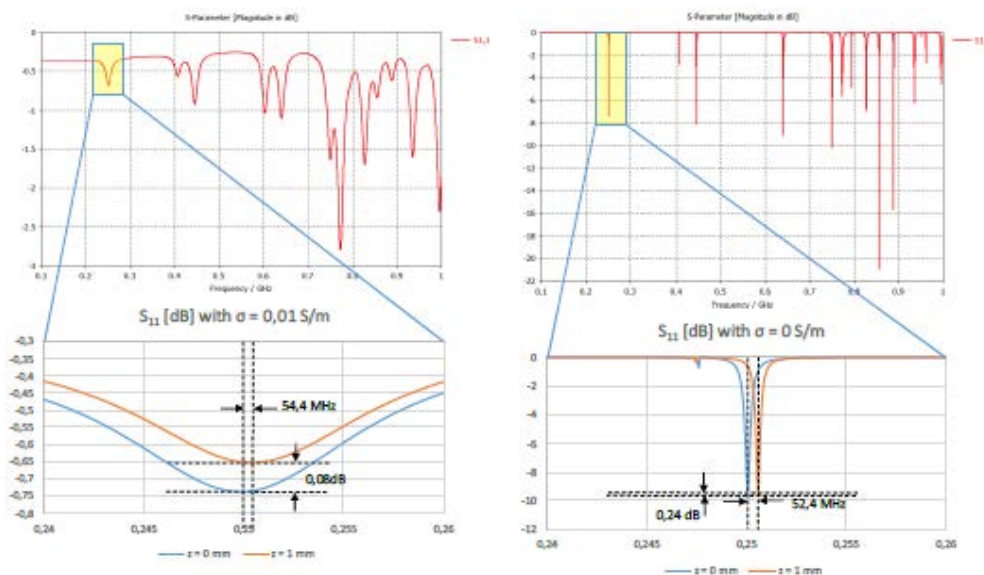


Figure 75: Reflecting coefficient (S11 [dB]) for the scenario presented in Figure 69

The linearity of the phase shift with the displacement of the analyzed object and the corresponding sensitivity requires a preliminary analytical and numerical study of the scenario

### 3.2.3 Gradiometric Sensor

A completely new approach here presented by the authors for the first time could be based on the following idea: each object to be monitored produces a small but not completely negligible gravitational field produced by its mass distribution. Given a mass density distribution  $\rho(\vec{x})$  describing the mass contained in each element of the object being monitored, a gravitational potential is produced, given by

$$V(\vec{x}) = \int \frac{\rho(\vec{x}')}{|\vec{x} - \vec{x}'|} d^3x'$$

The integral is extended to the overall mass being monitored. This potential can be used to obtain various derived quantities, notably the gravitational force acting on whatever another object outside the first.

An experimental procedure able to measure some of these derived quantities provides information on the potential  $V(\vec{x})$  and therefore on the mass distribution generating it. Two types of measurement could be performed:

1. a **gravimetric** one;
2. a **gradiometric** one.

The first implies a measurement of the gravitational field in selected spatial positions outside the body (unit of measurement: Gal); the second a measurement of the field gradient ('difference') between couples of closely spaced points (unit of measurement: Eötvös).

An important difference between the two quantities is that (considering for simplicity a spherical mass distribution) the first scales as  $r^{-2}$ , while the second scales as  $r^{-3}$ ,  $r$  being the distance between the sensor and the mass. Therefore, proximity to the mass being studied is an important factor to be considered, in order to obtain a sufficiently high signal-to-noise ratio. This should not be a significant concern for the present proposal, but it could require a further assessment in case of a realistic implementation.

The key point is that in principle a given motion of the object being monitored would produce a gravitational signal that could be measured by the gravimeter or gradiometer. It has to be underlined that the inverse problem one wants to solve (determining the mass distribution given the gravitational field it produces) does not admit a unique solution, as it is well known in geodesy and geophysics. Therefore, any experimental measurement campaign will have to be complemented by a model (be it analytical or numeric) of the object, in such a way to create a set of ‘templates’ necessary to ‘deconvolve’ the signal and extract the quantities of interest (e.g., the motion of the object). The importance of this analysis phase does not have to be underestimated.

An important advantage of the gradiometric technique with respect to the gravimetric one is that the first – by construction – relies on the difference between two closely spaced measurements. Therefore, any disturbance external to the system (so-called ‘common mode’) would be largely cancelled, thereby greatly suppressing the corresponding systematic contribution in the measurement error budget.

### 3.2.3.1 Design of a possible gradiometric sensor

The **objective** of the design is to provide a first prototype of a gradiometric sensor for displacement monitoring of a canister in an EBS. This proposal can be divided into two phases:

1. **Design phase:** this preliminary phase is necessary in order to design the sensor and carry out a series of measurements for:
  - characterizing the sensor
  - calibrating the sensor
  - testing the sensor with a filled cylinder
2. **Prototyping phase:** in the second phase, a first prototype should be designed and customized in order to be inserted in a borehole on the basis of the results obtained in the previous phase (design phase).

#### Experimental setup

Two different types of sensors can be designed and proposed for the detection of the displacement as in Figure 11. The first sensor is composed by two accelerometers in a differential configuration (sensing mass 1 and sensing mass 2) so to give a measure of the horizontal component. The second differential sensor is used for measuring the vertical component. While the first sensor is used in parallel to the cross-section of the canister, the second sensor will be inserted in the borehole and used as a moving sensor on a carriage inside the borehole.

Using two sensors allows studying both displacement directions in a more feasible way, thus improving the reliability of results.

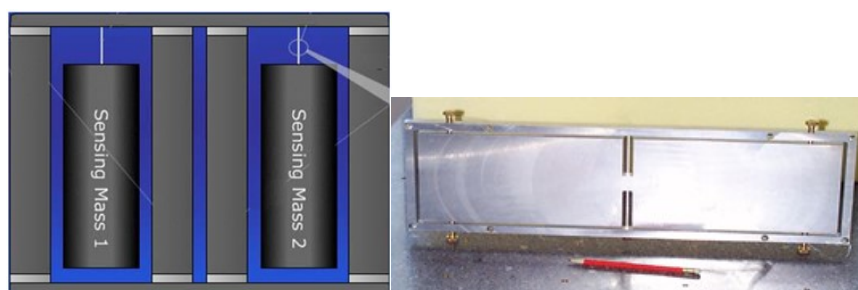


Figure 76: Schematic of potential implementation of the sensor

#### Key results

In order to arrive to a first prototyping, the following procedure could be followed:

- Development and realization of a first prototype ready to be installed in a hosting geological laboratory
- Validation of a Data Acquisition System with a defined accuracy
- Definition of physical limitations of the proposed technology
- Definition of an effective data analysis procedure
- Realization of an experimental campaign in situ for testing the prototype and obtaining first experimental results (this part is to be defined, and is not included in the budget below)

This approach as been here proposed as a general approach, details being covered by an ENEA patent.

### 3.2.4 Ultrasonic waves sensor

For the considered case study, the radioactive canister can be allocated in a cavity and placed horizontally or vertically. The space between the canister and the cavity is then filled with bentonite. The position of the canister must remain unchanged over time and monitored in all directions XYZ. For this purpose, non-destructive techniques can be used that detect the position without being in contact with the radioactive canister. In the case of application of foundation piles, the control is carried out by means of ultrasound probes inserted in the channels created during the casting of Crosshole Sonic Logging (CSL) in the same pole. In the case of the canister, these channels will be created in the bentonite or on the sides of the cavity. The ultrasound probes (20 - 50 KHz) can transmit or receive the waves in a timed manner, for example on 4 positions (Figure 8). The waves propagating from a transmitting probe in the bentonite/rock will invest the canister, which in turn will take the wave in different directions, that is eventually received by the 3 receiving probes. The process sees a transmitter probe and 3 receivers in alternating way, which rotates their role at each cycle. Each cycle will have 3 different signals for the 3 receiving probes, i.e. for 12 cycles become 12 different signals.

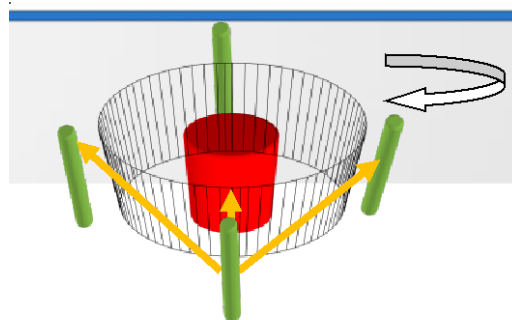


Figure 77. Ultrasound Sensor Scheme

The channels will have a certain length  $Y$  in which the probes run through (for example at every cm), and the probes emit and receive the corresponding 12 signals. After this scan, a mapping along the whole length of the cavity is obtained, and as a result of both the canister and the bentonite. This mapping is represented by a series of slices or morphological profiles that must remain unchanged over time. For this reason the technique can be called non-destructive monitoring or structural health monitoring.

#### Cross-Hole Analyzer CHAMP-XV (by Pile Dynamics, Inc)

There exist some commercial devices that are commonly used for concrete monitoring as non destructive techniques. Currently, Cross-Hole Sonic Logging (CSL) offers the most reliable technique for assessing the integrity of in-place constructed deep foundation elements. CSL is a common testing methods for determining the integrity of in-place constructed deep foundation elements, such as drilled shafts and



caissons. A minor variation of this method, called Single-Hole Sonic Logging (SSL) can also be used on smaller diameter drilled mini-piles. The methods differ only in the number of tests per pile and the location/orientation of the transducers within the pile. Pros and cons depend on the specific application. The Cross-Hole Analyzer [9] evaluates the quality of the concrete of deep foundations by the Crosshole Sonic Logging (CSL) method. It also performs Single Hole Sonic Logging (SSL).

Drilled shafts and other cast-in-place concrete foundations are prepared for the test by installation of PVC or steel tubes during their construction. During the test, a transmitter is lowered down in one of the tubes and sends a high frequency signal to a receiver inserted in another tube. Transmitter and receiver move down each pair of tubes, scanning the entire length of the shaft. Cables for the receiver and transmitter are available in various lengths, and may each be positioned at different depth levels for maximum testing flexibility.

Shafts that will be tested with a Cross-Hole Analyzer are built with steel (preferred for CSL) or PVC (required for SSL) tubes that span their length. A transmitter in one tube sends a high frequency signal that travels through the concrete and is detected by a receiver in another tube (or in the same tube for SSL). As these sensors are raised and/or lowered along the length of the foundation, the Cross-Hole Analyzer displays and records the strength of the received signal, as well as the time from signal emission to signal arrival at the receiver versus depth. In CSL, scanning various tube combinations for the entire shaft allows evaluation of concrete quality and defect location along the length and by quadrant. Only one tube is used in SSL. The optional Motorized Probe Deployment System relieves the operator from pulling the cables manually, making testing more comfortable (Figure 9).

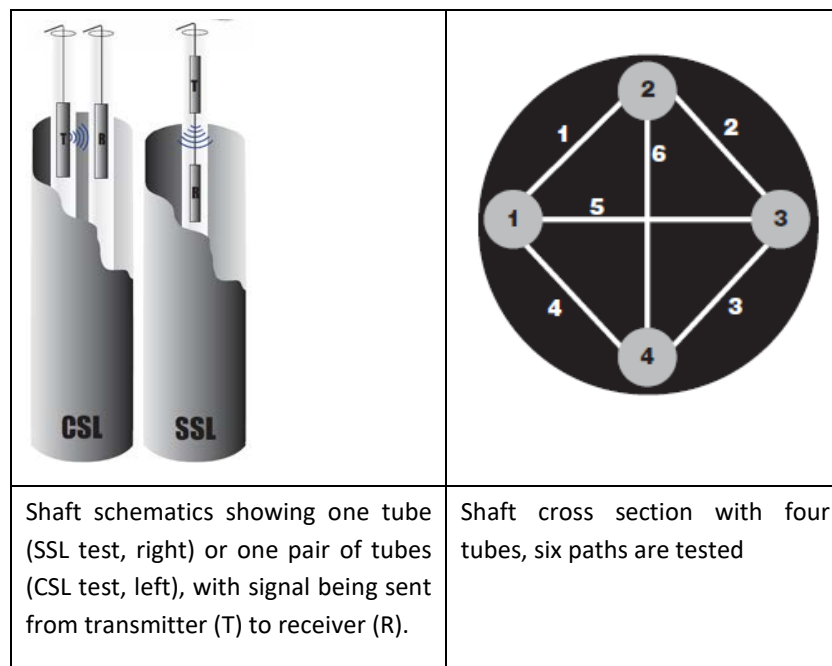


Figure 78. Shaft schematics and cross section

The commercial tool includes a Data Processing Software, which provides powerful tools for data analysis (Edge Finder for First Arrival Time detection, Defect Analysis for easy defect identification, ...). The probes have these specifications:

Physical specifications	Electronic specifications
Diameter: 25 mm Length: 215 mm	Transmitter frequency (nominal): 45 kHz
Element: Ceramic	Receiver tuned to 45 KHz nominal
Enclosure: Oil Filled Nickel Plated Brass	Transmitter voltage: 200, 400, 600 or 800 Volts (user selectable)
Shells pressure tested to 300m water depth	Powered by 12 V source in the CHAMP-XV (for safety)
Optional centralizers and bottom extension weights for deeper shafts.	Maximum probe separation: 3 m
Probe Cable: 60 m, 100 m or 150 m, heavy duty polyurethane jacket	

The tool also includes tomography software for Crosshole Sonic Logging (CSL) data. Tomography is a mathematical procedure that is applied to Crosshole Sonic Logging (CSL) data, providing the user with a visual image of a shaft’s internal defects. The procedure is aimed at solving a system of equations based on First Arrival Times (FAT) in order to calculate wave speeds at various points within the shaft. Tomography wave speeds distributed throughout the shaft are directly proportional to density, indicating material quality.

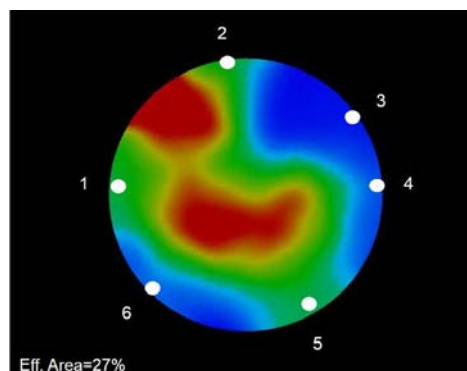


Figure 79. Wave speed contours at a cross-section depth of 1.34 m

In conclusion, a possibility of further implementing a sensor using ultrasonic techniques has given. The method is very simple, based on COTS instrumentation and not expensive. A possible drawback is the insertion of water on the inspection channels. A proper experimental campaign must be considered in order to practically assess the results of such an approach for the considered case.

### 3.2.4.1 Conclusion

Preliminary results indicate that all approaches could be suitable to solve the studied problem, yet several technical issues are to be faced before defining the best solution, which will be the result of a trade off among accuracy, depth of penetration and complexity of the detection system.

In this report we have analysed three different approaches to the problem based on three different physical principles: ultrasound waves, EM waves, gravity.

It is not possible here to give a direct comparison among them in terms of pros and cons, because the maturity level of the correspondent technology has not here considered, being well beyond the scope and the objectives of this work.

The objective of this activity has been to understand potential approaches to the individuation of alternatives to cable or contact existing technologies.

We have here individuated three different physical choices. Not all have been investigated until the final definition of a sensor, because even arriving to a real study of feasibility imposes the realization of experiments and tests that require the availability of significant resources.

The aim of this work has been an overview based both on the literature and on some original studies conducted by the authors, in order to explore potential applications that could deserve more attention in the future also thanks to the results contained in this report.

The ultrasound waves technique can be considered a mature technique already used in several applications for similar purposes. But in order to arrive to a real study of feasibility on the realization of a contactless sensor to be used for displacements measurement, more effort is required in order to design and test a prototype in a realistic application. The scheme here presented can be considered as a hint to start with.

On the other hand, the gradiometric technique here proposed should be considered at this stage as a pure conceptual proposal, yet a very promising one. It requires a strong effort to be transformed in a realistic prototype. The technique seems to show several advantages:

- Measures are also possible through a material discontinuity or vacuum
- Measures are also possible through metallic shielding
- Possible Hard Rad-Hard version (with remote electronics) up to 100Krad
- Easy to calibrate

Nevertheless, several issues should be fixed, first of all the interference effects with other (natural or artificial) massive systems.

More attention has been paid here to the third approach, i.e. *EM waves*. This possibility has been widely considered both on the theoretical and the simulation point of view. Some considerations could then be given as a conclusion of the work.

The GPR and NMR methods have been considered. Each method must be evaluated in terms of *depth of penetration* and *accuracy* of the detected signal. This requires to perfectly knowing the dielectric medium the signal passes through. In order to do that, a specific characterization of the dielectric parameters should be performed. This is a crucial point. Several works proposed validated models that could be used in the simulations.

It should be underlined that the diagnostic systems based on the propagation of RF waves are limited from the maximum depth of penetration. This in turn is inversely proportional to the AC conductivity of the medium penetrated by the RF wave and therefore inversely proportional to the water concentration of the medium. In the presence of non-negligible water concentrations, it is therefore necessary to reduce the frequency of the RF wave so that it penetrates in the medium and can be detected with sufficient signal-to-noise ratio. In this way, however, the spatial resolution (limited by diffractive phenomena), tends

to compressively decrease, despite the length of the RF wave being compressed in the presence of media with a higher water content, as shown in figure 12.

On the other hand, the use of well-defined topological configurations that allow the propagation of stationary electromagnetic waves and the knowledge of the electromagnetic properties of the materials involved, enhances the spatial resolutions below the diffractive limits. In this case, although the medium in which the electromagnetic field propagates is dissipative, by choosing wavelengths of at least one order of magnitude less than the geometric dimensions of the considered scenario, a series of resonant modes can be established (geometrically overmodal structure).

However, the presence of water concentrations will not allow to obtain resonant modes with high factors of merit. Therefore, the frequency spectrum of the reflected signal will have a finite band. Yet, the frequency band is not very narrow with an approximately linear phase drift around the central frequency (if the modes have central frequencies sufficiently distant from each other). A modal analysis of the reflected signal, when the position of one of the objects changes, will allow to detect variations in amplitude and phase that in principle are linked to the object deviation. The resolution depends here on the factor of merit of the analyzed resonant mode, which in turn is inversely proportional to the water concentration of the medium. The linearity of the phase shift with the displacement of the analyzed object and the corresponding sensitivity require a preliminary analytical and numerical study of the scenario.

Preliminary simulation results presented in this work confirm that as the frequency increases, the depth of penetration tends to dramatically reduce. But decreasing the frequency means that a higher antenna should be used. As a consequence, the design of the sensor should be done by a trade off between accuracy and geometrical dimension of the sensor (that should be designed so as to be easily included in the proposed environment). All possible combinations in terms of frequency range have been reported on Table 3. A detailed design could be done only after a thorough experimental campaign. The presented table could be used as a basic reference guide to start with.



## 4. Chemical sensors

### 4.1 Improvements and new developments on chemical measurements

#### 4.1.1 Introduction

Many safety relevant functions required for the compacted bentonite buffer in the final disposal of spent fuel rely on processes influenced by chemical composition of the pore water in bentonite. Important safety relevant processes are, inter alia, swelling, alteration, precipitation and dissolution reactions, transport of water colloids and ions.

The bentonite consists mainly of montmorillonite, smaller amounts of accessory minerals and pore water. The pore water can be divided into interlamellar water (IL-water) and non-IL water [142][138][134][133][146][129]. The compositions of the two types of pore water vary due to the negatively charged surfaces in montmorillonite. IL-water layers of less than a few nanometers are affected by anion exclusion phenomenon, whereas in larger non-IL water volumes cations and anions are present in varying amounts, depending on the distance from the negatively charged clay surfaces [145][139][143]. (Figure 77.)

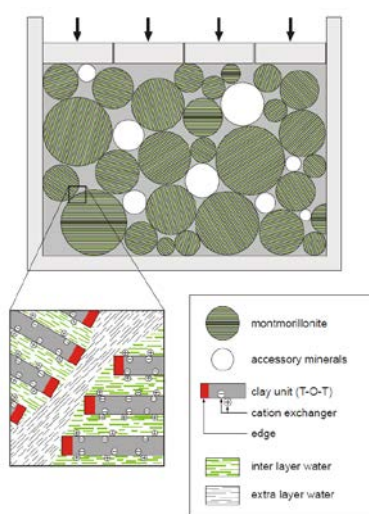


Figure 80. Generalized microstructure of (MX-80) bentonite [146] Extra layer water as non-IL water.

Activity, the effective concentration of a species in solution, should be used in non-ideal solution due to the interactions of ions between each other. Ion activity depends on the surrounding conditions, such as temperature, pressure, ionic strength, ion composition, etc... When these variables change also the ion activity of different species will change in solution [128] (Appelo and Postma, 1993). The majority of experimental data on the composition of compacted bentonite is based on batch experiments by leaching or using squeezing methods to collect pore water. In these methods pore water is removed from its initial surrounding and analyzed. However, there are certain uncertainties in those methods. Dissolution of accessory minerals, cation exchange reactions, mixing of different pore water types and interaction of charged surfaces will cause changes in the ion activities. Geochemical modelling has also been used to study composition of the pore water, but the uncertainties in data obtained experimentally will influence the modelling as well. However, much has been learnt during years and the pore water

composition of bentonite can be evaluated, if not strictly quantitatively, at least semi-quantitatively by combining results of different studies [132][141][137][130][129]

Direct measurement of ion activities in pore water of compacted bentonite are exceedingly difficult to perform because of the huge swelling pressure, which most of the sensors cannot withstand, also the low amount of the free water available for the sensors and long measuring times. VTT has developed a methodology for measuring pH and Eh in compacted bentonite. The aim of this study is to broaden the method of in-situ measuring relevant ion activities in the pore water of compacted bentonite. In this study commercial and house-made Ag/AgCl Cl-sensitive electrodes and Na sensitive “Nasicon” electrode with solution filling are tested in batch experiments, as well, H<sup>+</sup> sensitive IrOx electrode in diffusion experiment.

#### 4.1.2 Description of the technology

The ion selective electrodes used in this study are based on measurement of electrical potential difference between an ion selective electrode and a reference electrode. In an ideal situation the reference electrode is independent of the solution composition and the membrane of the ion selective electrode will be selective only for one specie. The reference electrode will give constant potential and the potential of the ion selective electrode will change with changing chemical activity of the measured ion in a solution according to Nernst equation (1). Where,  $E$  is the measured potential,  $E_0$  the constant value measured according to arrangement,  $R$  is the gas constant,  $T$  is absolute temperature,  $z$  is the charge of the ion,  $F$  is the Faraday constant and  $a$  is the activity of the ion in the solution [133].

$$E =$$

*Schematic presentation and photoelectrode is presented in Figure x. ctric contact between the membrane an the elect*

$$E = E_0 + \frac{2.303RT}{zF} \log a \quad (1)$$

Measurement is performed by placing pre-calibrated ion-selective electrodes in the holes bored in the compacted bentonite samples. Bentonite is then slightly compacted in order to obtain a good contact between bentonite and the electrode. The potential difference between the ion-selective electrode and an external reference electrode is measured by a voltmeter. The reference electrode is in contact with bentonite via solution ( Figure 78). At the end of the measurement the ion-selective electrode and the reference electrode are calibrated again. The ion activity is calculated according to the calibration curve obtained.

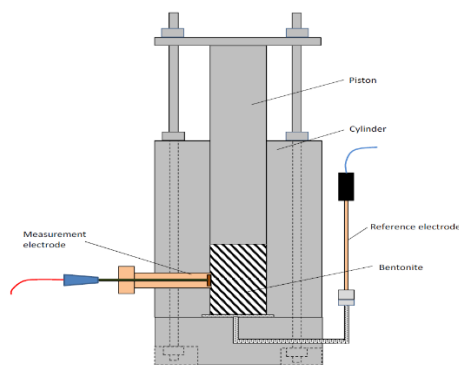


Figure 81. Schematic presentation of the test bench for ion-selective electrode batch testing. [140]

### 4.1.3 Preparation of the samples

Bentonite consists of montmorillonite and accessory minerals and both have an effect on the composition of porewater. Thus, bentonite has to be purified from accessory minerals and dissolved ions, e.g. chloride, if certain ion activities are to be measured. An example of initial chloride concentration effect on Cl activities in compacted bentonite samples can be seen in Figure 3.

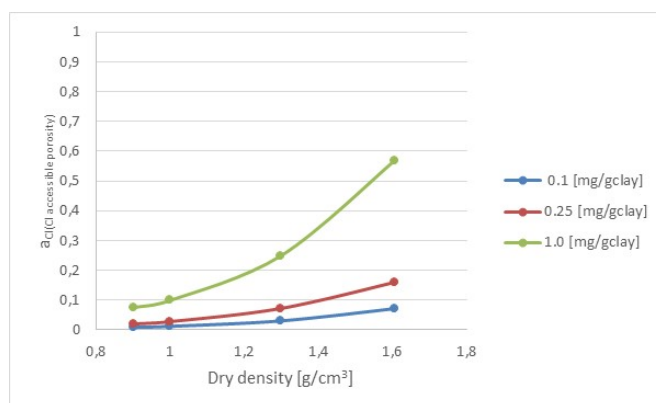


Figure 82. Bentonite initial Cl content effect on Cl activity in compacted samples when Cl accessible porosity is taken into account (Muurinen & Carlsson, 2013). The chloride activities were calculated based on the species in the Thermoddem database when using the *PHREEQC* code.

The method described in [144] was followed to purify the MX-80 bentonite at VTT. The purification consists of removal of the large particles, dissolution of carbonates by acid treatment, dissolution of iron oxides, removal of organic material, changing to the sodium or calcium form, and removal of the excess salt by washing and finally by dialysis. Photos of purified samples are shown in Figure 80. The unpurified MX-80 samples were used for testing chloride sensitive electrodes in batch experiments. Na-montmorillonite purified from commercially available MX-80 bentonite in tests with liquid-filled Na-sensitive electrodes was used. Diffusion experiment to measure pH changes in bentonite was performed using MX-80.



Figure 83. Purified Ca-montmorillonite on the left, MX-80 and grinded Na- and Ca-montmorillonites purified from MX-80 on the right.

#### 4.1.4 Compacting of the samples

Two different procedures were tested for preparing samples. In the first case bentonite powder were mixed with salt solution of composition of studied salt concentrations (0.01, 0.1 and 1.0 M NaCl). Then mixtures were compacted at the target dry densities. In the second case bentonite powder was mixed with deionized water. Then mixture were compressed in diffusion or squeezing cells at the target dry density and were left for wetting first with deionized water for a month to guarantee fully saturated state of the sample. The external saturation solution was changed to studied solution (e.g. 0.5M NaCl) and external water was allowed to equilibrated with studied sample by diffusion. In both cases the amount of liquid was calculated so that the samples reach fully saturated state at the target dry density. The picture of wetting samples can be seen in Figure 81. The problems of preparation of the samples by mixing bentonite and studied solution without diffusion can be seen in Table I and Figure 10 in results.



Figure 84. Diffusion cells for wetting compacted bentonite samples. On the right diffusion cell where external water sources are below and above of stainless steel sample holder. Liquid is separated from bentonite sample by sinters.

#### 4.1.5 Electrodes

House-made electrodes (e.g. pH and Na) were prepared according to methods described in [147], [138] [131] Commercially available reference and chloride electrodes were modified to be suitable for test-bench. Some house-made and modified electrodes are presented in Figure 82.



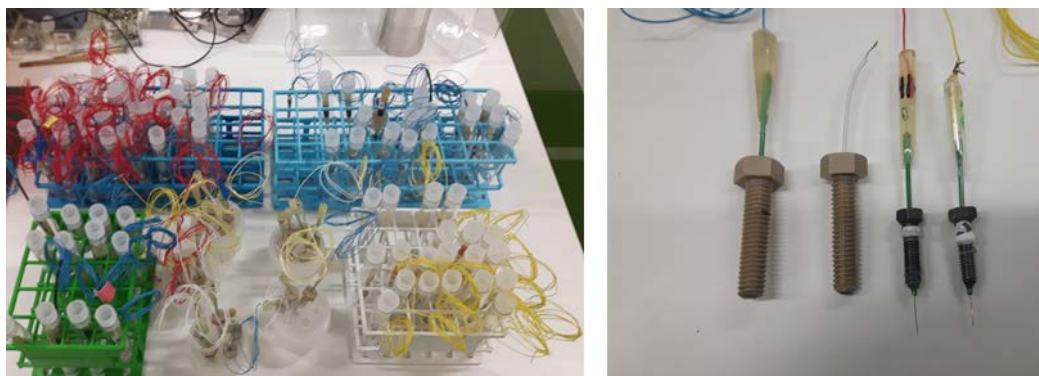


Figure 85. On the right side house-made liquid filled Na-sensitive Nasicon and pH sensitive IrOx electrodes. On the left electrodes ready for experiments.

- Cl selective electrode

The chloride electrodes were made in-house at VTT by dipping a silver wire in molten AgCl and was used in experiments where samples were equilibrated by mixing. The commercial Ag-AgCl coated silver wires prepared from a fine-grain homogeneous mixture of silver and silver chloride (In Vivo Metric, Healdsburg, California, USA) was used in experiment where samples were equilibrated by diffusion. The coated wires are 1 mm in diameter and 2.5 mm in height with 10 mm silver wire. The silver wire was first soldered to a 7 cm long electric wire and placed into a PEEK tube in a PEEK screw. The PEEK tube was then filled with epoxy so that also the bottom of the Ag-AgCl pellet was fixed into the PEEK screw. When the epoxy was hardened, the slot between the sides of the PEEK tube and the screw was filled with epoxy. A longer electric wire was soldered to the electrode and the joint was supported with epoxy.

- pH electrode

Solid iridium oxide (IrOx) pH electrodes was prepared by high-temperature oxidation method [147](Yao et al. 2001) in which an iridium oxide film is formed on iridium metal wire in lithium carbonate melt. The pH electrodes were prepared in the following way: Ir metal wires (0.15 mm diameter, 99.9% purity, from Aldrich Chemical Company) of about 50 mm in length was cleaned first with 6 M HCl and then with deionized water. The wires were placed in a gold crucible filled with Li<sub>2</sub>CO<sub>3</sub> powder. The oxidation of the Ir wires were performed at 870°C for 5 h in a furnace under air atmosphere. After cooling down to room temperature, the solid carbonate in the crucible was dissolved with hydrochloric acid. The oxidized wires were then washed with deionized water to remove any attached soluble components. Finally, the wires were dried at 120°C overnight. As a result, a black oxide layer grew on the surface of the wire. In order to fabricate the pH electrode, a 10 mm long section of the oxidized wire were scraped clean and a connecting wire for the data logger was soldered to this bare end. The whole electrode, except the 7-10 mm long sensor part, was covered with a protective PEEK tube filled with epoxy glue and the soldering supported with a tube filled with epoxy glue.

- Reference electrode

The reference electrode used was a commercially available Ag/AgCl electrode (LF-2) from Innovative Instruments, Inc., USA. The filling electrolyte is 3.4 M KCl. The electrode body is constructed from PEEK. The electric contact of reference electrode with the bentonite could be established through water in contact with the compacted sample through a sinter. Due to shifting of the potential, the electrode have to be checked frequently.

- Na electrode with liquid filling

The aim of this part of the study was to find out if liquid filling as a conductor between membrane and conduction wire will improve stability of electrodes. Soldering was replaced by NaCl solution and Ag/AgCl electrode were used as inner reference electrode (Figure 7). A Sodium Super Ionic Conductor (Nasicon) pellet was used for the membrane of the sodium electrode [131]. The Nasicon powder was pressed for two hours at 4000 bars at 200°C and sintered in an oven at 1000°C. The membrane was fixed with epoxy to the electrode body and the electric contact between the membrane and the electric wire in the electrode was made with NaCl solution. The schematic presentation of liquid filled Na-electrode is presented in Figure 83.

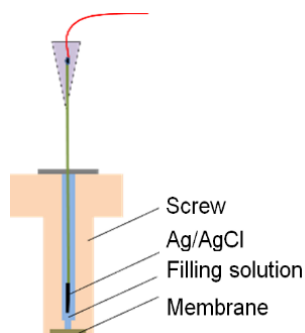


Figure 86. Schematic presentation of the liquid filled ion selective electrode.

#### 4.1.6 Test benches

Two kind of test benches were used for experiments. Modified squeezing cells (Figure 84) for batch experiments with Na and Cl sensitive electrodes and larger diffusion cells (Figure 86) for study H<sup>+</sup> diffusion in MX-80.

##### Batch benches



Figure 87. Test bench for batch experiments.

The test bench, modified from squeezing cells were used for batch experiments to study porewater ion activities by ion-selective electrodes. The test bench consists of a piston, a cylindrical sample holder, a sinter and a bottom part, all made of titanium. The bottom part contains a tube that acts as an outlet for the squeezed porewater. The tube, which is filled with squeezed porewater once the squeezing has started, also establishes the necessary electrical contact between the measuring electrodes and the reference electrode. The electrode holes in the cylinder wall are closed with bolts during compaction. When the electrode is placed, the bolt is first removed and a hole of about 1 mm of the diameter is made in the bentonite for the sensor. The sensor part of the electrode is placed so that it is fully surrounded by the bentonite. Finally bentonite is gently compacted in order to get a good contact between the electrode and bentonite. [138] (

## Diffusion bench

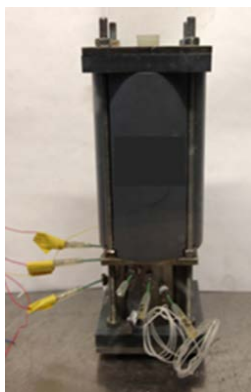


Figure 88. Photo of the diffusion cell. The diameter of the bentonite sample is 40 mm and the height 50 mm. The electrodes are 5, 10 mm from the solution-bentonite interface. The volume of the solution in the external vessel is 230 ml.

The diffusion cell ( Figure 85) is aimed to study the interaction between an external solution and bentonite. The cell consists of a titanium tube for compacted bentonite and a vessel made of PVC for the external solution. The contact between the bentonite and the solution is via a titanium filter plate. The titanium tube has holes for three pH electrodes at distances of 5, 10 and 20 mm from the bentonite-solution interface. During measurement periods, the reference electrode is placed in the external solution through a hole made in the stopper closing the solution vessel.

### 4.1.7 Results

- Experiments with Cl selective electrodes

Chloride activities were studied in compacted MX-80 samples equilibrated with NaCl solution by diffusion or mixing method. House-made and commercial Ag/AgCl electrodes were used to measure Cl activities. Chloride content in samples was analysed by aqueous leaching method, where 0.3 g of dry bentonite were dissolved in 30 mL of deionized water, centrifuged, ultrafiltered and analysed by IC (ion chromatography).

Chloride activity was calculated using the analysed amount of Cl in sample [mg/gclay], water content measurements of sample and modelling. Water content was used to determine total porosity and dry density of samples according to equation (2), where  $\rho_d$  is dry density,  $\rho_s$  = rock density,  $w$  = water content and  $\rho_w$  = water density. The Cl accessible porosity was calculated according to experimental equations determined for compacted MX-80 by Muurinen & Carlsson (2013). The modelling of chloride activity in studied samples were performed by PhreeqC using thermodem database. The modelled Cl activities were compared with measured activities determined by ion selective electrodes (Figure 10).

$$\rho_d = \frac{\rho_s \times \rho_w}{\rho_s \times w + \rho_w} \quad (2)$$

Results of the measured Cl activities from samples prepared by mixing as example in Table 1 and Figure 86

Table 12 : Measured chloride activities by Cl<sup>-</sup> selective electrodes for different densities and salt solutions.

Sample Code	Target C <sub>Cl</sub> [mol/L]	Water content [w-%]	Dry density [g/cm <sup>3</sup> ]	Cl content [mg/gclay]	Experimental		PhreeqC		IS E <sub>Cl1</sub> [-]	IS E <sub>Cl2</sub> [-]
					C <sub>(Cl)tot_vol</sub> [mol/L]	C <sub>(Cl)accessible</sub> [mol/L]	a <sub>(Cl)tot_vol</sub> [-]	a <sub>(Cl)access.</sub> [-]		
1.1	1	77.4	0.88	13.89	0.51	1.31	0.33	0.80	0.31	0.14
2.1	0.1	77.3	0.88	0.29	0.01	0.03	0.01	0.03	0.25	0.11
3.1	0.01	73.0	0.92	0.18	0.01	0.02	0.01	0.02	0.07	0.06
1.2	1	63.1	1.01	9.42	0.42	1.34	0.28	0.82	0.75	0.61
2.2	0.1	59.4	1.05	1.16	0.06	0.19	0.05	0.14	0.36	0.24
3.2	0.01	53.2	1.12	0.18	0.01	0.04	0.01	0.03	0.078	0.05
1.3	1	43.6	1.26	3.23	0.21	1.06	0.15	0.65	0.96	0.45
2.3	0.1	38.7	1.34	0.13	0.01	0.05	0.01	0.04	0.23	0.07
3.3	0.01	37.4	1.36	0.07	0.01	0.03	0.01	0.03	0.1	0.05
1.4	1	28.0	1.56	1.90	0.19	1.60	0.14	0.98	0.12	0.13
2.4	0.1	26.7	1.59	0.09	0.01	0.08	0.01	0.06	0.17	0.2
3.4	0.01	27.2	1.58	0.07	0.01	0.06	0.01	0.05	0.14	0.25

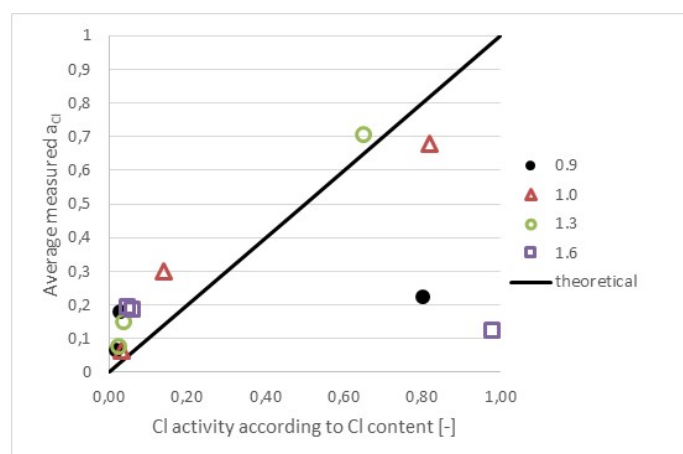


Figure 89. Measured chloride activities with Ag/AgCl electrodes versus calculated Cl activity by PhreeqC based on measured chloride content and Cl accessible porosities at studied dry densities in samples.

The initial chloride content in studied samples are about 0.1 mg/g<sub>clay</sub>, which means chloride activities from 0.01 to 0.06 for compacted bentonite samples in this study when dry density vary between 0.9 - 1.6 g/cm<sup>3</sup> (Figure 3 and Table I). This means that chloride activities in samples meant to be originally close to 0.01 are closer to 0.1, and thus 0.01 and 0.1 series have almost same Cl activities. The calculated Cl activity according to analysed values and measured Cl activity with Ag/AgCl electrode correspond quite well with in most of the samples. Anyhow, some samples measured Cl activity with electrode is much lower than expected according to theoretical value (samples 1.1 & 1.4 in Table I). This might be caused by inhomogenous distribution of chloride due to mixing method used for preparation of the samples. An example of the alternative preparation method for samples, where studied chloride concentration is equilibrated with sample by diffusion instead of mixing, can be seen in Figure 87.

Measured chloride activity by commercially available Ag(AgCl) Cl-sensitive electrode seems to correspond very well with calculated activity in Cl-accessible porewater.

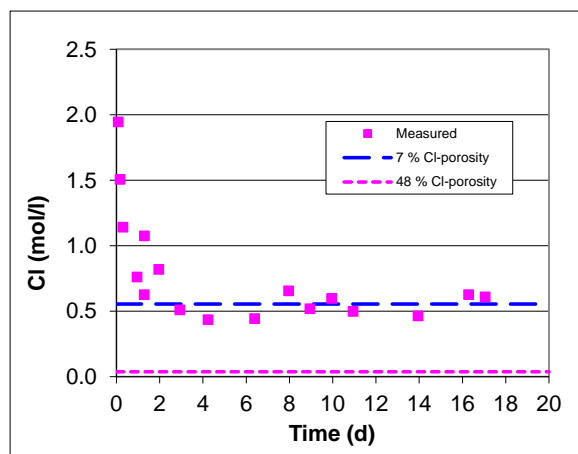


Figure 90. Measured Cl concentration with Ag/AgCl electrode in the porewater of MX-80 sample compacted to a dry density of 1.5 g/cm<sup>3</sup>. The Cl accessible porosity of 7 % match with measured values when per total water volume gives a clearly lower values.

The initial Cl content varies in bentonite and this should be taken into account in preparation of the samples, especially when low activities are measured in compacted bentonite. The amount of chloride in porewater can be calculated per total water volume or Cl accessible porewater volume according the measured dry density and initial Cl content. The other option is to wash initial Cl away before preparing the samples, at the same time gypsum, if present in the sample, will be removed. Anyhow, initial amount of the measured ions should be known and taken account when samples are prepared. Dissolving gypsum during the measurements will release calcium which will form complexes with Cl (CaCl, CaCl<sub>2</sub><sup>0</sup>) and, thus might lead misinterpretation of activity measurements of chloride by electrodes.

- Na selective electrodes with liquid filling

Na sensitive “Nasicon” electrode with filling solution was tested in Na-montmorillonite obtained by purifying MX-80, compacted at the target dry density 1.5 g/cm<sup>3</sup> and equilibrated with 0.1M Na<sub>2</sub>SO<sub>4</sub> solution by diffusion. The electrode was calibrated twice before experiments and once after experiments, calibration results can be seen in Figure 88 and results of the measurements in Figure 89.

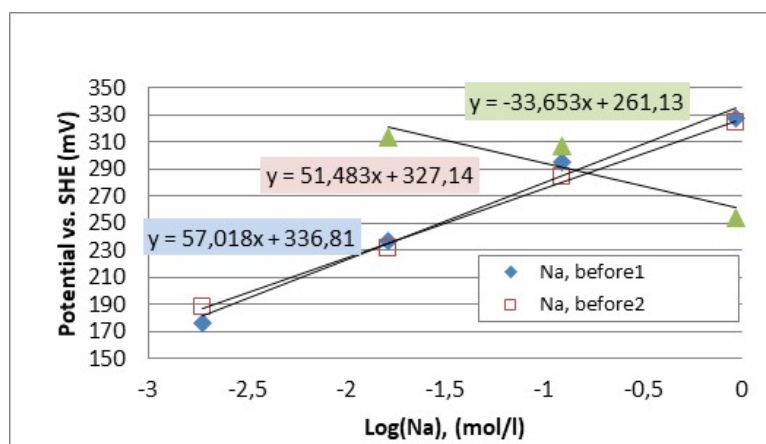


Figure 91. Liquid filled Na electrode calibration curves before and after experiments. Potential versus SHE were measured in solutions with different Na activities.

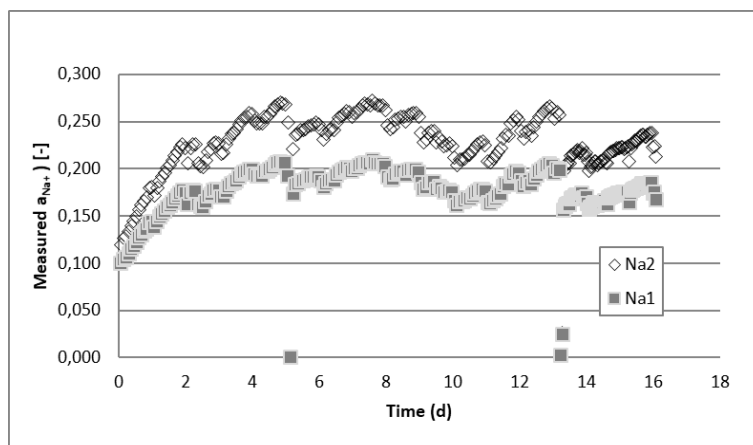


Figure 92 : Measured activity of  $Na^+$  in compacted bentonite saturated with 0.1 M  $Na_2SO_4$  solutions. According to PhreeqC calculations the activity of  $Na^+$  in this kind of solution should be about 0.12. Na1 as calibration 1 before experiments and Na2 as calibration 2 before experiments.

The measured activity seems to be close to 0.2. Anyhow, the simple geochemical modelling of studied solution shows the activity for  $Na^+$  about 0.12 in 0.1M  $Na_2SO_4$  solutions. The calibration before experiments gives a straight line with a good corresponding with sodium activity changes in solution. After experiments the calibration curve slope has changed sign and work as the anion sensitive electrode (Equation 1.). The reason for this might be the small leakage between membrane and screw that allows solution, used in calibration, to penetrate in inner part of electrode. Thus inner reference electrode (Ag/AgCl), sensitive for chloride, may cause the potential changes obtained by voltameter.

- Diffusion experiments with IrOx electrodes

The effect of a high pH solution on the pH in bentonite is studied with diffusion test bench (Figure 85) in anaerobic conditions. The compacted bentonite sample was prepared using anaerobic MX-80 bentonite and anaerobic deionized water. Bentonite was mixed with water and compacted in a compaction cell nitrogen atmosphere inside a glove-box. The compacted sample was subsequently moved into the titanium tube. The dry density of the bentonite sample was about 1.5 g/cm<sup>3</sup>. The three pH electrodes made of iridium oxide wire were placed in the bentonite and anaerobic deionised water was added to the external vessel. After 271 days the external solution was changed from the deionised water in equilibrium with bentonite (pH 8.4) to a saline solution of pH about 11.7 in order to simulate the effect of low-pH cement on bentonite in saline groundwater. Muurinen & Carlsson, (2008) [138] started to experiments at 2006 and experiments have been kept going on since.

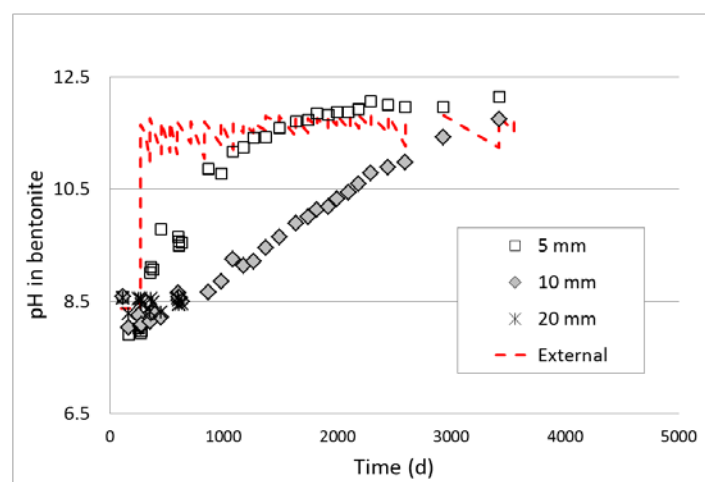


Figure 93: pH at different depths in bentonite and in the external solution of the diffusion cell sample. The solution chemistry was changed at 271 days from low-pH to high-pH.

The same IrOx electrodes have been kept measuring during the last ten years, while as, reference electrodes have been calibrated and changed multiple times.

## 4.2 Thermocouple psychrometers for water content measurement

### 4.2.1 Concept description and methodology

Thermocouple psychrometers have been used extensively for tracking the water content of bentonite-based material with high water contents (suctions below 6200 kPa). However, the available measuring electronics for long-term monitoring only operates using the psychrometric method, which is discontinuous and no very accurate due to the different mathematical criteria used to determine the stabilization of the cooling ramp.

The research carried out in Modern2020 frame intends to develop new sensors based on thermocouple psychrometers operating under the more accurate dew point method to measure water content in the bentonite barriers when close to saturation state. The work has been focused on:

1. The development of new electronics and software to perform measurements using the dew point method.
2. The integration of a commercial thermocouple psychrometer and the new electronics in a robust body to operate under the repository conditions.

Commercial available dew point measuring devices are scarce, complex, voluminous and expensive. Moreover, they are usually based on old fashioned electronics. The main goal is to find a new, cost-effective solution to handle the dew point measurement process for a long time. To achieve that, the following steps have been taken:

1. Analysis of available measuring devices and its technical documentation
2. Study of scientific papers to comprehend the physics involved and the most appropriate way to handle this task.
3. Prototyping of regulation and acquisition system following specifications found in the precedent studies.

4. Comparison of measurement between prototype and commercial devices using calibrated samples.
5. Tuning of prototype system.
6. Final design of boards.
7. Fabrication of several units for their final calibration and installation at LTRBM (WP 4.2)

#### 4.2.2 Experimental set-up

Arquimea has provided the materials and tools needed for the development of the system:

- Sample adiabatic chamber
- Commercial psychrometers PST-55
- Evaluation and prototype boards
- Discrete components

A Wescor HR33T microvoltmeter (supplied by Amberg) has been used to compare results

A Nucleo-144 development board from ST has been used for the system development, along with a commercial Wescor psychrometer PST-55.

During the tests, some different problems were found, mainly related to parasitic effects on the psychrometer during excitation (cooling cycles) and readout processes. Some of these effects were managed to be mitigated, and other have been admitted.

In Figure 91 and Figure 92 the experimental set-up is shown at its current stage.

Also, a LabView-based software has been developed to support debugging and control tasks. The software monitors all relevant parameters from the system during operation. Also, diverse configuration parameters can be tuned easily through the software.

In Figure 93, a complete measurement cycle is shown. The final measure can be found at the lower left side, indicating a relative humidity of RH=97.04% has been found.

Different tests have been performed using three different calibrated samples. The system has revealed to be sensitive to relative humidity changes, however it must still be evaluated and calibrated to determine its quality.



Figure 94 Isolated sample chamber to perform measurements



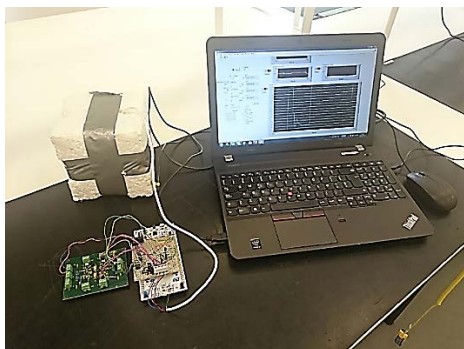


Figure 95 Complete system set up for prototype

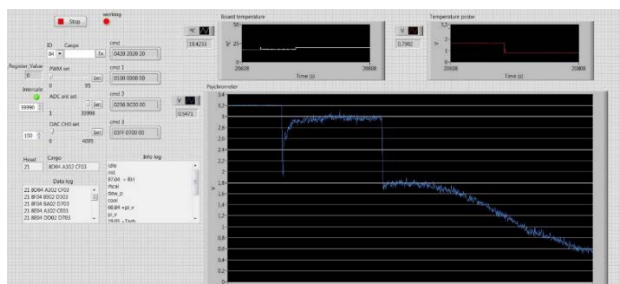


Figure 96 Software interface

### 4.2.3 Final design

The developed system has been designed on a printed circuit board and some demonstrators have been manufactured, like the one shown in Figure 94.

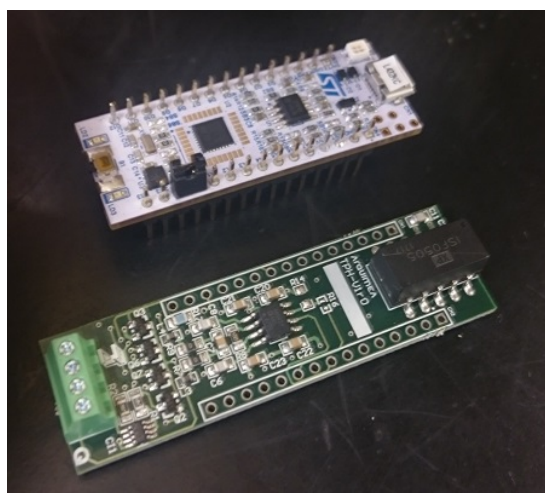


Figure 97: Proposed electronics

Two configurations for the sensor and readout units have been considered;

- Electronics integrated together with the sensor in a same casing. This configuration can be in other applications different than nuclear waste repositories (for instance in the agricultural sector).
- Sensor and readout unit are separated and connected between them via cable. This configuration is the one that will be fabricated for the demonstrator LTRBM.

### 4.2.4 Electronics

The demonstrators are based on an Nucleo-32 evaluation board and presents both USB and I2C connectivity to be commanded and read.

A connector is provided to easily connect or disconnect different psychrometer sensors.

A programmable current source is used to stimulate the psychrometer and two instrumentation amplifiers are provided to read the thermocouples. Finally, some transistors are used to connect or disconnect different parts of the circuit depending on the stage of the measurement process.

The power consumption expected from the system in a real application is very low, as the microprocessor can be set to deep low power modes that can be restored just to perform the readout process (order of 100 mW while measuring).

#### 4.2.5 Mechanical

The proposed measuring system is very compact, as can be found in Figure 94. It has dimensions of 63x20x20mm without the psychrometer.

For its use at LTRBM demonstrator, the psychrometer sensor head has been placed inside a porous cap made of sintered stainless steel while the rest of the sensor body has been sealed with epoxy-resin in a stainless-steel cylinder (see Figure 95). Casing dimensions are 75 mm long and 12 mm of external diameter.

The readout unit has been integrated in the wireless data transmission system.



Figure 98: Mechanical envelope of the sensor

#### 4.2.6 Conclusion/Discussion/Summary

A new system to measure relative humidity through dew point method using psychrometer sensors have been developed and tested. It has demonstrated to be sensitive to changes in relative humidity using calibrated samples.

The resulting system is low price and size, and it presents versatile features to be adapted to different cases of use, providing different working modes and control interfaces.

The developing process has not been easy but very profitable, and results are encouraging. The physics involved are very interesting, but it is not trivial to obtain good results from the very beginning. The biggest challenges during the development have been caused by noise and other parasitic effects, and big effort has been done to mitigate them to the minimum.

In conclusion, there is still room for improvements in psychrometer sensors. Methods like the one proposed in this case open new possibilities for measurement systems. Thus, it is important to dedicate efforts to investigate and develop new sensors because of the new opportunities hidden behind them.

## 5. Combined smart sensors

---

### 5.1 Objectives

There is a quite big range of total pressure cells on the market for the measurement of total. They usually come in 230mm diameter cylinder form with transducer attached via steel tube. Typical transducers used are vibrating wire (GeoKon), pneumatic (GLOTZL) or lately fibre optics. The CTU developed and used such pressure cells for civil engineering applications over 20 years now. Although these sensors are reliable, there are some disadvantages of their usage for EBS. In particular, their size and the necessity to use them in combination with other sensors to get full state of EBS, which is even more space demanding and measurements, are done in different places. Together with cabling and necessary data loggers, system gets complicated.

The new cell is targeted especially (but not exclusively) for measurements in the EBS system and to mitigate these problems. Although it is named as pressure cell, it is designed as all in one package. Along total pressure sensor, it integrates temperature, pore pressure sensor, RH sensors and electronics in the same package. This way the complete picture of EBS state can be obtained at once with much lower demands on space, cabling and power.

### 5.2 Objectives

The main objective for smart cell design were:

- Small size – less than 100 mm diameter
- Integrated body
- Measurement of
  - Total pressure
  - Pore pressure
  - Relative Humidity (optional)
- Low power design - long-term battery operation
- In-place signal processing and DAQ
- Integrated data logging for independent operation (optional)
- Digital interface (RS485, SDI-12)

From the DAQ point of view, the aim is to completely process the signal from sensors inside the cell electronics and give the user digital output with no further processing required. This way the noise and other issues (e.g. parasitic capacitance) from analogue cabling will be eliminated and techniques such as oversampling can be employed to further increase precision. Moreover having smart sensors also enables wide range of possibilities for measurements and communication. With further development of its programming, the cell can take measurements as necessary (triggered by various events) and send the data as one package at later stage or raise immediate alarms.

### 5.3 Mechanical setup

From the mechanical point of view the design of smart cell is driven by the necessity to combine the pressure exchanger, which transfer total pressure from the surface of the cell into pressure sensor itself and housing for the electronics and other sensors. The classic setup of pressure cell is a flat disc (around 200-250mm in diameter) filled with fluid with pressure transducer attached via short pipe. Piezometers and other sensors are typically cylinders (5-30mm diameter) with sensing part at the top of cylinder and cable on the other end. Just stacking those sensors together would create bulky device with irregular

shape and fragile protruding parts, which is unacceptable. Even if the piezometer and other sensors were integrated into pressure transducer body of the pressure cell the arrangement could not be used for two reasons:

- It takes lot of space
- The sensor housing is far away from place of measurement (cylinder) therefore even if additional sensor would be added they would measure in completely different place

To solve this problem the shape of sensor housing was changed into low profile cylinder and pressure exchanger was placed on one of the cylinder bases. The target for integrated cell was set to 80mm in diameter with no protrusions going out of the main body (except cable). This size was selected as a balance between the miniaturisation and precision of measurement (total pressure measurement needs large pressure exchange area). Although it may still seems big it poses significant engineering challenge to integrate all sensors in limited space while providing protected space for electronics.

The design of the new integrated cell is cylindrical 80mm in diameter and 25mm height. It consist of the main stainless steel body, which has welded on membrane on top and steel lid on bottom covering the electronics compartment.

The main body is major structural element. It holds all the sensors in place and provides shielded space for the electronics. The total pressure is measured using piezo resistive sensor submerged in the oil reservoir at the top main body. The reservoir is enclosed by top of main body and welded on membrane. It effectively acts as pressure exchanger transferring total pressure from environment into sensor. The pore pressure is measured using same type of pressure transducer directly connected to the environment via side holes in the body and porous stone acting as filter. The usage of same sensor types allowed simplifying the electronics. Both sensor ranges can be individually selected in order to accommodate for expected total and pore pressures.

The RH sensor is exposed to the environment in similar way as pore pressure sensor. It sits in side chamber and it is protected by porous stone. It also serves for measurement of temperature along thermometers on electronics board.

The electronics compartment takes approximately ½ of the space of inner body. It offers protected space sealed by bottom steel lid. At final stage before the in-situ installation, the compartment (electronics) will be filled with conformal coating for additional protection against moisture.

The development of the smart cell has been performed joint by CTU and TUL.

The design of the electronics, board prototypes and firmware development has been performed by TUL.

The design of the mechanical part, sensors selection, final assembly and testing has been performed by CTU. Several revision of the body has been prepared and manufactured. 3D modelling and rapid prototyping using 3D printing have aided the design (Figure 101). Two revisions of the body have been manufactured with third revision to be designed by the end of the project to solve minor mechanical problems of second version.

## 5.4 First version

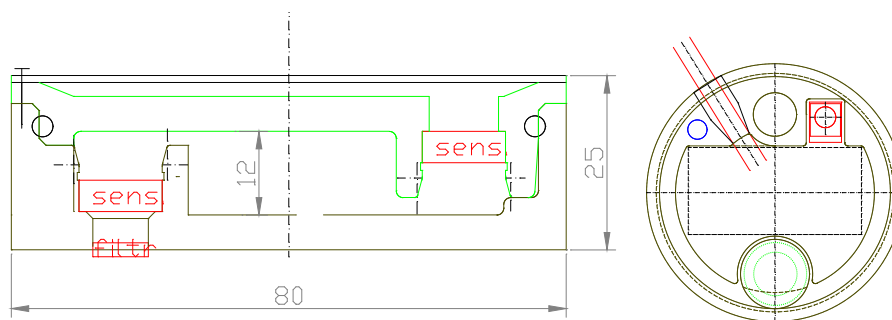


Figure 99: Conceptual design as presented during WP3 workshop (2015) (images not to scale)

The conceptual design (Figure 96) was first presented in 2015 during WP3 workshop in Madrid. It consisted of two parts. The top part containing total pressure exchanger and transducer (piezo resistive). The bottom part containing pore pressure transducer, electronics and RH transducer. This design had some disadvantages:

- Two complicated bodies
- RH and pore pressure measurement on the other side than total pressure
- Problematic sealing and assembly

These problems were tackled down during the design process. All the transducers and electronics were moved into “top” part e.g. into main body which become more complex (**Erreur ! Source du renvoi introuvable.**). The measurement ports for RH and pore pressure were moved to the cylinder side as closest available place to the total pressure measurement. That allowed to have bottom part as simple lid.

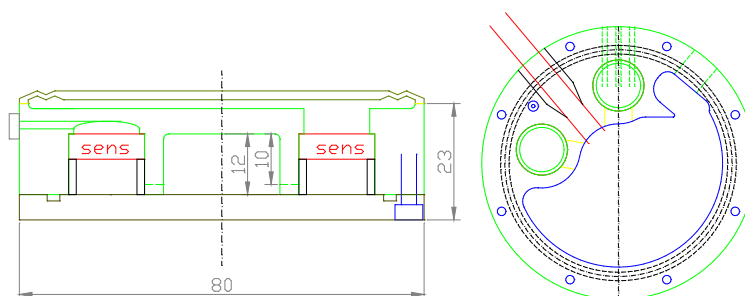


Figure 100: Cross section of the first version of the body design (images not to scale)

Some technical issues were not completely solved at the time of first body manufacturing (Figure 97) as the first revision of the cell body has been designed as proof of the concept. In particular, the filter stones for RH and pore pressure were not included. This was a deliberate choice, as it did not hamper the intended use of the prototype.



Figure 101: (On the left) First body version of smart cell (stainless steel body; (on the right) 3D printed prototype

The prototype (including electronics) has been tested at CEG labs (Figure 99). The test were promising however, excessive high temperature dependency was discovered. The high temperature dependency has been tracked down to the oil expansion in the pressure exchanger.



Figure 102: First prototype test in press (heat toleration test in progress

## 5.5 Second version

Second version of the smart cell body has been developed based on results of the first revision tests and to tackle parts omitted from first revision (Figure 100). The main points tackled by the second revision were:

- Oil expansion problem
- Pore pressure transducer filter incorporation (filter stone)
- RH transducer filter incorporation (filter stone)
- Improvement of RH transducer support

The oil expansion problem was mitigated by reduction of the oil volume inside the pressure exchanger. This has been achieved by two changes in design - by reduction of space below the membrane and by moving pressure transducer close to the membrane (reduction of dead space). Moreover the shape of membrane and of the body has been optimised for easier manufacturing. In particular the body has been redesigned to have flat surface with no protrusions facing the pressure exchanger.

The space for filter stones was designed as part of the wall. The shape of filter stones has been unified for RH and pore pressure transducer as a 10 mm diameter disc.

The area of RH transducer compartment has been redesigned. The RH sensor board is placed in the cylindrical hole in the cell side. The hole has smaller diameter in the inner part forming support for the board. The filter stone closes the hole from the outside and is separated from RH board by ring spacer. On the inside side of the cell wall a small compartment has been designed for easier sealing potting of RH board and connecting cable.

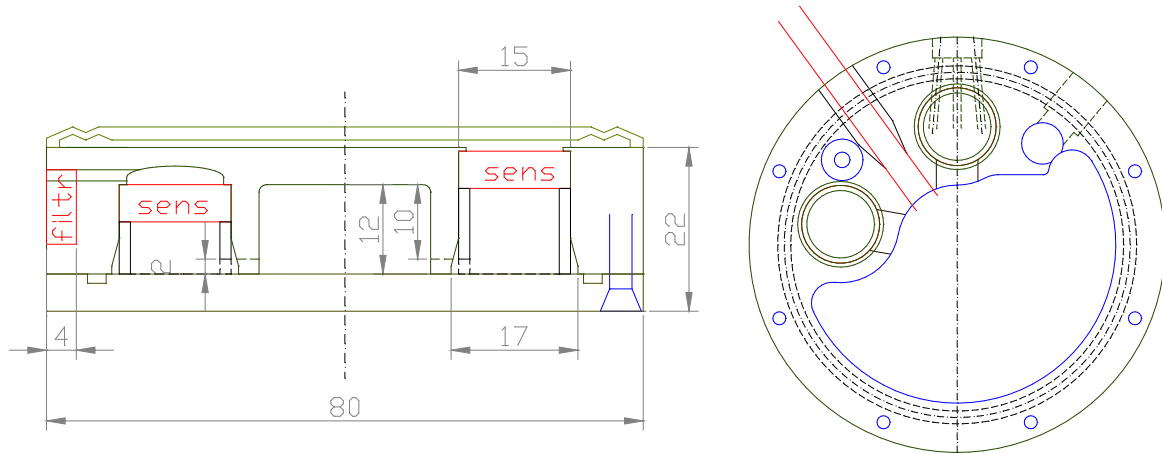


Figure 103: Cross section of the second version of the body design (images not to scale)

The second revision is undergoing testing and it will be installed in the LTRBM (Figure 102). The cell will be connected to the LTRBM via RS485 interface. As the LTRBM DAQ requires MODBUS protocol connection a new software has been developed in order to connect the smart cell. The software translates smart cell ascii based protocol into MODBUS. The LTRBM cell electronics has been completely potted for additional water protection.

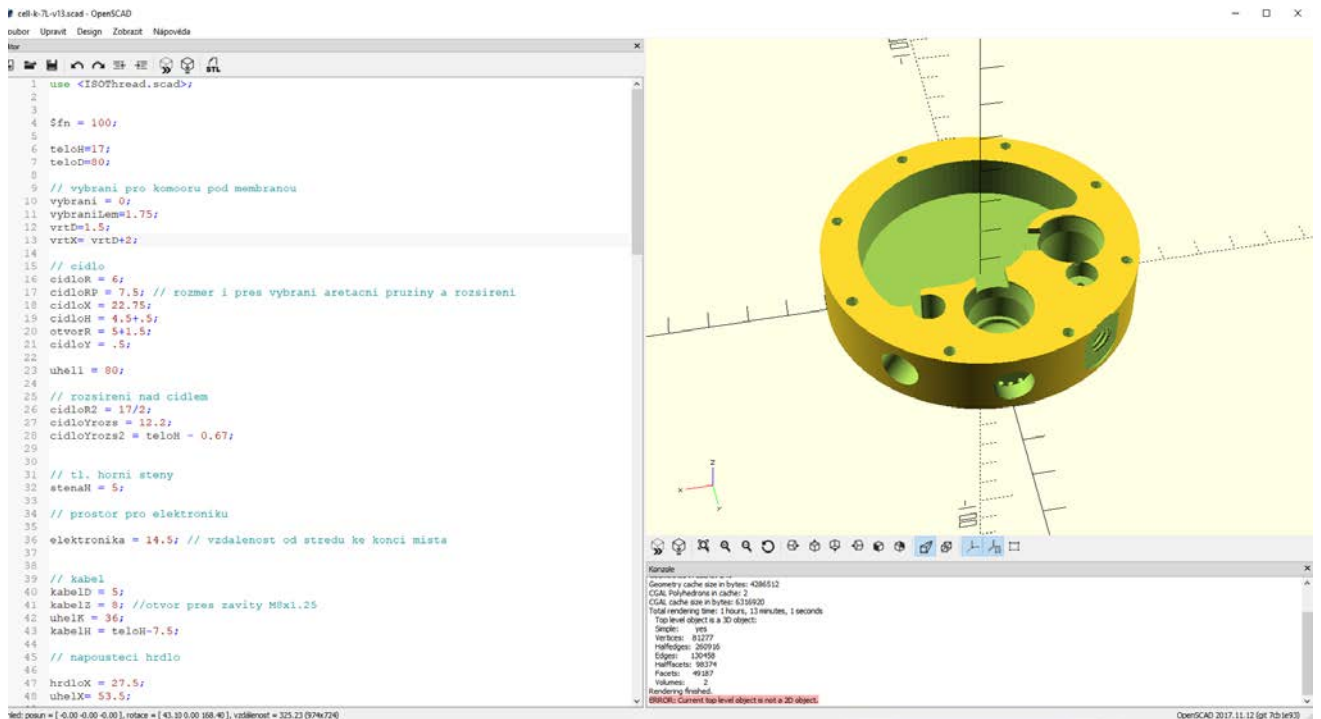


Figure 104: 3D model



Figure 105: 2nd revision smart cells (cell on the left designed for LTRBM)

## 5.6 Electronics

Core electronics of the smart sensor cell is described Figure 103 . All components must work at voltage given by a lithium single cell battery, i.e. in range from 3.3 V down to 2.0 V as close as possible.

From an electronical point of view, the Pressure Sensor is a resistance full bridge having overall resistance about 3 k $\Omega$ . It should be supplied with voltage about 3 V. Diagonal output signal is amplified with a single operational amplifier in a simple differential wiring with gain about 20. Operational Amplifier ADA4051 is rail-to-rail, zero-drift chopping amplifier. It means that it can utilize the full input range of subsequent ADC in the ratiometric measurement and exhibits low drift and offset (max. 15  $\mu$ V). It is capable to operate at 1.8–5.5 V with low consumption only 13  $\mu$ A. Low input current 5 pA does not load the bridge output.

Temperature & Relative Humidity (RH) sensor SHT-25 has excellent resolution (0.01  $^{\circ}$ C | 0.04 %RH) and precision ( $\pm$ 0.2  $^{\circ}$ C |  $\pm$ 1.8 %RH). It can work down to 2.1 V with consumption 0.3 mA. Digital output of the sensor is read by I2C interface. Unfortunately, its slave address cannot be selected so only single device can be served.

Temperature sensor SHT-21 utilizes a part of the same internal electronic blocks as SHT-25 so it has almost the same parameters. Its slave address is fortunately different so both sensors can communicate on the same I2C bus.

Choice of a Data EEPROM Memory was limited by the supply voltage range (1.8 V cannot be used) and a packaging because we had to use a small package but could not solder special packages (QFN, BGA etc.), at least for a functional sample / prototype. AT45DB321E is the 32 Mb memory in 8-pad DFN package with fast SPI interface, working in range 2.3–3.6 V.

Supply of all above-mentioned components (Supply Domain VCS) is switched off between measurements to conserve a battery energy.

Microcontroller STM32L052K8 is powerful (32-bit ARM Cortex-M0+ core) yet low-power MCU suitable for battery operated devices. It runs in range 1.65–3.6 V consuming 88  $\mu$ A/MHz (core only, also approx. per MIPS). It is equipped with 64 KB Code Flash, 8 KB SRAM, 2 KB EEPROM and rich set of peripherals. Peripherals used in the application are: 2 $\times$ UART, SPI, I2C, 12-bit ADC (2 channels), RTC, 7 GPIOs. Whole microcontroller (MCU) consumes 0.6 mA at frequency 4 MHz used in the device but the most important is the consumption during sleep (stop mode) with running RTC and SRAM retention – only 1  $\mu$ A.

Supply circuits and communication interfaces of the sensor cell are depicted in Figure 104.

RS-485 is a standard, widespread and well-known industrial communication interface. Its driver chip requires 5 V with sufficiently high supply current but it works at high baud rates and long distances.



SDI-12 is a special interface for slow data rate sensors (e.g. meteorological) connected to a datalogger. It works half-duplex over single wire at 5-V-logical levels with baudrate 1200 Bd.

Both interfaces require signal for switching output driver on and the 5 V supply which is stabilized from an external voltage. Input supply voltage can vary not only due to external supply selection but also due to voltage drop on a connection cable. Regulator 5 V was originally designed as a switching one but available chips exhibited high output voltage variation in low output current mode when they had to switch their run and stop modes over. Then simple linear regulator was used. A comparator signalizes to the MCU and switches off the battery when the external voltage is present. Since a low leakage diode must be used to separate the battery from reverse discharge by an output of non-supplied voltage regulator, the regulator does not stabilize about 3 V but 4 V considering a voltage drop across the diode.

The Lithium cell battery CR-2354/GUN (Li-MnO<sub>2</sub>, 560 mAh) is soldered in the PCB. A jumper connects it finally to the electronics before closing the cell.

MOSFET Switches are used for the battery connection and switching on the sensors & memory VCS domain.

Level Convertors convert and filter remote RESET and BOOT signals from the external supply level to the MCU supply level.

The cell is connected to a remote data converter either stand-alone RS 485/Ethernet or notebook's RS-485/USB or to a datalogger (SDI-12) with standard 4-pair shielded UTP cable. The cell communicates at RS-485 baudrate 115.2 kBD that makes possible using the cable with length up to 300 m.

PCB of the cell is shown in Figure 105 and assembling of the cell body, PCB and sensors in Figure 106

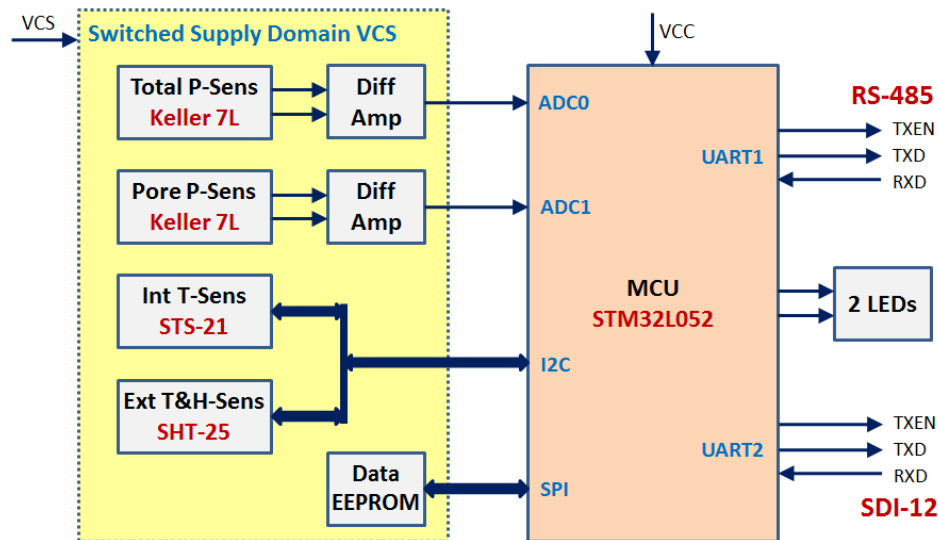


Figure 106: Block diagram of the core part of the smart sensor cell

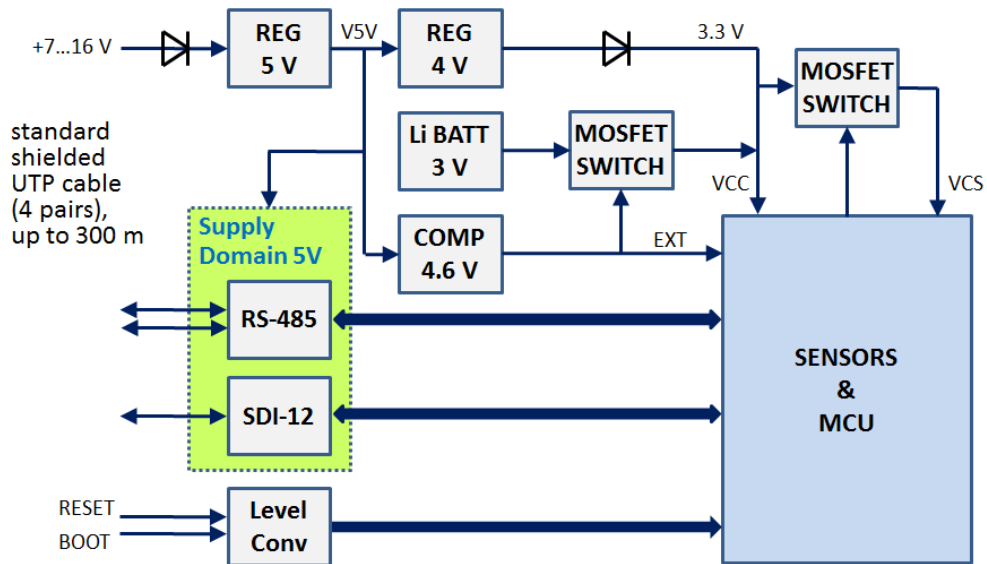


Figure 107: Block diagram of supply, interfaces and outer connection of the smart sensor cell

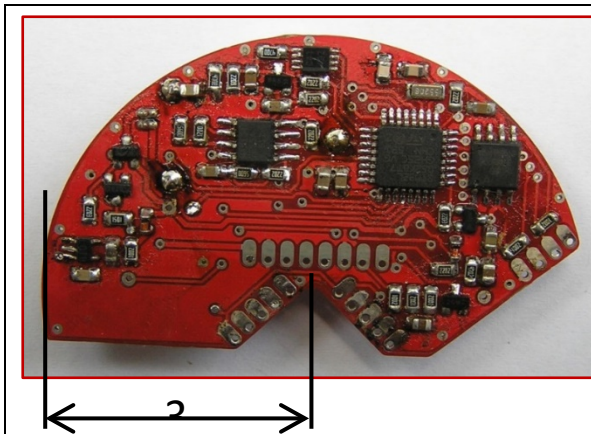


Figure 108: Bottom view of the PCB

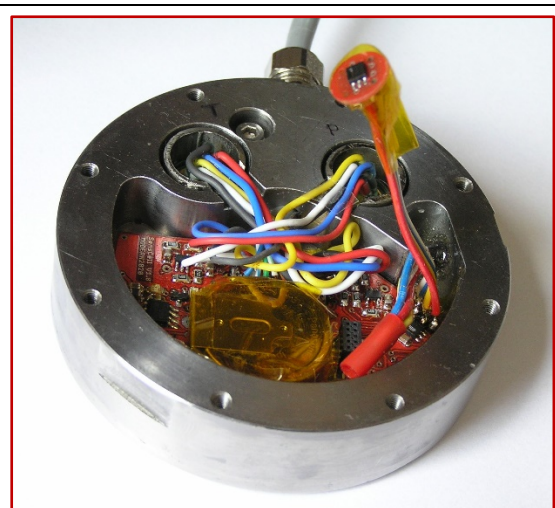


Figure 109: First version of the cell electronics compartment (SHT-25 is pulled out from its measuring place)

**Firmware** in the MCU fulfills following functions of the cell:

- At internal battery supply
  - Sleeping only (OFF)
  - Sleeping | Periodical sampling & storage in memory
- At external supply
  - Periodical sampling & storage in memory (without a communication)
  - Connected by SDI-12 (V1.3): on-demand sampling & data sending
  - Connected by RS-485 (115.2 k Bd, ASCII messages with parity):
    - ✓ On-demand sampling & data sending

- ✓ Download of acquired data from the memory
- ✓ Execution of auxiliary commands: settings: RTC date|time, SDI address, mode, sampling period; diagnostics, returns a device info (HW/FW version, S/N, etc.), No. of samples in memory
- ✓ Firmware update by the built-in bootloader & PC application

Since a record of one measurement sample contains 8 items of 16-bit integer number (compressed date, compressed time, 2×pressure, 2×temperature, humidity, battery voltage) the 32-Mbit data memory can store up to 262144 samples i.e. 3 samples/hour for 10 years.

**Basic test measurements** of the cell electronics have been carried out. It was tested with a laboratory supply replacing the battery. The pressure sensors were replaced with resistor bridges. Stable 14-bit value on the pressure channels has been achieved due to a huge ADC oversampling. Within the full voltage range 2.0–3.3 V a deviation of the value is only 0.3 %FS. Although the data sheets of some components show narrower supply range the electronics runs down to 2.0 V that makes possible full exploitation of the battery capacity.

Testing in a temperature chamber has verified a functionality of the electronics in the temperature range at least –20...+90 °C. A deviation of the pressure value within the temperature range 0...+85 °C is 0.6 %FS.

Consumptions at ambient and maximal working temperature are written in Table 13. Energy spent during one MCU run period (i.e. sampling of all sensors and storing data inside memory) is recalculated per year at sample period 3 samples/hour.

Table 13 : Results on basic test measurement on cell electronics

temperature	sleep current	consumption	energy/samp.	cons. @ 3 S/h
+25 °C	1.04 µA	9.1 mAh/yr	1.91·10 <sup>-4</sup> mAh	5.0 mAh/yr
+85 °C	2.09 µA	18.3 mAh/yr	1.99·10 <sup>-4</sup> mAh	5.2 mAh/yr

Considering real (due to self-discharge and higher temperature) capacity of the battery as ½ of nominal, battery life at consumption 24 mAh/yr can reach 10 years minimally.

From the point of view of remote and sealed (behind the barriers) placement of the cell, an average demanded communication rate is 0.4 kbit/hour (0.1 bit/s) at above mentioned sample rate 3 S/h. It assumes to sent data more efficiently, in binary form, which would require minor changes in firmware.

Continuous supply delivery from an alternative power supply sources would require 3 µA at 3 V except the communication. A buffer capacitor would have to be added to cover the peak consumption during the MCU run period.

## References

---

- [1] ANDRA, “Milestone 39: Design and performances of a sensing system to provide distributed radiation, hydrogen strain and temperature measurements in geological repository environments,” ANDRA, Tech. Rep., 2018.
- [2] S. Girard, Y. Ouerdane, A. Boukenter, C. Marcandella, J. Bisutti, J. Baggio, and J.-P. Meunier, “Integration of optical fibers in radiative environments: Advantages and limitations,” in Proceedings of ANIMMA 2011, 2011.
- [3] I. Petukhova, A. Fotiadi, A. Shubin, A. Tomashuk, S. Novikov, I. Zolotovskiy, O. Antipov, K. Panajotov, H. Tienpont, and P. Mégret, “Monitoring of gamma-irradiated Yb-doped optical fibers through the pump induced refractive index change effect,” in Proceedings of ANIMMA 2011, 2011, p. Paper 1.13.
- [4] S. Girard, J. Kuhnenn, A. Gusarov, B. Brichard, M. Van Uffelen, Y. Ouerdane, A. Boukenter, and C. Marcandella, “Radiation effects on silica-based optical fibers: Recent advances and future challenges,” IEEE Transactions on Nuclear Science, vol. 60, no. 3, pp. 2015–2036, 2013.
- [5] A. Othonos, Fiber Bragg Gratings: Fundamentals and Applications in Telecommunications and Sensing. Artech House, 1999.
- [6] J. A. Gusarov and S. K. Hoeffgen, “Radiation effects on fiber gratings,” IEEE Transactions on Nuclear Science, vol. 60, no. 3, pp. 2037–2053, jun 2013.
- [7] M. R. Samsudin, Y. G. Shee, F. R. M. Adikan, B. B. A. Razak, and M. Dahari, “Fiber bragg gratings hydrogen sensor for monitoring the degradation of transformer oil,” IEEE Sensors Journal, vol. 16, no. 9, pp. 2993–2999, may 2016.
- [8] Y. Kim, T. K. Noh, Y. W. Lee, E.-S. Kim, B.-S. Shin, and S.-M. Lee, “Fiber-optic hydrogen sensor based on polarization-diversity loop interferometer,” Journal of the Korean Physical Society, vol. 62, no. 4, 2013.
- [9] Y.-T. Dai, M. Yang, J. M. Karanja, and Q. Zhao, “Novel FBG sensors based on cladding surface microstructures,” in 23rd International Conference on Optical Fibre Sensors, J. M. López-Higuera, J. D. C. Jones, M. López-Amo, and J. L. Santos, Eds. SPIE, jun 2014.
- [10] H.-t. Song, G.-m. Ma, J. Jiang, C.-r. Li, Y.-t. Luo, and H.-b. Wang, “Dissolved hydrogen measurement with palladium-silver FBG sensor in transformer oil,” in 2015 IEEE Electrical Insulation Conference (EIC). IEEE, aug 2015.
- [11] X. Zhou, Y. Dai, M. Zou, J. M. Karanja, and M. Yang, “FBG hydrogen sensor based on spiral microstructure ablated by femtosecond laser,” Sensors and Actuators B: Chemical, vol. 236, pp. 392–398, nov 2016.
- [12] J. Jiang, G.-M. Ma, C.-R. Li, H.-T. Song, Y.-T. Luo, and H.-B. Wang, “Highly sensitive dissolved hydrogen sensor based on side-polished fiber bragg grating,” IEEE Photonics Technology Letters, vol. 27, no. 13, pp. 1453–1456, jul 2015.
- [13] G. M. Ma, J. Jiang, C. R. Li, H. T. Song, Y. T. Luo, and H. B. Wang, “Pd/ag coated fiber bragg grating sensor for hydrogen monitoring in power transformers,” Review of Scientific Instruments, vol. 86, no. 4, p. 045003, apr 2015.
- [14] S. Saad, L. Hassine, and W. Elfahem, “Hydrogen FBG sensor using pd/ag film with application in propulsion system fuel tank model of aerospace vehicle,” Photonic Sensors, vol. 4, no. 3, pp. 254–264, jul 2014.
- [15] J. M. Karanja, Y. Dai, X. Zhou, B. Liu, and M. Yang, “Microstructured femtosecond laser assisted FBG hydrogen sensor,” Optics Express, vol. 23, no. 24, p. 31034, nov 2015.

- [16] L.-j. Cui, H.-c. Shang, G. Zhang, Y. Li, and Z.-x. Zhao, "Experimental study on optical fiber bundle hydrogen sensor based on palladium-silver optical thin film," *Optoelectronics Letters*, vol. 9, no. 1, pp. 13–17, jan 2013.
- [17] L.-j. Cui, H.-c. Shang, G. Zhang, Z.-x. Zhao, and J. Zhou, "Optical fiber hydrogen sensor based on light reflection and a palladium-silver thin film," *Optoelectronics Letters*, vol. 7, no. 4, pp. 249–252, jul 2011.
- [18] G. Wang, M. Yang, J. Dai, C. Cheng, and Y. Yuan, "Microfiber bragg grating hydrogen sensor base on co-sputtered pd/ni composite film," in *Fifth Asia-Pacific Optical Sensors Conference*, B. Lee, S.-B. Lee, and Y. Rao, Eds. SPIE, jul 2015.
- [19] J. Dai, M. Yang, Z. Yang, Z. Li, Y. Wang, G. Wang, Y. Zhang, and Z. Zhuang, "Enhanced sensitivity of fiber bragg grating hydrogen sensor using flexible substrate," *Sensors and Actuators B: Chemical*, vol. 196, pp. 604–609, jun 2014.
- [20] M. Yang, G. Wang, J. Dai, Z. Yang, Z. Li, Y. Wang, Y. Zhang, and Z. Zhuang, "Fiber bragg grating sensors with pt-loaded WO<sub>3</sub> coatings for hydrogen concentration detection down to 200 ppm," *Measurement Science and Technology*, vol. 25, no. 11, p. 114004, oct 2014.
- [21] Z. Li, M. Yang, J. Dai, G. Wang, C. Huang, J. Tang, W. Hu, H. Song, and P. Huang, "Optical fiber hydrogen sensor based on evaporated pt/WO<sub>3</sub> film," *Sensors and Actuators B: Chemical*, vol. 206, pp. 564–569, jan 2015.
- [22] C. Caucheteur, M. Debliqy, D. Lahem, and P. Mégret, "Hybrid fiber gratings coated with a catalytic sensitive layer for hydrogen sensing in air," *Optics Express*, vol. 16, no. 21, p. 16854, oct 2008.
- [23] S. Masuzawa, S. Okazaki, Y. Maru, and T. Mizutani, "Catalyst-type-an optical fiber sensor for hydrogen leakage based on fiber bragg gratings," *Sensors and Actuators B: Chemical*, vol. 217, pp. 151–157, oct 2015.
- [24] M. Yang, Z. Li, J. Dai, Z. Yang, Y. Zhang, and Z. Zhuang, "Comparison of optical fiber bragg grating hydrogen sensors with pd-based thin films and sol-gel WO<sub>3</sub> coatings," *Measurement Science and Technology*, vol. 24, no. 9, p. 094009, jul 2013.
- [25] T. Wu, X. Wei, X. Yang, Y. Quan, G. Lv, Y. Shi, S. Wu, S. Li, and Z. Chen, "Highly sensitive hydrogen sensor based on pd-functionalized titania nanotubes prepared in water-contained electrolyte," *Journal of Materials Science: Materials in Electronics*, vol. 28, no. 2, pp. 1428–1432, sep 2016.
- [26] D. Luna-Moreno, D. Monzón-Hernández, J. Villatoro, and G. Badenes, "Optical fiber hydrogen sensor based on core diameter mismatch and annealed pd-au thin films," *Sensors and Actuators B: Chemical*, vol. 125, no. 1, pp. 66–71, jul 2007.
- [27] C. Caucheteur, M. Debliqy, D. Lahem, and P. Megret, "Catalytic fiber bragg grating sensor for hydrogen leak detection in air," *IEEE Photonics Technology Letters*, vol. 20, no. 2, pp. 96–98, jan 2008.
- [28] Y. S. Chiam, I. Z. M. Ahad, S. W. Harun, S. N. Gan, and S. W. Phang, "Effects of the dopant ratio on polyaniline coated fiber bragg grating for pH detection," *Synthetic Metals*, vol. 211, pp. 132–141, jan 2016.
- [29] B. N. Shivananju, G. R. Prashanth, S. Asokan, and M. M. Varma, "Reversible and irreversible pH induced conformational changes in selfassembled weak polyelectrolyte multilayers probed using etched fiber bragg grating sensors," *Sensors and Actuators B: Chemical*, vol. 201, pp. 37–45, oct 2014.
- [30] B. N. Shivananju, V. Prasad, G. A. Chenrayan, A. Misra, M. M. Varma, and S. Asokan, "Nanomaterials coated multiplexed fiber bragg grating for multiparameter sensing," in *Quantum Sensing and Nanophotonic Devices XII*, M. Razeghi, E. Tournié, and G. J. Brown, Eds. SPIE, feb 2015.




- [31] I. Yulianti, A. S. M. Supa'at, and S. M. Idrus, "Characterization of fiber bragg grating sensor for pH measurement," in 2014 IEEE/ASME International Conference on Advanced Intelligent Mechatronics. IEEE, jul 2014.
- [32] X. Liang, S. Chen, H. Huang, and W. Liu, "Study on sensitivity improving of fiber bragg grating based pH sensor," *Photonic Sensors*, vol. 4, no. 1, pp. 28–33, nov 2013.
- [33] Y. Lin, S. Chen, M. Wang, and W. Liu, "Fiber-optic fast response pH sensor in fiber bragg gating using intelligent hydrogel coatings," *Optical Engineering*, vol. 54, no. 5, p. 057107, may 2015.
- [34] S. Dong, M. Luo, G. Peng, and W. Cheng, "Broad range pH sensor based on sol-gel entrapped indicators on fibre optic," *Sensors and Actuators B: Chemical*, vol. 129, no. 1, pp. 94–98, jan 2008.
- [35] S. Islam, R. A. Rahman, Z. B. Othaman, S. Riaz, and S. Naseem, "Synthesis and characterization of multilayered sol-gel based plastic-clad fiber optic pH sensor," *Journal of Industrial and Engineering Chemistry*, vol. 23, pp. 140–144, mar 2015.
- [36] P. Chen, Z. Wang, S. Zong, H. Chen, D. Zhu, Y. Zhong, and Y. Cui, "A wide range optical pH sensor for living cells using au@ag nanoparticles functionalized carbon nanotubes based on SERS signals," *Analytical and Bioanalytical Chemistry*, vol. 406, no. 25, pp. 6337–6346, aug 2014.
- [37] S. Derinkuyu, K. Ertekin, O. Oter, S. Denizalti, and E. Cetinkaya, "Fiber optic pH sensing with long wavelength excitable schiff bases in the pH range of 7.0–12.0," *Analytica Chimica Acta*, vol. 588, no. 1, pp. 42–49, apr 2007.
- [38] S. T. Lee, J. Gin, V. P. N. Nampoori, C. P. G. Vallabhan, N. V. Unnikrishnan, and P. Radhakrishnan, "A sensitive fibre optic pH sensor using multiple sol-gel coatings," *Journal of Optics A: Pure and Applied Optics*, vol. 3, no. 5, pp. 355–359, jul 2001.
- [39] T. H. Nguyen, T. Venugopala, S. Chen, T. Sun, K. T. V. Grattan, S. E. Taylor, P. A. M. Basheer, and A. E. Long, "Fluorescence based fibre optic pH sensor for the pH 10–13 range suitable for corrosion monitoring in concrete structures," *Sensors and Actuators B: Chemical*, vol. 191, pp. 498–507, feb 2014.
- [40] P. Zubiate, C. R. Zamarreño, I. D. Villar, I. R. Matias, and F. J. Arregui, "Tunable optical fiber pH sensors based on TE and TM lossy mode resonances (LMRs)," *Sensors and Actuators B: Chemical*, vol. 231, pp. 484–490, aug 2016.
- [41] MoDeRn Deliverable 4.1 "Case Studies Final Report" 2013.
- [42] Niklès M., Thévenaz L., Robert P.A. (1997) "Brillouin Gain Spectrum Characterization in Single-Mode Optical Fibers" *Journal of Lightwave Technology* Vol 15 No. 10 pp1842-1851.
- [43] S. Delepine-Lesoille, J. Bertrand, L. Lablonde, X Phéron, "Hydrogen influence on Brillouin and Rayleigh distributed temperature or strain sensors" *Proc. SPIE 8421*, 22<sup>nd</sup> International Conference on Optical Fiber Sensors (OFS22), October 2012
- [44] O'Keefe S, Fitzpatrick C, Lewis E, Al-Shamma'a Al. A review of optical fibre radiation dosimeters. *Sensor review*. 2008 Mar 28;28(2):136-42.
- [45] B. Brichard, et al, "Reduction of the radiation-induced absorption in hydrogenated pure silica core fibres irradiated in situ with  $\gamma$ -rays," *J. of Non-Crystalline Solids*, vol. 353, 2007, pp. 466-472.
- [46] Faustov A., "Advanced fiber optics temperature and radiation sensing in harsh environments", PhD Thesis, Université de Mons, 2014.
- [47] X. Phéron, S. Girard, A. Boukenter, B. Brichard, S. Delepine-Lesoille, J. Bertrand, and Y. Ouerdane "High g-ray dose radiation effects on the performances of Brillouin scattering based optical fiber sensors", *Optics Express*, Vol. 20 Issue 24, pp.26978-26985 (2012)
- [48] C. Cangialosi, S. Girard, M. Cannas, A. Boukenter, E. Marin, S. Agnello, S. Delepine-Lesoille, C. Marcandella, P. Paillet, and Y. Ouerdane, "On-line characterization of gamma radiation vulnerability of Raman based distributed fiber optic sensor", *IEEE Trans.on Nucl. Sci.*, 2016D.

- Alasia, et al. "The effects of gamma-radiation on the properties of Brillouin scattering in standard Ge-doped optical fibres" *Measurement Science and Technology* 17.5 (2006): 1091.
- [49] C. Cangialosi, Y. Ouerdane, S. Girard, A. Boukenter, S. Delepine-Lesoille, J. Bertrand, C. Marcandella, P. Paillet, M. Cannas, "Development of a Temperature Distributed Monitoring System Based On Raman Scattering in Harsh Environment" *IEEE Transactions on Nuclear Science* Vol. 61, No. 6, Dec. 2014
- [50] Modern2020, WP3.4, Milestone 37: C. Broadway, D. Kinet, P. Mégret "Radiation, H2 and pH sensors based on FBG technology" May 2018
- [51] C. Cangialosi et al., "Steady State  $\gamma$ -ray radiation effects on Brillouin fiber sensors" OFS24 24th International Conference on Optical Fiber Sensor, 28/09 au 02/10/15, Curitiba, Brazil, SPIE 9634.
- [52] I. Planes, S. Girard, A. Boukenter, E. Marin, S. Delepine-Lesoille, C. Marcandella, Y. Ouerdane "Steady  $\gamma$ -ray effects on the performances of PPP-BOTDA and TW-COTDR fiber sensing" *Sensors*, 2017, 17, 396
- [53] Rizzolo S. and al., "Vulnerability of OFDR-based distributed sensors to high  $\gamma$ -ray doses", *Opt. Express*, vol. 23, no. 15, pp.18997-19009 (2015).
- [54] Rizzolo S. and al., "Radiation effects on OFDR-based sensors", *Opt. Lett.*, vol.40, no.20, pp. 4571-4574 (2015).
- [55] Rizzolo S. and al. "Radiation hardened optical frequency domain reflectometry distributed temperature fiber-based sensors", *IEEE Trans. Nucl.Sci.*, vol.62, no.6, pp.171-176.
- [56] S. Girard et al., "Radiation effects on silica-based optical fibers: Recent advances and future challenges," *IEEE Trans. Nucl. Sci.* , vol. 60, no. 3, pp. 2015–2036, 2013.
- [57] P. Lecomte, « Mesure Haute Température en Environnement Irradié par Fibre Optique Utilisant L'Effet Raman », Thèse de Doctorat (PhD), Université de Perpignan via Domitia, Perpignan, France, April 2017.
- [58] J. Stones, "Interaction of hydrogen and deuterium with silica optical fibers: A review" *J. Lightwave Tech.*, no5, pp.712-733, 1987.
- [59] A. Piccolo, I. Planes, S. Delepine-Lesoille, D. Leduc, Y. Lecieux, M. Landolt, S. Girard, Y. Ouerdane "Temperature And Gamma Radiation Coupled Effect In Optical Fibre Distributed Strain Sensors » Journées fibres optiques en milieu radiative, Mons, Belgium, December 2017
- [60] A. Piccolo, S. Delepine-Lesoille, M. Landolt, M. Osmond, S. Poirier, I. Planes, S. Girard, Y. Ouerdane, A. Boukenter, D. Leduc, Y. Lecieux "Combined Radiation and Temperature Effects on Brillouin Scattering based sensing with Ge-Doped Optical Fibers" submitted OFS26, International Optical Fiber Sensor Conference, Lausanne, Suisse, Septembre 2018
- [61] M. Landolt, D. Kinet, A. Piccolo, S. Delepine-Lesoille, P. Mégret « Influence des radiations gamma sur l'herméticité à l'hydrogène des revêtements carbone des fibres optiques » Journées fibres optiques en milieu radiative, Mons, Belgium, December 2017
- [62] G. Failleau, O. Beaumont, R. Razouk, S. Delepine-Lesoille, M. Landolt, B. Courthial, J. M. Hénault, F. Martinot, J. Bertrand, et B. Hay "A metrological comparison of Raman-distributed temperature sensors." *Measurement* 116 (2018): 18-24
- [63] Dubois J.-P. Dubois, S. Delepine-Lesoille, V.-H. Tran, S. Buschaert, S. Mayer, J.-M. Henault, J. Salin, G. Moreau, "Raman versus Brillouin optical fiber distributed temperature sensing: an outdoor comparison (metallic beam and concrete slab) " Conference SHMII-4, 22-24 July 2009, Zurich, Suisse
- [64] S. Delepine-Lesoille, I. Planes, M. Landolt, G. Hermand, et O. Perrochon. "Compared performances of Rayleigh Raman and Brillouin distributed temperature measurements during concrete container fire test." *Optical Fiber Sensors Conference (OFS)*, 2017 25th, pp. 1-4. IEEE, 2017

- [65] S. O’Keefe, A. Fitzpatrick, E. Lewis, A. Al Shamma’a, « A review of optical fibre radiation dosimeters” *Sens. Rev.* 2008, 28, 136-142.
- [66] Beauvois, G.; Caussanel, M.; Lupi, J.-F.; Ude, M.; Trzesien, S.; Dussardier, B.; Duval, H.; Grieu, S. *Projet DROÏD: Développement d’un dosimètre distribué à fibre optique.* In Proceedings of the 7ème Journée sur les Fibres Optiques en Milieu Radiatif (FMR2016), Chatenay Malabry, France, 12-13 December 2016.
- [67] Di Francesca, D., Girard, S., Planes, I., Cebollada, A., Vecchi, G. L., Alessi, A., ... & Lecoecueche, V. (2017). Radiation hardened architecture of a single-ended Raman-based distributed temperature sensor. *IEEE Transactions on Nuclear Science*, 64(1), 54-60.
- [68] Toccafondo, Y.; Marin, E.; Guillermain, E.; Kuhnhen, J.; Mekki, J.; Brugger, M.; di Pasquale, F. Distributed Optical Fiber Radiation Sensing in a Mixed-Field Radiation Environment at CERN. *J. Lightwave Technol.* 2016, doi:10.1109/JLT.2016.2608849.
- [69] Benabdesselam, M.; Mady, F.; Girard, S.; Mebrouk, Y.; Duchez, J.B.; Gaillardin, M.; Paillet, P. Performance of Ge-doped Optical Fibre as a Thermoluminescent Dosimeter. *IEEE Trans. Nucl. Sci.* 2013, 60, 4251-4256
- [70] Di Francesca, D.; Toccafondo, I.; Calderini, S.; Vecchi, G.L.; Girard, S.; Alessi, A.; Ferraro, R.; Danzeca, S.; Kadi, Y.; Brugger, M. Distributed Optical Fiber Radiation Sensing in the Proton Synchrotron Booster at CERN, In Proceedings of the RADECS 2017 Conference, Geneva, Switzerland, 2-6 October 2017
- [71] S. Delepine-Lesoille, S. Girard, S., M. Landolt, J. Bertrand, I. Planes, A. Boukenter, E. Marin, G. Humbert, S. Leparmentier, J.L. Auguste, Y. Ouerdane “France’s State of the Art Distributed Optical Fibre Sensors Qualified for the Monitoring of the French Underground Repository for High Level and Intermediate Level Long Lived Radioactive Wastes”, *Sensors*, 17(6), p.1377, 2017
- [72] Modern2020, WP3.4, Milestone 38 J.L. Auguste & G. Humbert “Report from Xlim – M. Kudinova PhD activity from 01/2016 to 12/2017” May 2018
- [73] X. Bevenot, A. Trouillet, C. Veillas, H. Gagnaire and M. Clement, "Hydrogen leak detection using an optical fiber sensor for aerospace applications", *Sensors and Actuators B*, 67, 57-67 (2000).
- [74] M.A. Butler, "Optical fiber hydrogen sensor", *Applied Physics Letters*, 45 (10), 1007-1009 (1984).
- [75] D. Monzon-Hernandez, D. Luna-Moreno and D. Martinez-Escobar, "Fast response fiber optic hydrogen sensor based on palladium and gold nano-layers", *Sensors and Actuators B*, 136 (2), 562-6 (2009).
- [76] M. Tabib Azar, B. Sutapun, R. Petrick and A. Kazemi, "Highly sensitive hydrogen sensors using palladium coated fiber optics with exposed cores and evanescent field interactions", *Sensors and Actuators B* 56 (1-2), 158-63 (1999).
- [77] J. Villatoro and D. Monzon-Hernandez, "Fast detection of hydrogen with nanofiber tapers coated with ultra-thin Pd layers", *Optics Express*, 13 (13), 5087-5093 (2005).
- [78] L. Goddard, K.Y. Wong, A. Garg, E. Behymer, G. Cole and T. Bond, "Measurements of the complex refractive index of Pd and Pt films in air and upon adsorption of H<sub>2</sub> gas", *IEEE Lasers and Electro-Optics Society (LEOS 2008)*, 569-70 (2008).
- [79] F. Greco, L. Ventrelli, P. Dario, B. Mazzolai and V. Mattoli, "Micro-wrinkled palladium surface for hydrogen sensing and switched detection of lower flammability limit ", *International Journal of Hydrogen Energy*, 37, 17529-17539 (2012).
- [80] S. Delepine-Lesoille, J. Bertrand, L. Lablonde and X. Phéron, "Distributed hydrogen sensing with Brillouin scattering in optical fibers", *Photonics Technology Letters*, 24 (17), 1475-1477 (2012).
- [81] S. Leparmentier, J.-L. Auguste, G. Humbert, G. Delaizir, S. Delepine-Lesoille, "Fabrication of optical fibers with palladium metallic particles embedded into the silica cladding", *Optical Materials Express* Vol. 5, Issue 11, pp. 2578-2586 (2015)



- [82] S. Leparmentier, J.L. Auguste, G. Humbert, G. Pilorget, L. Lablonde, S. Delepine-Lesoille, "Study of the hydrogen influence on the acoustic velocity of single-mode fibers by Rayleigh and Brillouin backscattering measurements", SPIE 9634-118, OFS24, International Optical Fiber Sensors Conference, 28/09 au 02/10/15, Curitiba, Brésil
- [83] M. Kudinova, G. Humbert, J.-L. Auguste, S. Delepine-Lesoille, « Système de mesures d'hydrogène fondé sur des fibres optiques biréfringentes », Patent application, 28/11/2017 no 1761320
- [84] Bristow, K.L., White, R.D. & Kluitenberg, G.J. (1994): Comparison of single and dual probes for measuring soil thermal properties with transient heating, *Aust. J. Soil Res.*, 32, 447-464.
- [85] Brugg cables, (2015): BRUsens Temperature 85 °C heatable, Fibre Optic Sensing Cable, 2012/10/16 Rev. 05 BK © www.bruggcables.com/sensing
- [86] Carslaw, H.S. & Jaeger, J.C. (1959): *Conductivity of heat in solids*. 2nd ed. Clarendon, Press, Oxford, UK.
- [87] Ciocca, F., Lunati, I., van de Giesen, N. & Parlange, M.B. (2012): "Heated Optical Fiber for Distributed Soil-Moisture Measurements: A Lysimeter Experiment", *Vadose Zone J.* - doi:10.2136/vzj2011.0199.
- [88] Decagon Devices, Inc (2015): KD2 Pro Owner's manual, <https://www.decagon.com/en/thermal/instruments/kd2-pro/>
- [89] Delta Elektronika, DC Power Supplies (2015), © Delta Elektronika <http://www.delta-elektronika.nl/>
- [90] Dingfeng, C., Bin, S., Honghu, Z., Guangqing, W., Shen-En, C. & Junfan, Y. (2015): A distributed measurement method for in-situ soil moisture content by using carbon-fiber heated cable, *Journal of Rock Mechanics and Geotechnical Engineering*, 7, 700-707.
- [91] Garitte, B., Weber, H., Müller, H. R., Köhler, S., Kaufhold, S., Plötze, M., Paysan, S., Ohms F. & Holl, M. (2015): Requirements, manufacturing and QC of the buffer components Report LUCOEX – WP2, pp 115.
- [92] Karnland, O. (2010): Chemical and mineralogical characterization of the bentonite buffer for the acceptance control procedure in a KBS-3 repository, SKB Technical Report, TR-10-60, pp. 29.
- [93] Müller, H.R., Garitte, B. Vogt, T., Köhler, S., Sakaki, T., Weber, H., Spillmann, T., Hertrich, M., Becker, J. K., Giroud, N., Cloet, V., Diomidis, N. & Vietor, T. (2017): Implementation of the full-scale emplacement (FE) experiment at the Mont Terri rock laboratory, *Swiss Journal of Geoscience*, DOI 10.1007/s00015-016-0251-2.
- [94] Read, T., Bour, O., Selker, J.S., Bense, V.F., Borgne, T.Le., Hochreutener, R. & Lavenant, N. (2014): Active-Distributed Temperature Sensing to continuously quantify vertical flow in boreholes, *Water Resour. Res.*, 50, 3706–3713, doi:10.1002/2014WR015273.
- [95] Sakaki, T., Köhler, S. & Müller, H.R. (2015a): FE Experiment: Density measurement of granulated bentonite mixture in a 2D pre-test using a dielectric moisture profile probe, P-04-02, Clay Conference 2015, March 23-26, Brussels, Belgium.
- [96] Sakaki, T., Köhler, S., Hertrich, M. & Müller, H.R. (2015b): FE Experiment: Density measurement of granulated bentonite mixture in a 3D 1:1 scale mockup test using dielectric tools, P-04-03, Clay Conference 2015, March 23-26, Brussels, Belgium.
- [97] Sakaki, T., Firat, B. & Vogt, T. (2017a): Feasibility experiments for estimating dry density of granulated bentonite mixtures in narrow annulus using heated fiber-optic cables. Nagra Project Report NPB 17-08.
- [98] Sakaki, T., Firat, B. & Vogt, T. (2017b), Feasibility Experiments for Monitoring State of Granulated Bentonite Mixtures using Heated Fiber-optic Cables. Nagra Arbeitsbericht NAB 17-35.

- [99] Sakaki, T., Firat, B. & Vogt, T. (2018a): Feasibility experiments for estimating dry density of granulated bentonite mixtures in narrow annulus using heated fiber-optic cables, Year 2 progress report. Nagra Project Report NPB 18-08.
- [100] Sakaki, T., Firat Lüthi B., Vogt T., Uyama M. and Niunoya S. (2018b), Heated fiber-optic cables for distributed dry density measurements of granulated bentonite mixtures: Feasibility experiments, *Geomechanics for Energy and the Environment*, <https://doi.org/10.1016/j.gete.2018.09.006>.
- [101] Sayde, C., Gregory, Ch., Gil-Rodriguez, M., Tufillaro, N., Tyler, S., van de Giesen, N., English, M., Cuenca, R. & Selker, J.S. (2010): Feasibility of soil moisture monitoring with heated fiber optics, *Water Resources Research*, Vol. 46, W06201, doi:10.1029/2009WR007846.
- [102] Sayde, C., Buelga, J.B., Rodriguez-Sinobas, L., Khoury, L.E., English, M., van de Giesen, N. & Selker, J.S. (2014): Mapping variability of soil water content and flux across 1 – 1,000 m scales using the Actively Heated Fiber Optic method, *Water Resour. Res.*, 50, 7302–7317, doi:10.1002/2013WR014983.
- [103] Silixa Ultima User Manual (2015): © Copyright Silixa Ltd 2015, [www.silixa.com](http://www.silixa.com).
- [104] Tang, A.M. & Cui, Y.J. (2006): Determining the Thermal Conductivity of Compacted MX80 Clay, ASCE Fourth International Conference on Unsaturated Soils, April 2 –6, Arizona, USA, doi.org/10.1061/40802(189)142.
- [105] Ukil, A., Braendle, H. & Krippner, P. (2011): Distributed Temperature Sensing: Review of Technology and Applications, *IEEE Sensors Journal*, Vol. 12-5, 885–892, doi: 10.1109/JSEN.2011.2162060.
- [106] MoDeRn Project, Proceedings of an International Conference and Workshop, Luxembourg, 19 – 21 March 2013
- [107] MoDeRn Project, Technical requirements report DELIVERABLE (D-N°:2.1.1), 2011.
- [108] Biot, M. A. "Theory of propagation of elastic waves in a fluid-saturated porous solid", 1956
- [109] Frazier CH1, Cadalli N, Munson DC Jr, O'Brien WD Jr Acoustic imaging of objects buried in soil. *J Acoustic Society American* 2000 Jul;108(1):147-56.
- [110] Michael L. Oelze, William D. O'Brien, Jr., and Robert G. Darmod, Measurement of Attenuation and Speed of Sound in Soils, *The Journal of the Acoustical Society of America* 109, 2287 (2001)
- [111] Podio et al. «Ultrasonic velocity and attenuation measurement in water-based drilling mud», 1990. 
- [112] Orban «New ultrasonic caliper for MWD operations», 1991 
- [113] Kai and Taining "Experimental study on ultrasonic propagation in water-based bentonite slurry", 2009. 
- [114] <https://www.pile.com>
- [115] V. Saltas, F. Vallianatos, D. Triantis, "Dielectric properties of non-swelling bentonite: The effect of temperature and water saturation" *Journal of Non-Crystalline Solids* Vol. 354, Issues 52–54, 15 December 2008, Pages 5533–5541
- [116] Hong C. Rhim, Oral Buyukozturk, "Electromagnetic properties of concrete at microwave frequency range" *Acı materials journal*, n° 95-M25, May-June 1998, Pages 263–271
- [117] Ana T. Lima, J. P. Gustav Loch, Pieter J. Kleingeld "Bentonite electrical conductivity: a model based on series-parallel transport" *J Appl Electrochem* 2010, Pages 1061–1068

- [118] Vissuta Jiwariyavej, Takehiro Imura, Takuya Koyanagi, Yusuke Moriwaki, Yoichi Hori, Chiaki Nagai, Kenichi Ando, Kazuya Watanabe, Masao Uyama “Basic Experimental Study on Effect of Bentonite to Efficiency of Wireless Power Transfer Using Magnetic Resonance Coupling Method”
- [119] Timo Saarenketo. Electrical properties of water in clay and silty soils. *Journal of Applied Geophysics*, 40(1-3):73–88, 1998.
- [120] A. Sihvola. *Electromagnetic Mixing Formulae and Applications*. Number 47 in IEE Electromagnetic Waves Series. INSPEC, Inc, 2000.
- [121] Ph. Cosenza and A. Tabbagh. Electromagnetic determination of clay water content: role of the microporosity. *Applied Clay Science*, 26(1-4):21–36, 2004.
- [122] S. R. Evett and G. W. Parkin. *Advances in Soil Water Content Sensing: The Continuing Maturation of Technology and Theory*. *Vadose Zone J*, 4(4):986–991, 2005.
- [123] C. M. Regalado. A geometrical model of bound water permittivity based on weighted averages: the allophane analogue. *Journal of Hydrology*, 316:98–107, January 2006.
- [124] LAN Kai and YAN Taining, Experimental study on ultrasonic propagation in water-based bentonite slurry, *Global Geology*, 12 (3) :1742178 (2009)
- [125] Norman Wagner, Eberhard Trinks, Klaus Kupfer, Determination of the spatial TDR-sensor characteristics in strong dispersive subsoil using 3D-FEM frequency domain simulations in combination with microwave dielectric spectroscopy, *Meas. Sci. Technol.* 18 (2007) 1137–1146
- [126] David Daniels, *Ground-penetrating radar*, 2nd ed., The Institution of Electrical Engineers, 2004
- [127] N. Wagner, Th. Bore, J.-C. Robinet, D. Coelho, F. Taillade, and S. Delepine-Lesoille, Dielectric relaxation behavior of Callovo-Oxfordian clay rock: A hydraulic-mechanical-electromagnetic coupling approach, *JOURNAL OF GEOPHYSICAL RESEARCH: SOLID EARTH*, VOL. 118, 1–16, doi:10.1002/jgrb.50343, 2013.
- [128] Appelo, C.A.J and Postma, D., 1993. *Geochemistry, Groundwater and Pollution*. Rotterdam, A.A. Balkema, 536 p.
- [129] Bradbury, M.H., Baeyens, B., 2002. Pore water chemistry in compacted re-saturated MX-80 bentonite: Physico-chemical characterisation and geochemical modelling. Paul Scherrer Institut Bericht Nr. 02-10, Villigen, 2002, p. 42.
- [130] Bruno, J., Arcos, D., Duro, L. 1999. Processes and features affecting the near field hydrochemistry. Groundwater-bentonite interaction. SKB Technical Report TR-99-29.
- [131] Caneiro, A., Fabry, P., Khireddine, H., Siebert, E. 1991. Performance characteristics of sodium super ionic conductor prepared by the sol-gel route for sodium ion sensors. *Anal. Chem.*, vol. 63, 2550 - 2557.
- [132] Curti, E. 1993. *Modelling Bentonite Pore Waters for the Swiss High-level Radioactive Waste Repository*. Helsinki: Wetingen, Switzerland, NAGRA, 74 p. + app. 11 p. (NTB 93-45).
- [133] Fernández, A.M., Baeyens, B., Bradbury, M., Rivas, P., 2004. Analysis of the pore water chemical composition of a Spanish compacted bentonite used in an engineered barrier. *Physics and Chemistry of the Earth*, 29, 105-118.
- [134] Holmboe, M., Wold, S., Jonsson, M., 2012. Porosity investigation of compacted bentonite using XRD profile modelling. *J. Contam. Hydrol.*, 2012 Feb, 1;128(1-4): 19-32.
- [135] Janata, J. 2009. *Principles of chemical sensors*, 2nd ed. Springer Science+Business Media, New York.

- [136] Matuszewicz, M., Liljeström, V., Pirkkalainen, P., Suurinen, J.P., Root, A., Muurinen, A., Serimaa, R., Olin, M., 2013. Microstructural investigation of calcium montmorillonite. *Clay Minerals* 48, 267-276
- [137] Muurinen, A., Lehtikoinen, J. 1999. Porewater Chemistry in compacted bentonite. Report Posiva 99-20.
- [138] Muurinen, A., Karnland, O., Lehtikoinen, J., 2007. Effect of homogenization on the microstructure and exclusion of chloride in compacted bentonite. *Physics and Chemistry of the Earth, Parts A/B/C*, 32(1-7), 485-490.
- [139] Muurinen, A., Carlsson, T., 2013. Bentonite Pore Structure based on SAXS, Chloride Exclusion and NMR Studies. Posiva Oy, Olkiluoto, Finland. Working Report 2013-53.
- [140] Muurinen, A., Järvinen, J., 2013. Ion-selective electrodes in pore water chemistry measurement of compacted bentonite. Posiva Oy, Olkiluoto, Finland. Working Report 2013-24.
- [141] Ohe, T., Tsukamoto, M. 1997. Geochemical properties of bentonite pore water in highlevel-waste repository condition. *Nuclear Technology*. Vol. 118, pp. 49-57.
- [142] Pusch, R., Muurinen, A., Lehtikoinen, J., Bors, J., Eriksen, T., 1999. Microstructural and chemical parameters of bentonite as determinants of waste isolation efficiency. European Commission. Nuclear Science and Technology. Project Report EUR 18950 EN.
- [143] Tournassat, C. and Appelo, C.A.J., 2011. Modelling approaches for anion-exclusion in compacted Na-bentonite. *Geochimica et Cosmochimica Acta* 75, 3698-3710.
- [144] Tributh, H., Lagaly, G.A. 1986. Aufbereitung und Identifizierung von Boden- und Lagerstättentonen. I. Aufbereitung der Proben im Labor. *GIT-Fachzeitschrift für das Laboratorium* 30, 524 - 529.
- [145] Van Loon, L.R., Glaus, M.A. and Muller, W., 2007. Anion exclusion effects in compacted bentonites: Towards a better understanding of anion diffusion. *Applied Geochemistry* 22, 2536-2552.
- [146] Wersin, P., 2003. Geochemical modelling of bentonite pore water in high-level water repositories. *J. Contam. Hydrol.* 2003 Mar. 61(1-4): 405-22.
- [147] Yao, S., Wang, M. and Madou, M. 2001. A pH electrode based on melt-oxidized iridium oxide. *Journal of The Electrochemical Society* 148 (4), H29-H36.